Coupled Flow and Geomechanical Modeling, and Assessment of Induced Seismicity, at the Castor Underground Gas Storage Project

Final Report

Ruben Juanes
Massachusetts Institute of Technology

David Castiñeira
Massachusetts Institute of Technology

Michael C. Fehler
Massachusetts Institute of Technology

Bradford H. Hager
Massachusetts Institute of Technology

Birendra Jha
Massachusetts Institute of Technology

John H. Shaw
Harvard University

Andreas Plesch
Harvard University

April 24, 2017

Table of Contents

Executive Summary

Objectives of the Study

The Castor Project is an underground gas storage facility that converted an abandoned oilfield located 22 km offshore from Vinarós in the province of Castellón (Spain) to a natural gas storage site. In September 2013, a few days after large-scale gas injection started in Castor, activity in Castor was halted after several hundred minor earthquakes were detected in the area off the eastern coast of Valencia. The overall objective of our project is to perform an integrated structural, seismological and geomechanical study to assess the occurrence of seismicity in September-October 2013 associated with reservoir operations at the Castor underground gas storage project.

The specific objectives of the study are:

1. To review and synthesize the available geological, geophysical, geomechanical, well and reservoir data, together with the recorded seismicity.
2. To employ all the available data to develop a geological structural model of the study area that includes the Amposta fault system and faults within the reservoir. This 3D geologic structural model enables two lines of inquiry: (1) a seismological analysis, and (2) a coupled flow-geomechanical analysis.
3. To re-analyze the seismological data, including the development of a high-resolution seismic velocity model, relocation of the seismic events, assessment of the evolution of the hypocenters of the earthquake sequence in space and in time, and an evaluation of focal mechanisms of selected events.
4. To build a coupled flow-geomechanical computer model of the reservoir and surrounding area, including the Amposta fault system and other reservoir faults. By determining changes in Coulomb stress on the different faults that may have been activated as a result of fluid injection operations, the model provides a quantitative tool for the post mortem analysis of the September-October earthquake sequence, and for the risk assessment of induced seismicity in the area. The model can also be used to explore possible future scenarios and mitigation strategies if reservoir operations were to continue.
5. Finally, to integrate the outputs of the geological, seismological and flow-geomechanical analyses in the 3D structural model, and assess the mechanisms and potential geologic structures linking reservoir operations with recorded seismicity.

Geologic Structural Model

To analyze Castor Field operations in the context of regional faulting and seismicity, we developed a comprehensive geologic structural model. This model provides a detailed representation of the Castor reservoir properties and structure, embedded in a regional description of major faults that are considered possible candidates for the sources of past or future earthquakes. We also developed a corresponding 3D velocity model (Vp, Vs), to facilitate depth conversion of seismic reflection data and help constrain earthquake locations.

As part of our structural analysis, we also assessed geological constraints on the activity of the Amposta fault system. The southern segment of the fault system and its hanging wall

splays offsets geological strata to the seafloor, indicating recent (late Quaternary or Holocene) tectonic activity, which is consistent with regional studies and fault compilations that have described the Amposta as a tectonically active fault, with the southern Amposta fault transferring strain onto the series of hanging-wall splay faults that we document.

Seismicity Analysis

The main goals of the analysis that we performed on the seismic data were:

1. To review the results of work by previous investigators.
2. To estimate the uncertainties in the locations and faulting mechanisms (moment tensors) of the earthquake sequence;
3. To determine to what extent the seismicity can be associated with the faults in the Geologic Structural Model;
4. To evaluate the evolution of the earthquake sequence in space and time; and
5. To determine the relationship between the seismicity and the stress changes in space and time predicted by the geomechanical model.

Our major conclusions from the analysis of the seismic data are:

1. Seismicity initiated near the platform, rapidly expanded into a spatially distributed zone, then contracted to a tighter cluster surrounding the 6 largest events that occurred after injection stopped.
2. Seismic energy release is dominated by these six relatively large events. These large events are located very close - within a few km of each other. The large events likely occurred along a single NW dipping plane that could be coincident with the Amposta fault. Our locations place these events near the Castor platform.
3. Most events can be associated with faults that are represented in the geological model developed for this project.
4. Event relocations and moment-tensor solutions, within uncertainties, agree with those from Spain's Instituto Geográfico Nacional (IGN), but our preferred moment tensor has a plane that dips to the NW, aligned with the distribution of the largest events.
5. There is very little evidence that the largest events occurred along a low-angle eastward dipping fault.

Coupled Flow-Geomechanics Analysis

We developed a simulation model that couples the flow in the reservoir from fluid extraction and injection with the deformation and stress changes in the rock, based on the theory of coupled poromechanics. The computational model consists in an unstructured mesh that adapts to the faults and reservoir horizons identified and geologic structural model. It accounts for the detailed schedule of production and injection of fluids during the entire history of the reservoir—something that enables history matching the reservoir parameters and builds confidence in model predictions.

Our coupled flow and geomechanics analysis leads to a *dynamic* quantitative simulation of the impact of subsurface operations (oil production and gas injection) on the stresses on the fault structures present in the model. The key outcomes from the simulation study are:

1. The Amposta fault is significantly de-stabilized by injection, with maximum change in Coulomb stress (DCFF) of about 0.5 MPa.
2. Faults located on the hanging wall side of Amposta fault are also de-stabilized (maximum DCFF of about 0.04 MPa), even though they are not subject to pressure variations directly – however, fault stresses are altered via poroelastic effects.
3. The most heavily de-stabilized faults, according to the model, are reservoir faults in close proximity to the Amposta fault (max DCFF ~ 0.4 MPa). All of these faults are steeply dipping.
4. Other reservoir faults farther away from the Castor platform are subject to minimal Coulomb stress changes. This is the case, for example, of the EastBounding fault (known in some previous reports as the "Castor fault"), subject according to our coupled flow-geomechanics model to a maximum DCFF of < 0.002 MPa.

We conducted the coupled flow-geomechanics analysis for other injection scenarios. We find that maximum DCFF values decrease for scenarios with reduced injection rate (and therefore, reduced injection volume). We also simulated a more complex scenario that models gas injection at a higher rate, followed by recovery of the injected gas and an additional injection cycle: we find that this would result in larger de-stabilization (roughly, by a factor of two in terms of maximum DCFF) of the Amposta fault and other reservoir faults.

Conclusions

By integrating the results of our geologic, seismologic, and reservoir flow-geomechanical analyses, we are able to assess the possible linkages between regional faults, the 2013 earthquake sequence, and Castor reservoir operations. From our integrated analysis, we conclude that:

1. Earthquake hypocentral locations determined in this study are consistent with activity on the Amposta fault system, its splays, and faults within the reservoir in the vicinity of the injection sites.
2. The hypocenters of the first several events located near the reservoir, followed by a sequence of earthquakes clustered along and to the west of the tectonically active portions of the Amposta fault and its hanging wall splays.
3. Earthquake focal mechanisms for the mainshock are consistent with the orientations of the Amposta fault, its splays, and steeply dipping reservoir faults.
4. Many relocated earthquakes map to regions of the faults that are destabilized due to injection operations. In particular, our coupled flow-geomechanics model suggests that Amposta, some of its splay faults and several of the reservoir faults in close proximity to Amposta, were significantly de-stabilized by gas injection, induced Coulomb stress changes of up to 0.5 MPa. In contrast, the EastBounding fault (also known as the "Castor fault" in some reports) experienced changes in Coulomb stress < 0.002 MPa. For reference, risk of de-stabilization of a fault is believed to occur for Coulomb stress changes in the order of 0.01 MPa – 0.1 MPa, and perhaps lower (this is in the range of typical stress drops during earthquakes)
5. The six largest earthquakes (M 3.8 to 4.3) occurred late in the sequence, after injection ceased. These events are clustered in a region of the Amposta fault system that was significantly destabilized during gas injection.

6. Other earthquakes extend farther west and south along the Amposta fault system to areas that were not significantly affected by reservoir operations.

These observations suggest the following scenario for the event sequence:

1. Gas injection triggered seismicity on reservoir faults and nearby segments of the Amposta fault system.
2. These earthquakes, in turn, triggered seismicity on the Amposta fault system and possibly other reservoir faults through static or dynamic stress changes, well after injection stopped ("aftershock sequence"). This sequence included the largest earthquakes, which occurred on segments of the Amposta fault system destabilized by gas injection.
3. Earthquakes largely occurred on the tectonically active (southern) portion of the Amposta fault and its hanging wall fault splays.

Recommendations

Coupled flow-geomechanics simulations of additional injection scenarios suggest that, while reduced injection rates generally reduce the maximum Coulomb stress change on Amposta and reservoir faults, values remain high and in risk of inducing seismic events. In particular, the maximum Coulomb stress change is higher than that estimated for the post-mortem analysis in the case of full cycle of gas recovery and injection.

This points to an elevated risk of resuming operations in Castor:

1. Occurrence of M ~ 4 events likely have moved portions of the Amposta fault system closer to failure through static stress changes: these events might have increased Coulomb stress without relieving much moment.
2. Given the fault structures and history of de-stabilization, there is a possibility of earthquakes of significantly larger magnitude. It is worth noting that a complete rupture of the Amposta fault system in the study area could produce a M ≥ 6.8 earthquake, based on standard rupture-area-to-magnitude scaling relations.
3. Defining safe operating injection limits (maximum pressures, rates, volumes) is difficult.

In the case that a determination is made to resume operations, we recommend:

1. Deployment of a dedicated seismic network of ocean bottom seismic stations with good proximity and azimuthal coverage.
2. Slow ramp-up of injection in several phases, with dedicated analysis of seismicity, reservoir pressure, and updating of geomechanics model, after each phase.
3. Develop a protocol for actions to be taken if seismicity occurs or increases during injection (e.g., a traffic-light system).

Finally, it is important to point out that this is a *post-mortem* evaluation of the Castor project, which employs new paradigms for integrating geology, geophysics and reservoir geomechanics. As such, it is unreasonable to expect that a study with industry-standard methodologies would have reached these conclusions ahead of the injection. Our study, however, points to the need for *new standards* to quantify the seismicity risks associated to underground operations, especially in areas where active faults are present.

Chapter 1. Introduction

1.1. Objectives of the Study

The overall objective of our project is to perform an integrated structural, seismological and geomechanical study to assess the occurrence of seismicity in September-October 2013 associated with reservoir operations at the Castor underground gas storage project.

The specific objectives of the study are as follows:

1. To review and synthesize the available geological, geophysical, geomechanical, well and reservoir data, together with the recorded seismicity.

2. To employ all the available data to develop a geological structural model of the study area that includes the Amposta fault system and faults within the reservoir. This 3D geologic structural model enables two lines of inquiry: (1) a seismological analysis, and (2) a coupled flow-geomechanical analysis.

3. To re-analyze the seismological data, including the development of a high-resolution seismic velocity model, relocation of the seismic events, assessment of the evolution of the hypocenters of the earthquake sequence in space and in time, and an evaluation of focal mechanisms of selected events.

4. To build a coupled flow-geomechanical computer model of the reservoir and surrounding area, including the Amposta fault system and other reservoir faults. The model defines the prevalent tectonic stresses, and the reservoir operations that could have triggered the seismic events. Such a model is crucial to determine the changes in the stress field—and, in particular, changes in Coulomb stress — on the different faults that may have been activated as a result of fluid injection operations. The model provides a quantitative tool for the post mortem analysis of the September-October earthquake sequence, and for the risk assessment of induced seismicity in the area. The model can also be used to explore possible future scenarios and mitigation strategies if reservoir operations were to continue.

5. Finally, to integrate the outputs of the geological, seismological and flow-geomechanical analyses in the 3D structural model, and assess the mechanisms and potential geologic structures linking reservoir operations with recorded seismicity.

1.2. Induced Seismicity and Study Approach

In recent years, induced seismicity has emerged as a fundamental aspect surrounding subsurface technologies, both from an operational standpoint and from the point of view of public perception (National Research Council, 2013; Galchen, 2015). Much of the documented evidence of triggered and induced seismicity is related to the subsurface disposal of wastewater produced during as a result of unconventional oil and gas

extraction, predominantly shale oil, shale gas, and mature oil fields that once were deemed uneconomical (Frohlich, 2012; Ellsworth, 2013; Keranen et al., 2013, 2014; van der Elst et al., 2013; Weingarten et al., 2015). However, the anthropogenic origin of triggered earthquakes has been linked to a wide range of subsurface technologies, including geothermal energy (Majer et al., 2007; Deichmann and Giardini, 2009, Brodsky and Lajoie, 2013), oil and gas production (Segall, 1989; Suckale, 2009; Zhang et al., 2009; Valoroso et al., 2009; Improta et al., 2015, Buttinelli et al., 2016), gas injection (Gan and Frohlich, 2013), gas storage (Dost and Haak, 2007; Cesca et al., 2014), and groundwater extraction from shallow aquifers (Gonzalez et al., 2012; Amos et al., 2014)—for a comprehensive recent review, see Foulger et al. (2017).

While the potential for subsurface fluid injection and extraction to trigger earthquakes has long been recognized (Raleigh et al., 1976; Segall, 1989), the sharp increase in the extent and vigor of induced seismicity calls for deeper understanding than is currently available (Guglielmi et al., 2015, Hornbach et al., 2015). This is particularly relevant from the point of view of establishing workflows for reservoir management and decision-making, which incorporate reservoir geomechanical processes, including subsidence, caprock integrity, reservoir compartmentalization, hydraulic fracturing and fault activation and associated seismicity.

It is likely that induced earthquakes may be better understood, modeled and forecast (and—eventually—perhaps managed) than natural earthquakes. The reason is twofold. First, usually there is a relatively dense set of subsurface measurements that provide detailed knowledge of the geologic structure before exploitation, and there is an opportunity to deploy a monitoring program that quantifies changes within that structure, including bottom hole pressures, water cuts and gas-oil ratios, surface deformation, and microseismicity. Second, the injection and extraction of fluids are causally linked to changes in fluid pressures and in the tensor stress state of the subsurface. This linkage can be quantified by mathematical models that describe the coupling between flow through rocks and deformation of those rocks in the presence of fractures and faults.

We propose that geologically realistic computational models of coupled reservoir flow and geomechanics permit the integration of seismic, well log, fluid pressure and flow rate and other data that may be available (e.g., geodetic data) in a way that enables quantitative assessments of the likelihood of induced seismicity, strategies that prevent it, or remediation programs that mitigate it. Naturally, this would have important social, economic, and regulatory consequences.

Previous work from our group has already illustrated the potential of predictive computational models of induced seismicity potential. These include a detailed case study exploring potential connections between the May 2012 Emilia-Romagna sequence in northern Italy and operations in the nearby Cavone oil field. Our analysis addressed the question of whether this earthquake sequence might have been triggered by fluid extraction and injection and, if it is not, whether it is plausible that future reservoir operations could trigger other seismic events (Juanes et al., 2016).

1.3. Background on the Amposta Field and the Castor Project

The Castor Project is an underground gas storage field that converted an abandoned oilfield located 22 km offshore from Vinarós in the province of Castellón (Spain) to a natural gas storage site (Figure 1.1). The main objective of the project was to store gas transferred from mainland Spain via a pipeline approximately 30 km long, mostly running along the sea bottom. The gas storage project was designed for a series of fill-in and production cycles (aiming to better balance the variability in natural gas supply and demand). The Castor gas storage facility was meant to cover 30 percent of Spain's daily gas consumption. The Castor Project, and the related exploitation concession, were owned and developed by Escal UGS S.L.

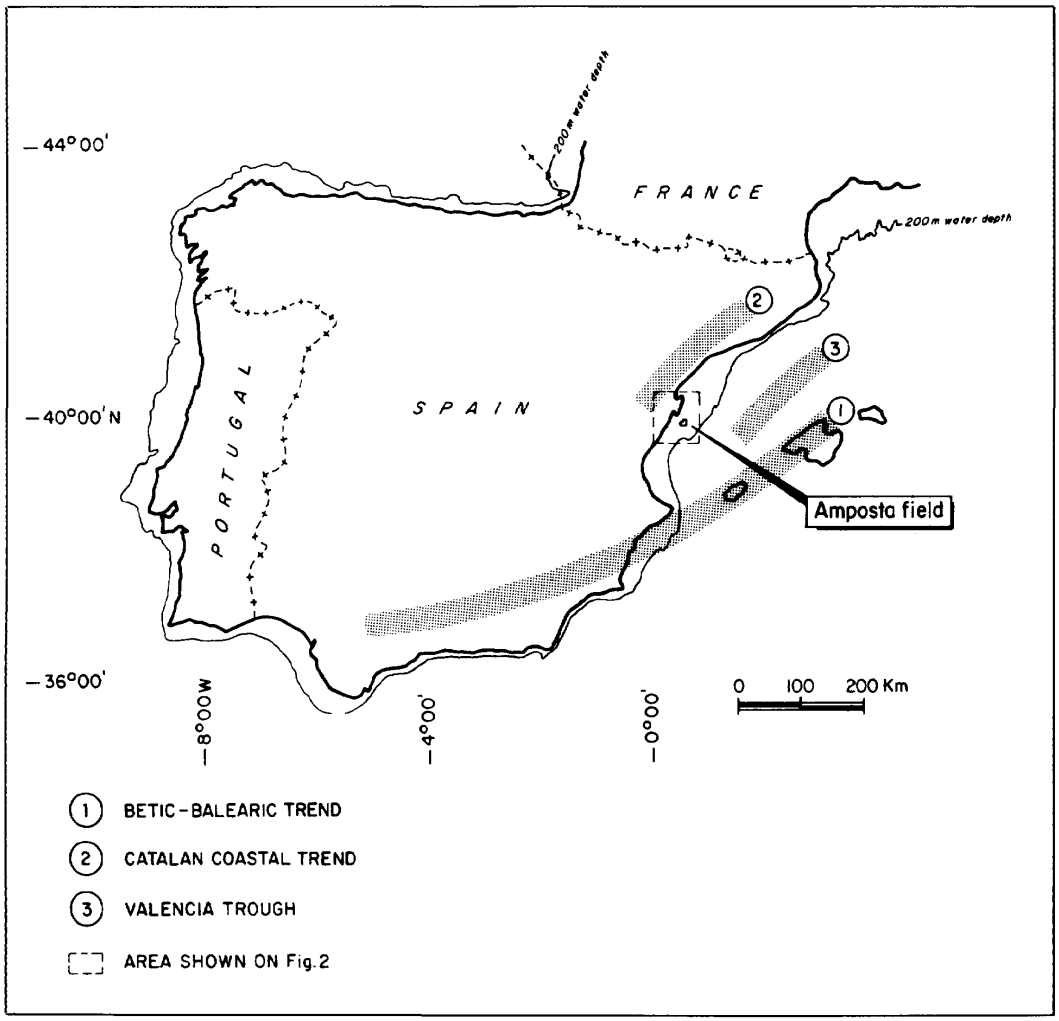

Figure 1.1: Location of the Amposta oil field—the geologic trap used for the Castor gas storage project. From Seemann et al. (1990).

In September 2013, a few days after large-scale gas injection started in Castor, the Spanish government halted activity in Castor after more than 200 minor earthquakes were detected in the area off the eastern coast of Valencia. A series of studies were quickly conducted

(IGN, 2013; IGME, 2013; IGME, 2014) to analyze this seismic activity and to identify the potential relationship to the Castor operations.

From a perspective of subsurface operations, we distinguish three time periods:

i. *Amposta Production Period* (1970-1989):
ii. *Castor Project Design Period* (1996-2012):
iii. *Castor Injection Period* (2012-2013):

As discussed in Section 1.1 of this report, the main goal of the current study is to employ state-of-the-art modeling techniques (using coupled flow and geomechanics simulation) in order to mechanistically and quantitatively evaluate the potential impact of gas injection on fault slip potential and the risk of induced seismicity in the region around the Castor platform. Naturally, this study is focused primarily on the third period described above (Castor Injection Period). However, it was necessary for our analysis to create a new simulation model (i.e., a far more extensive model and with a more comprehensive and complex fault description) in order to properly evaluate the impact of the Castor operations on the main faults in the region. Consequently, our model also intended to capture the historical behavior of the old Amposta field that was reported during the 1970-1989. Hence, from that perspective, this study also covers the first period described earlier (Amposta Production Period).

These three time periods are briefly described below, with an emphasis on key technical aspects that are relevant for our study.

i. Amposta Production Period (1970-1989)

The original Amposta reservoir was discovered by Shell Spain in 1970, and large-scale production from this field started in 1973. This reservoir is described as a N-S oriented horst that is tilted down to the east. From a geological perspective this system is a lower Cretaceous dolomitic limestone that is fractured and brecciated. Here karstification of the limestones has potentially created large cavities in the reservoir (which helps explaining its observed high productivity). As for most naturally fractured reservoirs, a distinction could be made between a matrix system (characterized by low porosity ranging from 0.2-2 % and permeabilities in the order of 0.01 milliDarcy (mD)) and a fracture/karst system (with very large porosities, and permeabilities in the Darcy level).

The Amposta reservoir is sealed on the west by the Amposta fault (a large, deep, normal fault located beneath the Castor platform). On the South, East and North sides the reservoir is sealed by an aquifer. Bottom sealing is also given by the aquifer. On the other hand vertical sealing is given by stratigraphic closure (i.e., the Montsia is overlain by some 60 meters of impermeable formation).

The initial pressure in this reservoir was around 2743 psi. The volume of original oil in place (OOIP) was estimated at 100 MMbbl, although this volume was later updated to be more in the order of ~140 MMbbl by analyzing the reprocessed 3D seismic data that a Shell unit acquired in 1982.

The Amposta reservoir (Montsia formation) was produced until it reached its economical limit in 1989. More than 12 wells were drilled during this production period, and maximum oil production rate in the field was around 40,000 bbl/d in 1975 with just 3 wells. In fact, wells drilled in karstified zones showed very high productivity (those karstified limestone intervals are mostly located in the upper part of the Montsia formation). Along the entire reservoir production history most of the field production was materialized in 6 of the Amposta wells, leading to a total cumulative oil production of approximately 56 MMstb by 1989 (with less than 1% cumulative water cut). The strong aquifer limited the pressure depletion from the reservoir; the maximum pressure decline reported in the field was 70 psi in 1976, and final pressure at field abandonment was reported to be close to original virgin pressure.

ii. Castor Project Design Period **(1996-2012)**

In 1996 Escal UGS became interested in the abandoned Amposta reservoir and the possibility of using this reservoir for a natural gas storage project. A large number of feasibility and design studies were conducted during this period of time, including a new 3D seismic survey, analysis of data obtained from a new drilled well in 2004 (Castor-1), a Petrel static model, a 2D geomechanical model, and a series of dynamic simulation models (using Eclipse and material balance models). The main goal of these studies was to better characterize the Amposta field and to predict the behavior of the Castor system during the gas storage operations.

Starting in 2010 a total of 13 new wells (the so-called Castor wells) were drilled in this field (along with pipeline and platform construction). This recount includes the re-completion of Castor-1 well, a series of observations wells that would monitor the Castor operation, and a water disposal well. All the new wells production/injection wells were completed in the reservoir crest. Initial plans called for those wells to be permanently exposed to gas after the first gas filling. Initial design plans proposed a maximum delivery of 25 MM m3/d (3.5 MM m3/d per well plus one as a spare well); under the same plan eight wells would provide 8 MM m3/d injection capacity.

The design and location of the observation wells was strategic. Well Castor-POB was designed to record pressure and contact movement (using pressure gradient surveys) using 16 downhole gauges completion. Castor OBS and OBN wells were designed to record pressure and identify possible gas leaks by the spill point (completions with 10 downhole gauges). Finally, CSM well was drilled to measure the pressure in the Castellon sealing formation, targeting the bottom sand series M5/M4. A water disposal well was also designed (SWD well) for the Castor operations.

A graphical visualization for the locations of these wells superimposed in one of the Escal-UGS models is provided in Figure 1.2.

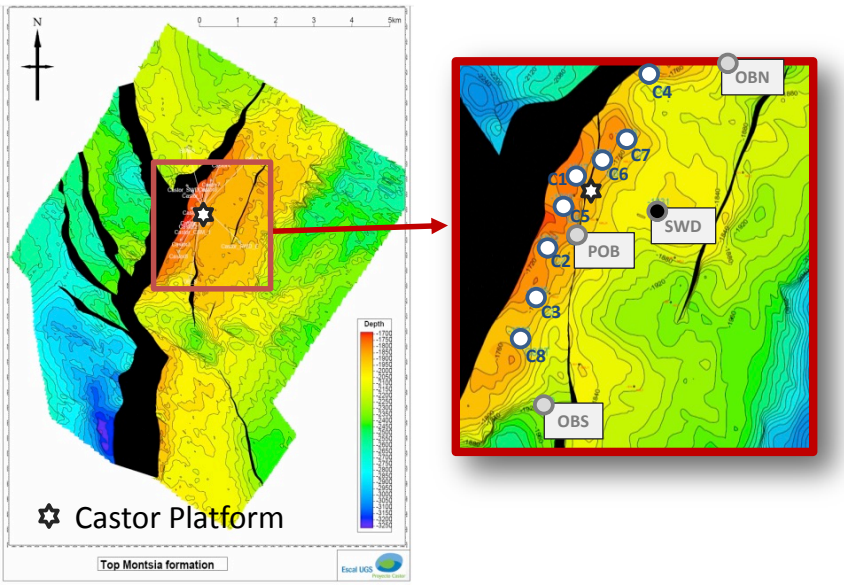

Figure 1.2: New wells drilled for the Castor project. Source of background model: Escal-UGS.

Potential geological risks associated to the Castor project were already identified and analyzed during this period. These risks included:

1) Possible gas leaks through old (or new) wells: Information was especially scarce and incomplete about the mechanical conditions (e.g., seals and cementing) of the abandoned wells in Amposta. Hence it was proposed that potential gas leakage through the wells had to be carefully monitored in Castor.

2) Sealing capacity of Castellon formation: Upward leakage of gas through the seal was considered unlikely due to presence impermeable sands. On the other hand the risk of fracturing the cap rock was analyzed using minifrac, log and core data analysis (and from here a minimum fracturing pressure of 1400 psi above current reservoir pressure was established).

3) Possible reactivation of the faults: A dedicated geomechanical study was conducted (Nauroy et al., 2011) to analyze key aspects such as entry pressure for fluid displacement (methane/brine entry pressure to be applied before displacing any fluid into the formation), caprock strength (which showed a high strength), fracturing pressure (estimated up 1400 psi above initial pressure, in line with minifract tests). Furthermore simulations from a 2D geomechanical mode conclude that the pore pressure in the reservoir could be increased by 710 psi (to a total of ~3400 psi) without reactivating any fault. From here a conservative maximum design operating pressure of 3225 psia at the topmost gauge was recommended.

Several simulation models were built during this period of time (and before the onset of operations in Castor) in order to predict and characterize the dynamic response of the abandoned Amposta reservoir to new gas injection and production. Both material balance model (using MBAL software) and full-physics simulation studies (using Eclipse 300

software) were conducted. These simulations studies concluded that the pressure response in Castor would stay within operation limits under the proposed injection and production programs. In reality this predicted pressure response actually overestimated the observed pressure response during the injection period. This was later attributed, among other aspects, to the relatively unknown behavior of the formation top to the new conditions (so filling curve in this area was mainly theoretical), a model that was calibrated with (only) production history (which was characterized by imbibition of rock-saturated oil by water aquifer, in contrast to a new displacement mechanism involving gas drainage). Moreover it was proposed that a dual porosity model would have been perhaps necessary in order to better match the gas-liquid response observed during the Castor phase.

iii. Castor Injection Period (2012-2013)

A series of injection tests were conducted using some of the new Castor wells (Castor-1, Castor-2, Castor-4, …) from 2012 to August 2013. These tests were intended mainly to evaluate Castor infrastructure, well injectivity, and key operational parameters. Large-scale gas injection began in Castor on September 2, 2013. Figure 1.3 shows the reported (individual well) gas injection rates and cumulative gas injection during the Castor operation.

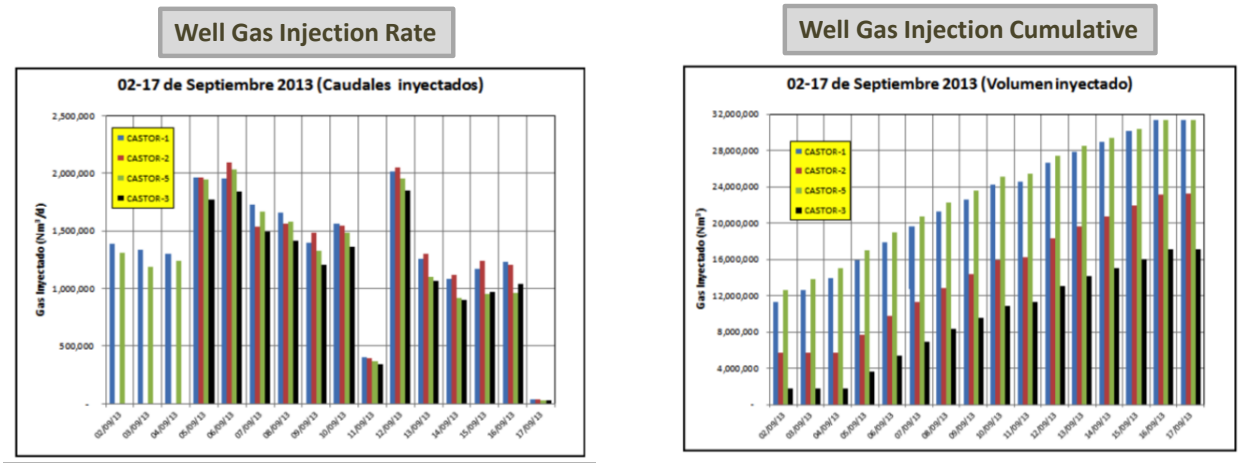

Figure 1.3: Individual well gas injection rates (left panel) and gas injection cumulatives (right panel) during the Castor field operation. Source: Escal-UGS (Proyecto Castor, Informe de Campaña de Inyección 2013, GKI / IT-TE-035).

Starting on September 5, 2013 a series of earthquakes was detected in the proximity of the Castor project, and some of these seismic events were felt in the nearby coastal towns of Vinarós and Benicarló (IGME, 2014). Gas injection was officially terminated on September 17, 2013. The largest earthquake (Mw=4.3) was detected in the area on October 1, 2013. The last earthquakes felt by the population during this sequence were registered around October 4, 2013. Seismic activity in the area largely decayed after mid-October 2013. During the injection period the maximum pressure increase observed in the Castor field was 111 psi above the initial formation pressure, which was well below the maximum pressure threshold for safe operation estimated during the previous feasibility studies.

Following the occurrence of the earthquake sequence, several post-mortem studies were conducted (IGN, 2013; IGME, 2013, 2014; Cesca et al., 2014; Gaite et al., 2016; Saló et al., 2017). Our current study builds on these studies, but follows a markedly different approach, which hinges on the integration of structural geology, seismology, and coupled flow-geomechanics for the interpretation of the recorded seismicity following gas injection. Our results also provide a mechanistic basis for exploring additional injection scenarios that shed light on the risks of resuming gas injection/extraction operations.

Chapter 2. Geologic Structural Model

To analyze Castor Field operations in the context of regional faulting and seismicity, we developed a comprehensive geologic structural model. This model provides a detailed representation of the Castor reservoir properties and structure, embedded in a regional description of major faults that are considered possible candidates for the sources of past or future earthquakes. We also developed a corresponding 3D velocity model (Vp, Vs), to facilitate depth conversion of seismic reflection data and help constrain earthquake locations.

2.1. Geologic Setting of the Castor Field

The Castor Gas Storage Project is located in Valencia Trough of the western Mediterranean Sea (Figure 2.1). This region separates the Iberian Peninsula from the Balearic Islands, and is characterized by a series of northeast-southwest trending extensional grabens that are bounded by normal faults. These grabens formed in the Late Oligocene to Neogene during ongoing convergence of the European and African tectonic plates (Roca and Guimerà, 1992; Bartrina et al., 1992). The bounding fault systems offset the Mesozoic pre-tectonic section, including the Cretaceous platform carbonates that form the primary hydrocarbon reservoirs in the region. The grabens are filled with syntectonic Alcanar Group sediments, which in turn are overlain by Castellon and Ebro Group siliciclastic sections (Bartrina et al., 1992; Gessal, 2013). Several of the bounding normal faults show evidence of ongoing late Tertiary tectonic activity (García-Mayordomo et al., 2012; Perea et al., 2012).

The Castor field is a horst block located to the east of the Amposta graben. The horst block and graben are formed by the Amposta fault, which dips to the west and produces up to ≈ 1km of normal offset on the upper Cretaceous Montsia reservoir units (Figure 2.2). The reservoir units dip gently to the east, forming a fault bounded trap. The culmination of the trap defines the Amposta oil field and the Castor gas storage site, and coincides with a region where the trend of the Amposta fault changes from northwest to northeast. This bend in the fault localizes a series of splay faults that cut the graben and extend to the northwest. In addition, the horst block and reservoir are cut by several southeast and northwest dipping faults that exhibit 10's to 100's of meters of normal separation on the Montsia reservoir and overlying Tertiary units.

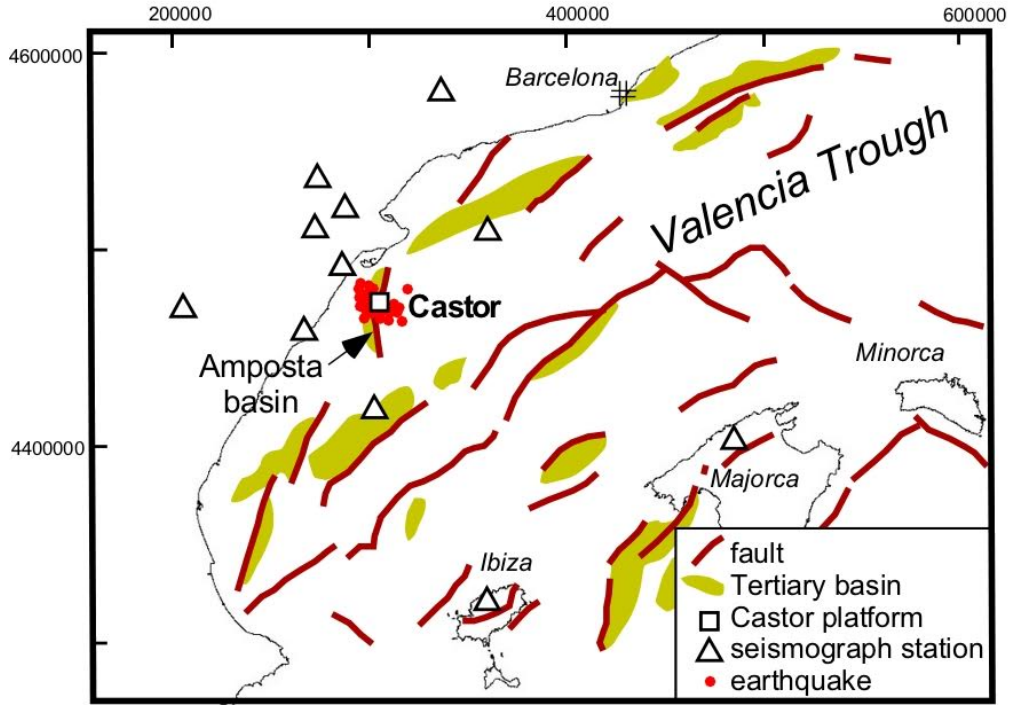

Figure 2.1: Map of Valencia Trough showing location of major offshore faults and Tertiary basins (from Alaya et al., 2015). Seismicity after the initiation of injection operations is shown within a 10km radius of the Castor platform (IGN, 2013).

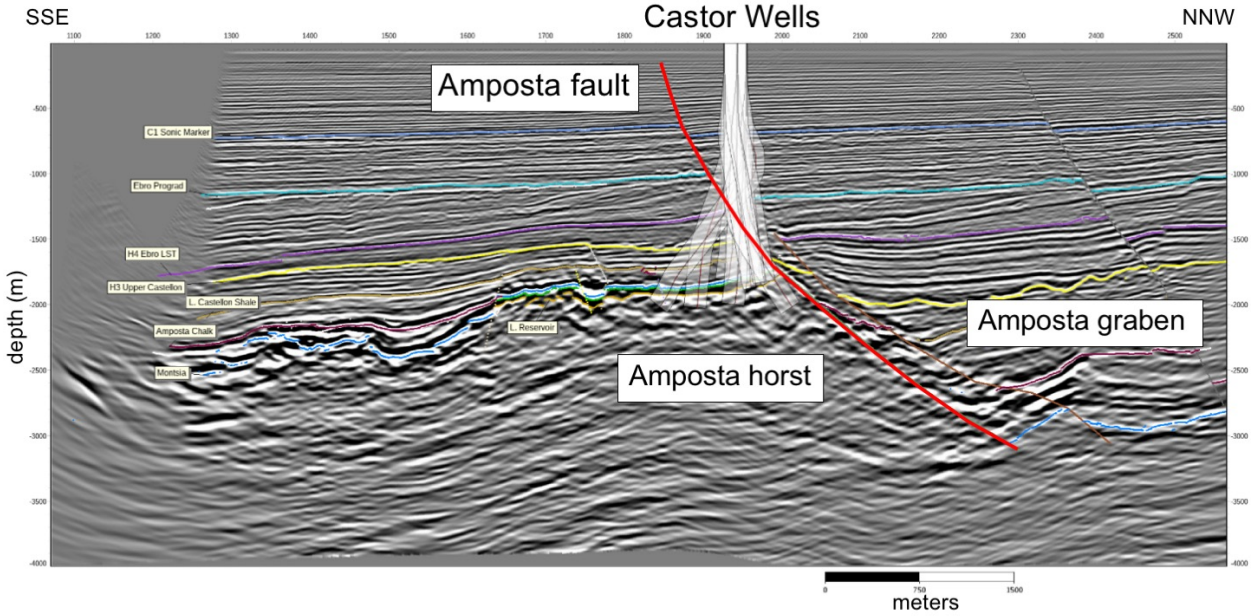

Figure 2.2: Seismic reflection profile from the 3D survey showing Amposta fault and horst block that provides the structural trap for the Castor field.

2.2. Model Construction

We developed our 3D structural model using Gocad (Mallet, 1992; Paradigm Geophysical), and industry-standard structural modeling application that facilitated integration of geologic, geophysical, and seismological data. These data were provided by Enagas, and include a 3D seismic reflection survey, 41 regional 2D seismic reflection profiles, formation tops and logs from 29 wells (Figure 2.3). The 3D seismic survey was acquired in 2005, and processed using standard wave-equation migration techniques and converted to depth using velocity data calibrated with well logs. This survey, in conjunction with well data from the field, served as the basis for defining the reservoir model. Enagas provided detailed fault and horizon interpretations from the 3D depth seismic volume. These interpretations were reviewed and found to be of high quality. We made modifications to these fault and horizon interpretations where appropriate, and extended the mapping of the reservoir and regional fault systems using both 3-D and 2-D seismic reflection data. In order to incorporate interpretations of the 2-D seismic data, which were provided in two-way travel time (TWTT), we constructed an initial velocity model based on sonic logs from the field. This model was used to depth convert the 2-D data. Stratigraphic markers in these depth-converted 2-D data closely matched corresponding units in the 3-D survey, confirming the validity of the velocity model.

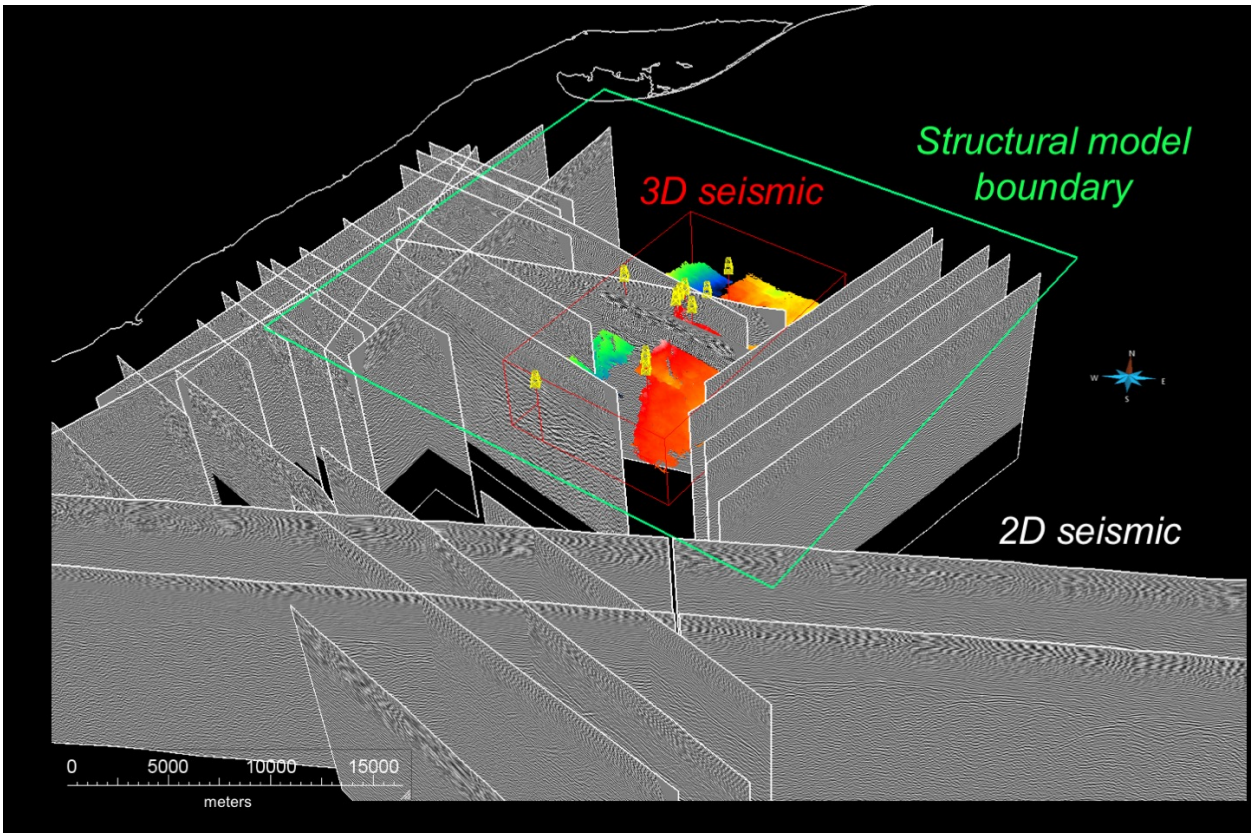

Figure 2.3: Perspective view of datasets used to construct our 3-D structural model. Castor and Amposta wells are shown. The colored surface represents the top Montsia reservoir.

The next step in our analysis was to develop triangulated surface (tsurf) representations from the fault interpretations. These surfaces were generated using discrete smooth interpolation (DSI) in Gocad, in a manner that ensured consistency between the seismic interpretations and the faults identified in wells. This process is illustrated for the Amposta fault in Figure 2.4. In order to constrain the fault geometry below the effective imaging depth of the seismic reflection data, we used an inclined shear method to model the fault based on the geometry of folds present in its hanging wall. These fold, known as rollovers, form in response to displacement on curved or listric normal faults (Hamblin, 1965). These structures are common in the Valencia Trough as well as in other extensional basins around the world. Inclined shear modeling techniques are well established as the most effective method to define fault geometry in these systems (Gibbs, 1983; Groshong, 1990; Xiao and Suppe, 1992; Shaw et al., 1997). Application of these methods to the Amposta fault demonstrate that it shallows from a 57°W dip in the vicinity of the field to a more gentle (≈5W) west dip at a depth of about 7km. We used these constraints, along with the fault interpretations from the 3-D and 2-D seismic surveys to generate a surface that represents the Amposta fault throughout the study area (Figure 2.4b). We then developed representations of the splays in the hanging wall of the Amposta fault. These structures do not exhibit well developed rollovers in their hanging walls, and appear to be planar. Thus, we extrapolated these faults from the seismic interpretations to depth and terminated them into the Amposta fault surface.

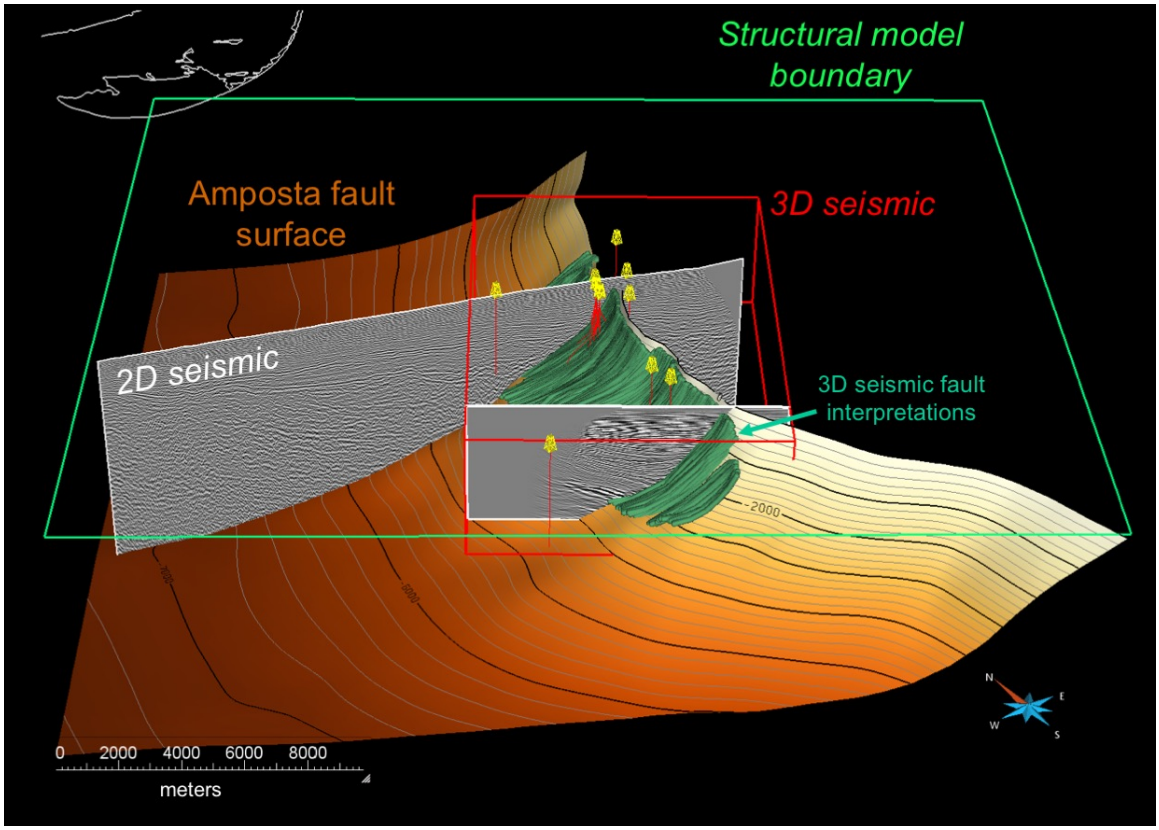

Figure 2.4: Perspective view of select data constraints used to construct the Amposta fault surface. The complete Amposta fault representation is shown with depth contours in meters subsea.

We followed similar procedure to develop surfaces that represent the major reservoir faults (Figure 2.5). These structures include a set of steeply dipping normal faults in the immediate vicinity of the Castor injection wells (F10, 11, & 12), and extensions of these fault systems along strike (e.g., F14, South fault). We also generated representations of select reservoir faults at greater distances from the injection wells. We chose to represent the largest and most laterally continuous of these faults, and included the east dipping Castor fault, which had been previously interpreted as a potential source of the 2013 seismicity. Notably, all of the reservoir faults that we interpret and represent in the model are steeply (> 45°) east- or west-dipping structures and exhibit normal separation. Previous studies have represented some of these faults in TWTT displays, which show them as more gently dipping structures (e.g., Seemann et al., 1990; Cesca et al., 2014). However, direct constraints (cut-offs, fault-plane reflections) from the 3D seismic survey displayed in depth confirm that these are more steeply (> 45°) dipping faults. This will have significance when we investigate focal mechanisms for the largest events in the 2013 earthquake sequence and attempt to relate them to fault geometries represented in the model.

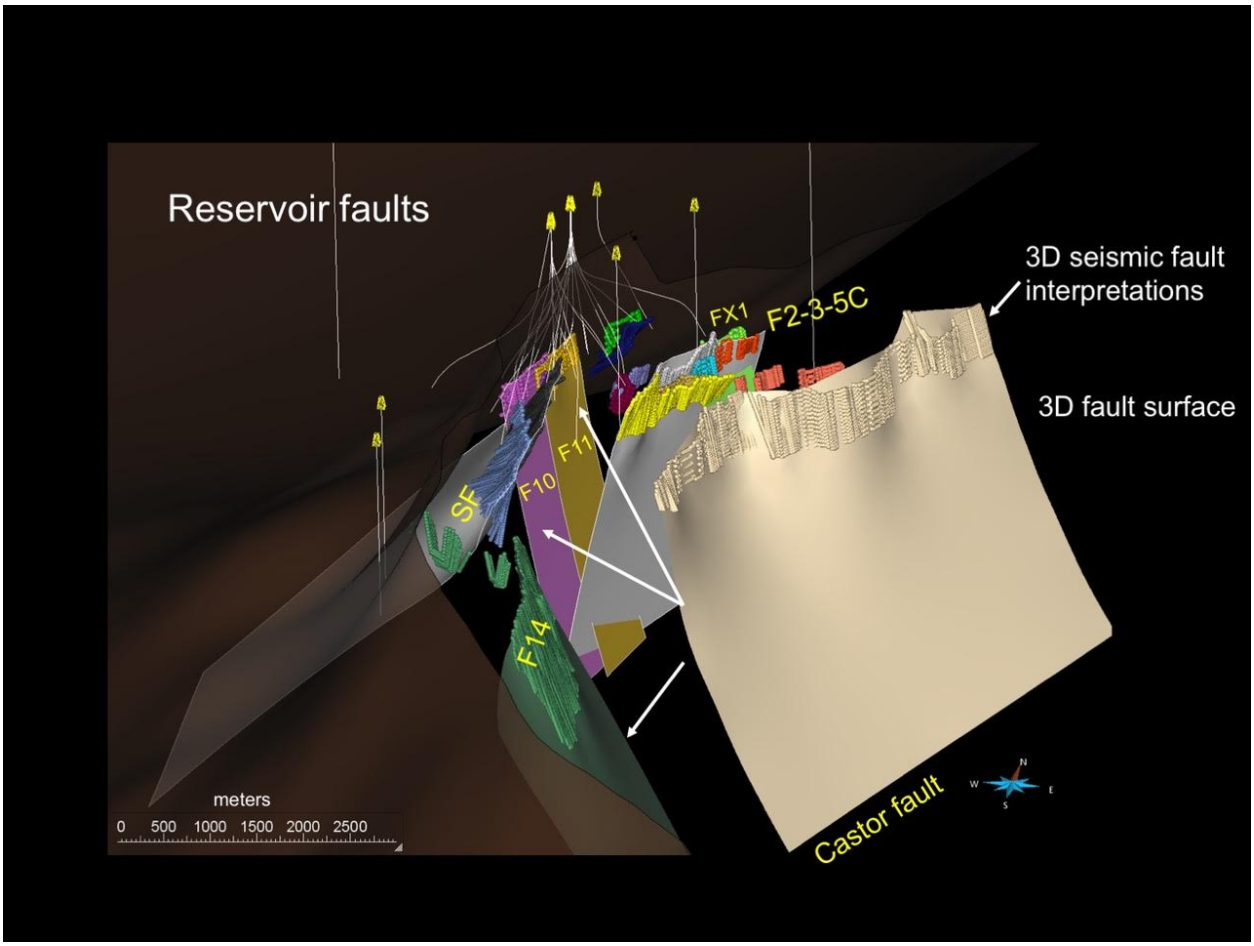

Figure 2.5: Perspective view of reservoir faults mapped in the 3D seismic reflection data and extrapolated to develop fault surfaces. Labeled faults are those incorporated in the model used for the coupled flow-geomechanical analysis.

The final set of faults included in our model are located west of the Castor Field and Amposta fault surface. These faults (Splay 1A/B, Splay 1B anti1/2, Splay 2A/B/C, Splay 2B anti1, Splay 3, Splay 4/5) trends approximately north-south and dip to the east, and are considered tectonically active based of displacements of young, near surface sediments (e.g., García-Mayordomo et al., 2012; Perea et al., 2012). We constrained the strike and dip of these faults using published maps and 2-D seismic data. Surfaces were generated by extrapolated the fault traces to depth. We included these faults in the model, as they represent potential earthquake sources. Thus, we calculate stress changes acting on these faults related to Castor Field operations, and consider these faults in our analysis of the 2013 earthquake sequence.

In addition to representing faults, our model included several geologic horizons that define the Castor reservoir and seal (caprock), as well as influence seismic wavespeeds. These surfaces include base Paleozoic, base Jurassic, and base Tertiary. The base Tertiary horizon corresponds to the top Montsia reservoir unit, and is generally well imaged in both the 3-D and 2-D seismic datasets. We evaluated a set of horizon picks provided by Enagas in the vicinity of the Castor wells, and deemed them to be of high quality. We revised these interpretations as needed to ensure consistency with the faults, and then extended the mapping of these surfaces through the study region using well tops and the seismic reflection datasets (Figure 2.6). The top reservoir surface is offset by the Amposta fault system. We mapped this offset, which exhibit up to 1000 meters of normal (down to the west) fault separation on the top reservoir horizon. This fault displacement is represented in our model as discrete hanging wall and footwall cutoffs. Based on anticipated challenges with generating the computational mesh, the choice was made to not explicitly represent offsets for the smaller displacement faults in the model. Rather, offsets on these smaller faults that could be resolved in the seismic reflection data were included as changes in elevation of the surfaces as they cross the faults. We do not feel that this choice of representation had any meaningful effect on our subsequent analysis.

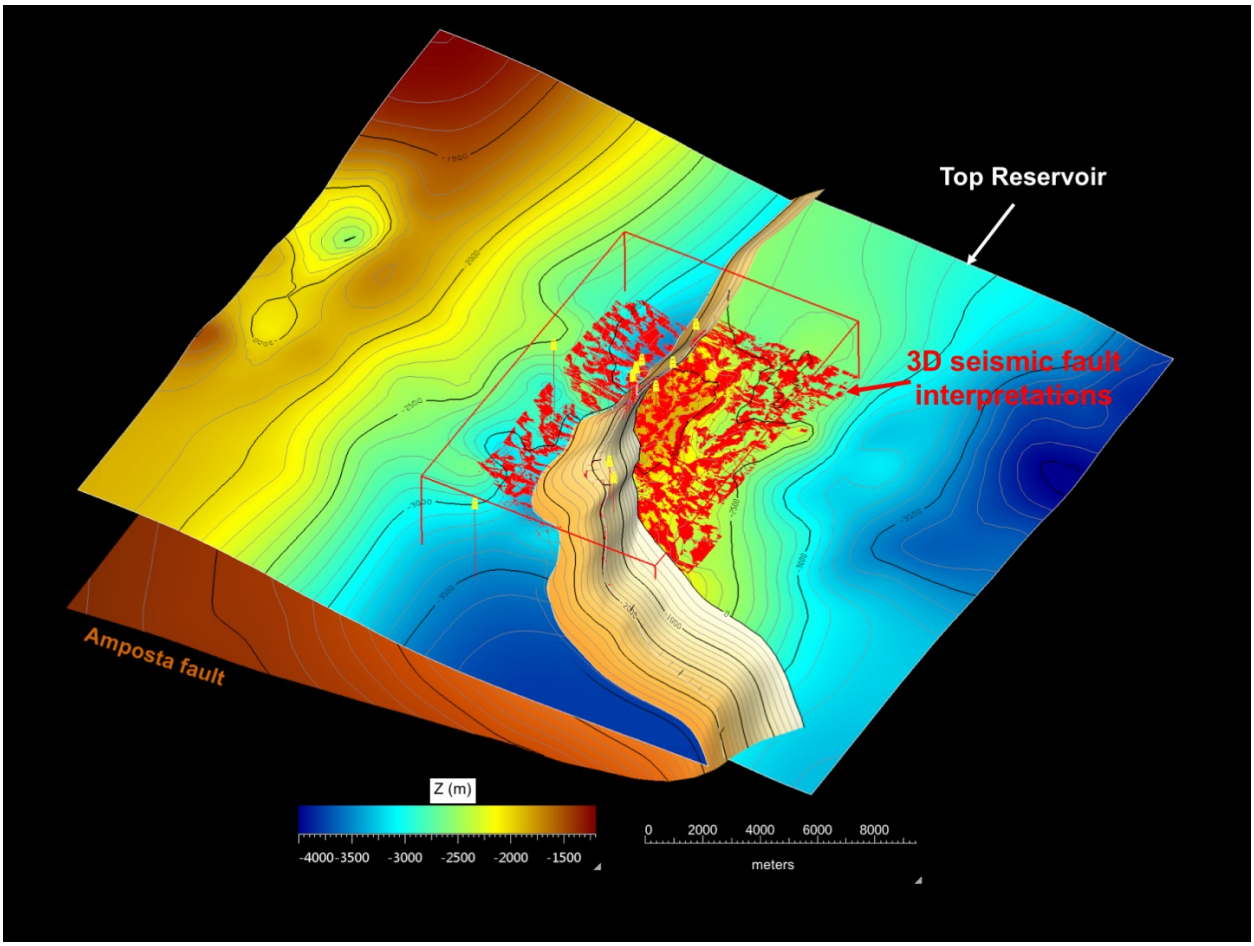

Figure 2.6: Perspective view of the top Montsia Formation reservoir horizon.

In summary, our 3-D structural model includes three major categories of faults: The Amposta fault and its hanging wall splays; reservoir faults (in the footwall of the Amposta fault); and two large regional faults that lie west of the Castor field. In addition, the model includes the top Montsia Reservoir and other stratigraphic horizons, which will be used to define seismic velocities for the seismological analyses and parameterize the reservoir properties for the geomechanical simulations.

2.3. 3D Velocity Modeling

To help support the seismological analysis of the 2013 earthquake sequence, we also developed a 3D velocity (Vp, Vs) model that incorporated components of our regional structural analysis. The primary datasets that constrained wavespeed in our model were sonic logs in the Amposta and Castor wells, along with results of previous studies that constrain velocities for older geologic units in the region (Torne et al., 1992, Vidal et al. 1998). These data, along with the structural components of our model (faults, horizons) were used to develop co-registered Vp and Vs parametrizations, which in turn were embedded in regional tomographic velocity models (e.g., Bassin et al., 2000; Cesca et al., 2014; Gaite et al., 2016). The resulting velocity representation covered a larger area than the structural model, as it was necessary to encompass several of the stations used in our seismological analysis (Figure 2.7).

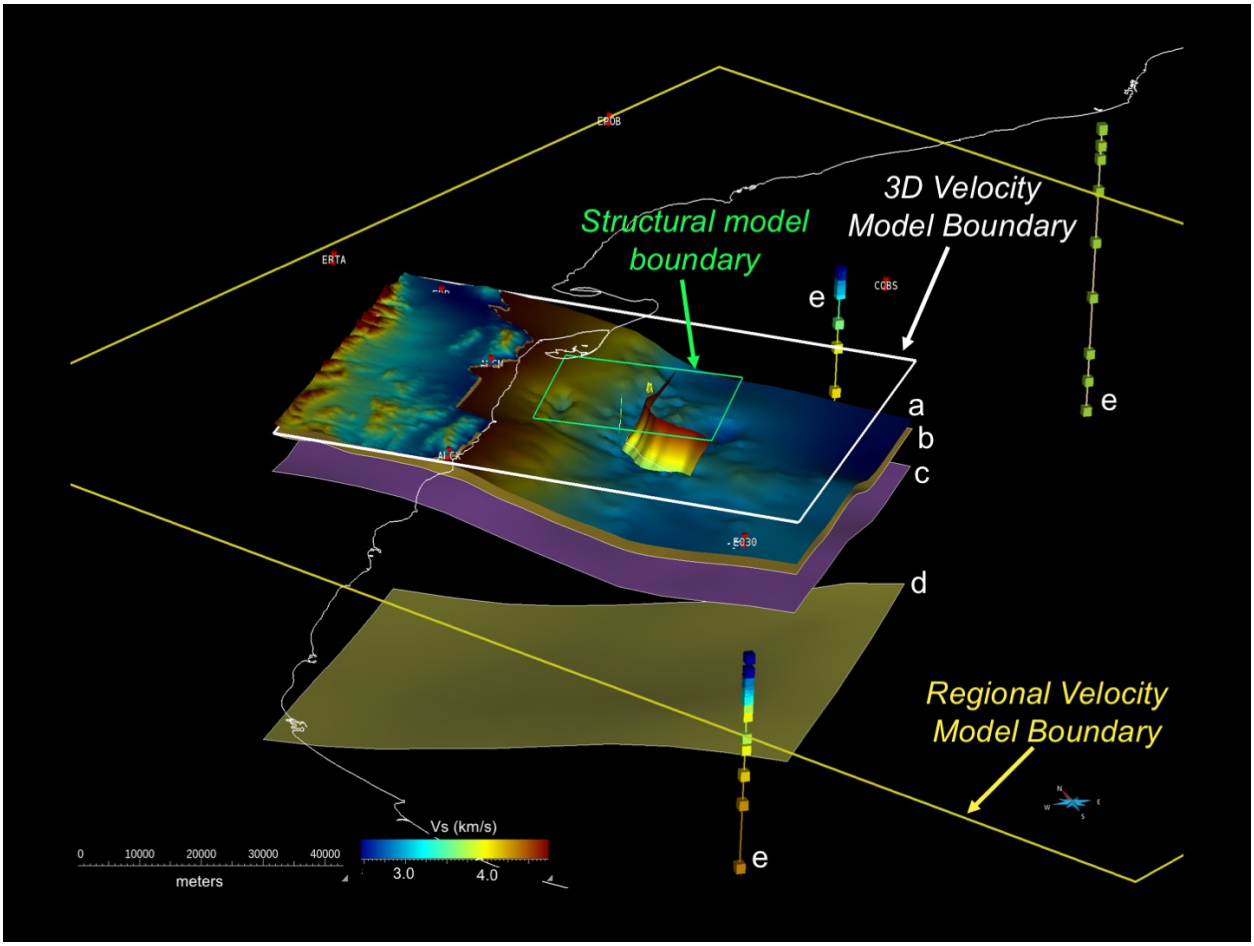

Figure 2.7: Perspective view of the geologic surfaces used to constrain our 3-D velocity model. a – base Tertiary (top Montsia reservoir); b – base Jurassic; c – base Paleozoic; d- Moho; e – velocity profiles from regional models.

The seismic wavespeed structure in the Castor region is defined by four principal lithologic units: Tertiary, dominantly siliciclastic section (Alcanar, Castellon, and Ebro Group); Cretaceous to Jurassic carbonates (including the Montsia reservoir); Triassic to Paleozoic siliciclastics, which may include some carbonates in the lower part of the section; and basement. Thus, we developed horizons to define the depth and shape of these lithologic transitions. These included a topography/bathymetry surface (Ryan et al., 2009), a base Tertiary surface, a base Cretaceous-Jurassic carbonate surface, a base Triassic-Paleozoic surface, and the Moho (Collier et al., 1994).

The Amposta and Castor well data directly constrain Vp and Vs values in the Tertiary and Cretaceous-Jurassic carbonate sections, with some additional measurements in the Triassic and upper Paleozoic sections. Thus, we used these data to develop depth-dependent velocity (Vp) model for these three units described by:

Tertiary:

$$Vp =< 6000: Vp = 1564 \text{ m/s} - 1.28 Z \quad (2.1)$$

$$Vp > 6000: Vp = 6000 \text{ m/s} + 0.227 (Z_{6000} - Z) \quad (2.2)$$

where $Z_{6000} = (1564 - 6000)/1.28$ m and Z is elevation in m (positive up)

Cretaceous-Jurassic:

$$Vp = 5340 \text{ m/s} - 0.227 Z \quad (2.3)$$

Triassic-Paleozoic:

$$Vp = 1.92 * Vs_{CSIC}$$

where Vs_{CSIC} is interpolated from Gaite et al. (2016).

We developed a volumetric grid of the study area consisting of ≈ 35 million cells, corresponding to a spatial resolution of 1 km by 1 km (horizontal) and 100 m (vertical). The grid was parameterized using the sediment velocity relations. In parallel, we used dipole sonic logs to constrain the relationship between Vp and Vs, and used the following relationship to generate a parallel shear wave model:

Tertiary:

$$Vs =< 3000: Vs = 500 \text{ m/s} - 0.833 Z \quad (2.4)$$

$$Vs > 3000: Vs = 3000 \text{ m/s} + 0.111 (Z_{3000} - Z) \quad (2.5)$$

where $Z_{3000} = (500 - 3000)/0.833$ and Z is elevation in m (positive up)

Cretaceous-Jurassic:

$$Vs = 2667 - 0.111 Z \quad (2.6)$$

Triassic-Paleozoic:

$$Vs = Vs_{CSIC} \quad (2.7)$$

where Vs_{CSIC} is interpolated from Gaite et al. (2016)

We then embedded the velocity model in the background model of Gaite et al. (2016). To ensure a smooth transition between these velocity structures, we define a several-kilometer wide transition zone around the local model over which velocities were smoothed. This resulted in a model that describes velocity structure in both the sedimentary basin and the mid- to lower-crust that encompasses the Castor field and the local seismograph stations used in our analysis (Figure 2.8). Notably, the model describes a distinct velocity inversion beneath Castor that is consistent with the transition from Cretaceous-Jurassic carbonates to underlying Triassic clastic strata.

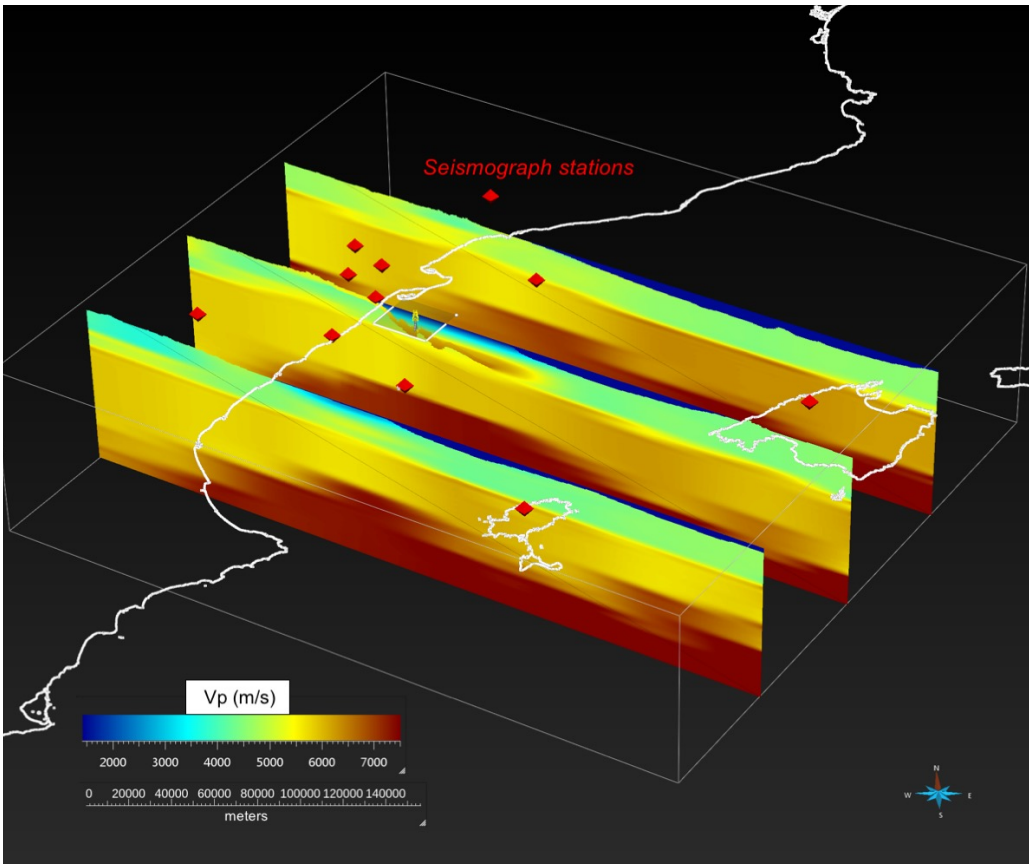

Figure 2.8: Perspective view of our 3-D velocity model showing Vp. The model is embedded in the regional velocity model of Gaite et al. (2016), and encompasses several of the seismic stations used in our analysis of the 2013 earthquake sequence.

2.4. Tectonic Activity of the Amposta Fault

As part of our structural analysis, we also assessed geological constraints on the activity of the Amposta fault system. The southern segment of the fault system and its hanging wall splays offsets geological strata to the seafloor, indicating recent (late Quaternary or Holocene) tectonic activity (Figure 2.9). This is consistent with regional studies and fault compilations that have described the Amposta as a tectonically active fault (García-Mayordomo et al., 2012; Perea et al., 2012). Notably, the northern extent of the Amposta fault does not extend upward and offset these young geological strata. Rather, it terminates upward into older Tertiary strata at a depth of about 2 km. This indicates that the northern portion of the fault is tectonically inactive. Notably, this south-to-north transition in fault activity occurs at the location where the map trace of the fault changes trend from northwest to northeast near the Castor field. At this juncture, recent stratigraphic offsets on the southern Amposta fault appear to transfer onto the series of hanging wall splay faults that we have documented (Figure 2.9).

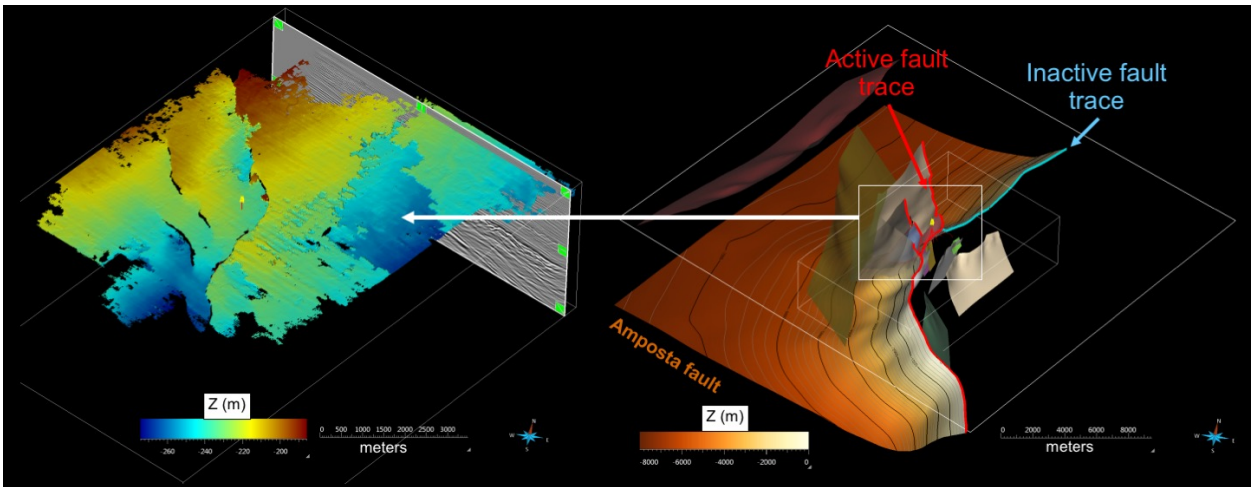

Figure 2.9: (Left) Perspective view of a shallow (≈ 230m below sea level) stratigraphic horizon mapped in the 3-D seismic reflection data showing offsets along the southern Amposta fault and its hanging wall splays. (right) 3D perspective of Amposta fault showing location of offset horizon along its active trace. North of this area, the Amposta fault becomes inactive.

In subsequent stages of our analysis, we will explore the reservoir induced fluid pressure and stress changes, as well as the occurrence of seismicity, relative to the tectonic activity of these various segments of the Amposta fault.

2.5. Preparing the Model for Grid Generation

In order to facilitate the incorporation of the structural model into a mesh that could be used for the coupled flow–geomechanical analysis, we were required to make some simplifications to the representations of the faults. These changes are outlined in Table 2.1 and were motivated by the desire to avoid complex or elongated tetrahedral elements that would compromise the quality of the calculations. We made an effort to maintain the representations of the Amposta fault and key reservoir faults, while eliminating other smaller fault segments. In addition, we merged select segments or splays of small displacement faults to generate continuous surface representations. Merged faults included smaller segments of the Amposta fault splays and several reservoir faults. We consider these changes to the fault representations as not having a significant impact on our results or conclusions. Figure 2.10 illustrates the model components that we used to generate the computational mesh.

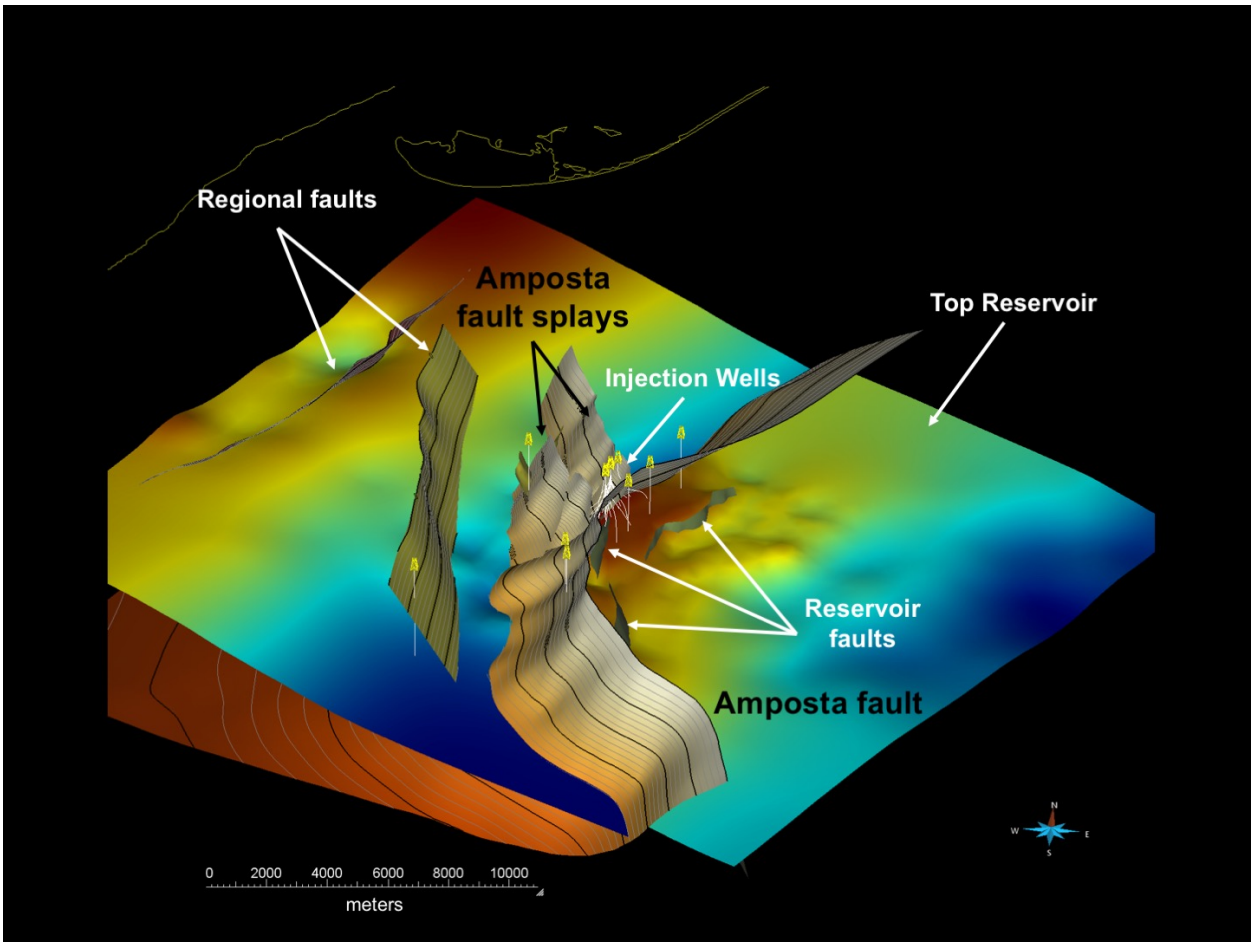

Figure 2.10: Perspective view of the complete structural model.

Table 2.1: Summary of changes made to faults for mesh generation. Meshed faults were not modified from the structural model. Omitted faults were not included. Merged and Extended faults were generated to simplify the mesh representations.

Meshed faults
Castor-Amposta_fault
Castor-W_Main_fault
Castor-m1_F235
Castor-m1_Splay1B_anti1
Castor-m1_Splay1B_anti2
Castor-m1_Splay2B_anti1
Castor-m1_Splay3
Castor-m2_Splay1AB
Castor-m2_Splay2AB
Castor-m_F10
Castor-m_F11
Castor-m_F14
Castor-m_FEastBounding
Castor-m_SouthFault

Omitted faults
F1
F4/6/7/8/9/12/13 (not modeled)
W_PlioQuF1
Splay2C
Splay4/5
F1011 more gently dipping alternatives

Merged faults
F2, F3, F5, into F235
Splay1A and B into Splay1AB
Splay2A and B into Splay 2AB
combined picks of Splay3 patches merged into single fault
SEFault merged with Amposta
SouthFault1/2 merged into SouthFault

Extended faults
Splay1/2/3 across Amposta fault
Northern Amposta to sea level

Chapter 3. Seismicity Analysis

The main goals of the analysis that we performed on the seismic data were:

1. To review the results of work by previous investigators, including IGN (2013), Cesca et al. (2014), and Gaite et al. (2016);
2. To estimate the uncertainties in the locations and faulting mechanisms (moment tensors) of the earthquake sequence;
3. To determine to what extent the seismicity can be associated with the faults in the Geologic Structural Model;
4. To evaluate the evolution of the earthquake sequence in space and time; and
5. To determine the relationship between the seismicity and the stress changes in space and time predicted by the geomechanical model.

The seismicity observed during and subsequent to the termination of injection at Castor occurred offshore and there were no seismic stations specifically set up to monitor the seismicity. This means that the distribution of seismic stations in the vicinity of the recorded seismicity is poor, which leads to large uncertainties in the analysis of the seismic data. An optimal scenario for observing seismicity is when stations completely surround the zone of seismicity and many stations are located at distances of no greater than twice the depth of the events. Since the event depths at Castor are mostly less than 10 km deep, stations located within 10 km of the platform are required for reliable locations. The closest station to the Castor platform is station ALCN, which is located approximately 27 km from the platform. In addition, the azimuthal distribution of stations surrounding the events is limited since most stations are located on land and are generally west of the platform. Two island stations, ETOS on Mallorca, and EIBI on Eivissa, are to the East and South of the platform but are each more than 100 km away, so they did not obtain high signal-to-noise ratio recordings for the earthquakes (island stations are notoriously noisy). Our ability to reliably determine the locations and moment tensors of events at Castor is severely limited by the inadequate station distribution.

We present a discussion of the work that has been done by others on the seismic data to locate events, to evaluate the temporal evolution of the seismicity, and to determine the sense of faulting, which is known as the focal mechanism or moment tensor. We then present results of our own analysis and interpretation of the data

3.1 Overall Approach

We began with an assessment of data and an evaluation of work by previous investigators. We received the EBRO Observatory earthquake catalog, including arrival time picks for events within the Castor region. We also received waveform data. All data were provided to us by Enagas. Our work began with an assessment of quality of the arrival time picks in the EBRO catalog. We decided to proceed using the EBRO travel time picks to locate the events. Events were located using a fit-for-purpose location algorithm that was written for this project. This algorithm uses a grid search, and weights the observed S-P times (the time

difference between the arrivals of the first-arriving compressional wave and the later arriving shear wave) equally with the observed P and S times. The reason for this relatively unconventional approach was that we initially observed that the S-P times during about the first 10 days of the sequence showed considerable variation, but that the time differences were almost constant later in the sequence. We wanted a location approach that would make use of this important observation. Locations were determined using two velocity models as will be described below. We also evaluated the moment tensor solutions (provide information about fault orientation and slip direction) obtained by previous investigators. We then proceeded to use a number of approaches for constraining the moment tensor solutions. Finally, we discuss the evolution of the seismic sequence in space and time.

3.2. Earthquake Locations

3.2.1. Previous Studies

Locations have been determined by the IGN (2013), by the EBRO Observatory, and by two independent research groups (Cesca et al., 2014; Gaite et al., 2016). Figure 3.1 is a map of the region showing the locations determined by IGN (2013). Cesca et al. (2014) located subsets of the earthquakes using approaches that are intended to give either reliable absolute locations or reliable relative locations of the events. They used a flat-layered velocity model to calculate expected arrival times. The velocity model is derived from a global earth model that has information specific to the Castor region (Laske et al., 2000). The 73 event locations that they determined using their absolute location approach were found to occur mostly to the north of the Castor platform, although a few occur to the south. The event depths range from about 1 to 3 km. Their results are very different from those reported in the EBRO catalog, which show events trending NW-SE and lying both east and west of the platform. The 51 events that were located by Cesca et al. (2014) using a relative location technique were tightly clustered and followed a trend going NNE-SSW. The depths of these locations were also in a range of 1- 3 km.

Gaite et al. (2016) used a 3D velocity model derived from surface wave dispersion curves developed by using seismic interferometry on noise. Their locations fall along a trend that is more similar to that of the EBRO catalog locations, e.g. a NW-SE trend surrounding the Castor platform. The depths of the locations determined by Gaite et al. (2016) are considerably larger than those determined by Cesca et al. (2014) and range from a few km to as great as 15 km.

3.2.2. Evaluation of Arrival Times of Phases

We used seismic data from the EBRO Observatory. We obtained continuous trace records from 9 stations (see map, Figure 3.1). A limited amount of data were provided for a tenth station but those data were not used because of the small amount of data and the close proximity of that station to a cluster of other stations for which we had considerably larger datasets. In addition, we were provided with the EBRO location catalog that contained the arrival time picks at the stations and the locations of the events as determined from those

picks by the EBRO Observatory. We used the waveforms for evaluating the arrival time picks in the catalog and for determining the moment tensor/focal mechanism of the largest event that occurred on October 1, 2013. The catalog contained picks and locations for approximately 1000 events that occurred between September 5 and October 30, 2013. We are not certain how the catalog picks were obtained from the trace data. However, our visual comparison of the picks with the waveforms leads us to believe that there is an uncertainty of the picked P and S arrival times of 0.1 to 0.5 seconds, depending on the event size, the station, and the phase. We did not attempt to quantify the pick uncertainty and we did not attempt to improve the pick quality. Manual repicking of the phases is something that might improve the quality of the locations. However, given the poor station distribution and the large uncertainty in the velocity model, we decided that the pick quality was adequate for our subsequent analysis.

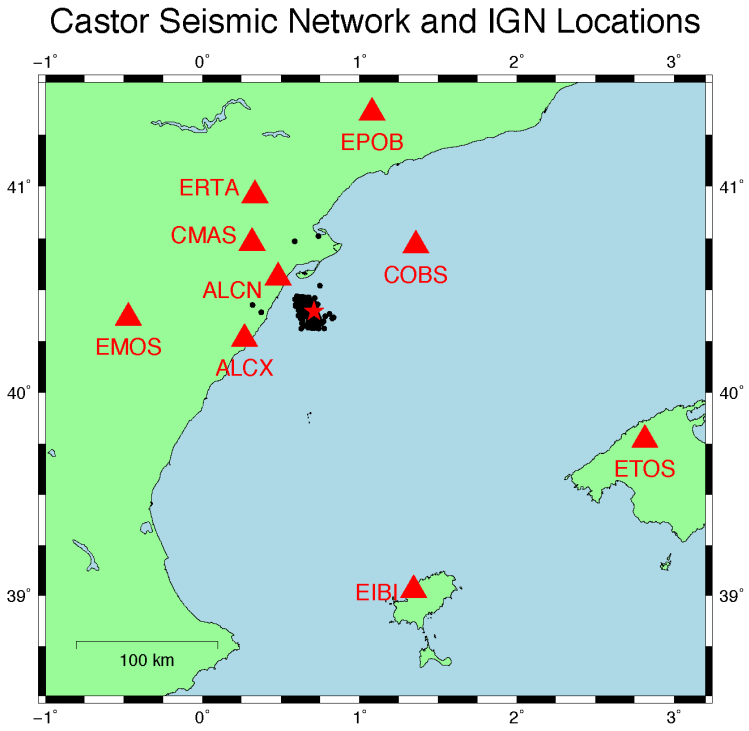

Figure 3.1: Map showing the locations of the stations in the seismic network that we used for locating the events at Castor. The location of the Castor platform is shown with a red star. Black dots near the platform are the locations of events determined by the IGN.

Earthquakes are generally located by matching the measured arrival times of various phases with times predicted using a given velocity model. Predicted times are a function of the earthquake location and the velocity model. We begin by an evaluation of the arrival time data available in the EBRO catalog. Generally the arrival times of the P (compressional) and S (shear) phases are used. Since these waves travel at different velocities, the difference in the arrival times of the two phases depends strongly on the distance between the recording station and the event. Figure 3.2 shows a plot of all

waveforms recorded at station ALCN, the closest station to the Castor platform. The left side shows the vertical component waveforms and the right side shows the transverse component waveforms. Waveforms are organized by their chronological order of occurrence. Thus, event 1 occurred on September 5, 2013 and event 200 occurred in the middle of the day on September 14. Event 600 occurred on October 1, 2013. All traces are aligned by the P-wave arrival time reported in the EBRO catalog. Time 0 is the reported arrival time. The change in character of the traces from before the marked P-wave at 0 seconds arrival to after the P-wave arrival indicates that the pick quality is reasonably good. By evaluating the right hand plot in Figure 3.1, we see that the S-wave arrival times do not vary much relative to the P-wave times; e.g. the difference between the P arrival and the S arrival is roughly 4 seconds. The interesting observation is that the S-waves for events numbered greater than about 250 appear at almost the same time relative to the P-wave arrival times. Before event 250, there seems to be a variation in the S-time relative to the P time. This means that the events that occurred before mid-September, 2013, occurred at a range of distances from ALCN but that the later events occurred at almost identical distances from ALCN.

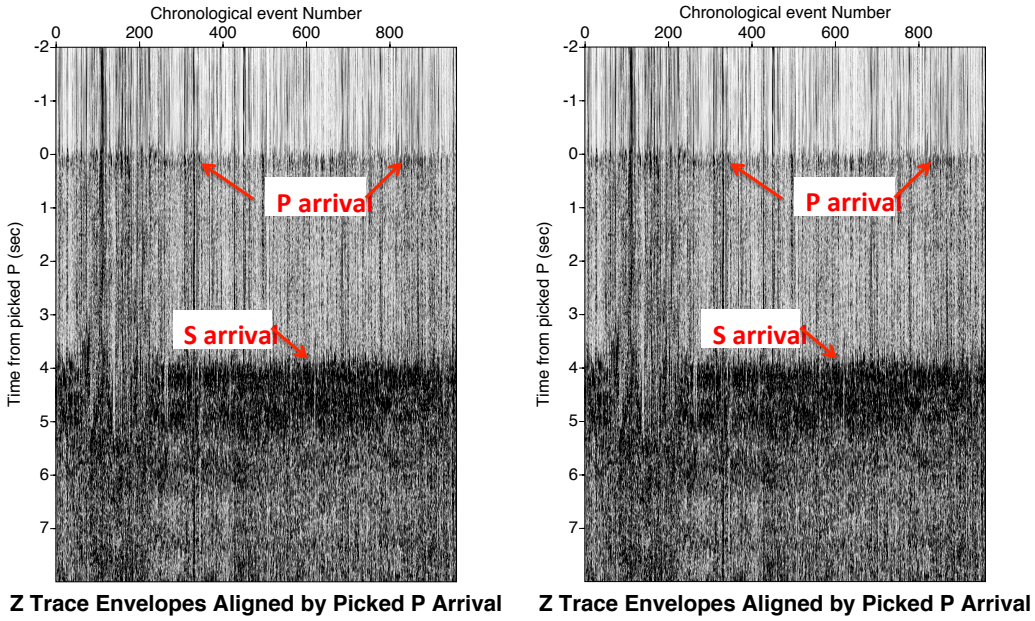

Figure 3.2: Compilation of waveforms of earthquakes at Castor that were recorded at station ALCN (Figure 3.1). Each vertical line represents one earthquake. The traces are aligned on the P-wave arrival time listed in the EBRO seismic catalog. Changes in the character of the image are obvious at the P- and S-arrival times. Left panel shows vertical component traces that highlight the P-arrivals. Right panel shows horizontal transverse component traces that highlight the S-arrivals. Note that the S-arrival times are almost identical after about event 250 indicating that events after that one are located at a nearly constant distance from station ALCN. Events before about event 250 show variable S-arrival times indicating that their distances from ALCN vary from event to event.

We have examined plots similar to the one shown in Figure 3.2 but for other stations. One notable observation is that the S-P time for all events is almost constant at station EPOB,

that is located NNE of the Castor platform. This means that the event distances did not change much relative to station EPOB.

From our basic evaluation of arrival times from the waveforms, we conclude that events before mid September occurred at a range of distances from station ALCN, but that they occurred at almost a constant distance from station EPOB. This is consistent with a NW-SE trend of the event locations. Such simple observations from the raw data will be used later to support our confidence about our locations for the seismic events and the interpretation that we draw from them.

3.2.3. Velocity Model

In addition to the distribution of stations that record earthquakes, reliable knowledge of the velocity structure is essential for determining their locations. The size and depth of the region over which the velocity model must be known increases with the distance between the earthquake and the recording stations. We investigated several velocity models: (1) the flat layered Crust 2.0 model that was used by Cesca et al. (2014), (2) the 3D heterogeneous model that was derived by Gaite et al. (2016) from analysis of surface wave dispersion, (3) a flat layered model derived from the model in Gaite et al. (2016) for the region closest to the Castor Platform, and (4) a 3D heterogeneous model derived from the Geological Structural Model that was developed for the reservoir/geomechanical model in the current project. Model 4 was embedded within a larger 3D velocity model derived from the work of Gaite et al. (2016). The results we will discuss are those obtained using models 3 and 4 since we feel that they are the most reliable representations of the velocities in the region under investigation. Figure 3.3 shows vertical cross sections of the P-wave velocity through the flat layered model (model 3, Figure 3.3a), the heterogeneous model (model 4, Figure 3.3b), and a smoothed version of the heterogeneous model (Figure 3.3c). The smoothed model is the one that we used to trace rays to determine travel times needed for the location study using the heterogeneous model.

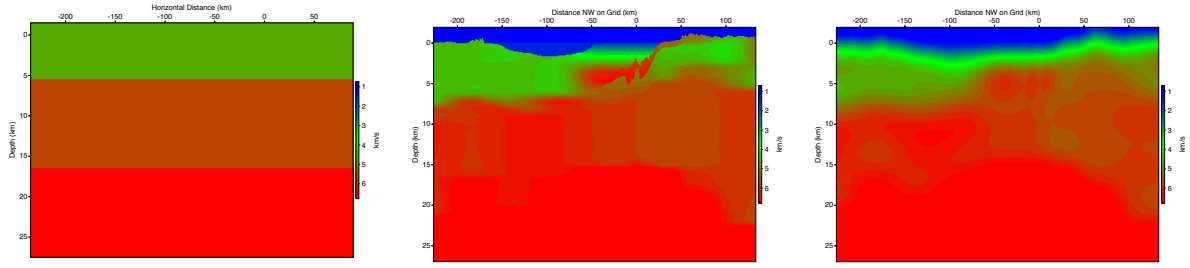

(a) (b) (c)

Figure 3.3: Vertical cross sections of the P-wave velocity models. In each case, the cross section corresponds to a slice trending N59.4 degrees West. The Castor Platform is located at horizontal position 0 km. Note vertical exaggeration. (a) Layered model derived from Gaite et al. (2016); (b) 3D model developed for this study based on detailed geological and geophysical information; (c) Smoothed 3D model used in the ray tracing through (b).

3.2.4. Location Methodology

We used a grid search technique for determining event locations. We chose a grid surrounding the Castor platform extending to distances of approximately 15 km from the platform. The horizontal grid was rotated 59.4 degrees counterclockwise from North, in the same orientation as the grid used for the reservoir/geomechanical model. The depth range was between 0.2 and 20 km. Grid increments were 0.2 km in the three orthogonal directions along the grid, resulting in approximately 2.3 million points in the grid.

For each event, we determined the difference between the observed and predicted arrival times for each point on the grid. We calculated the fit to the P and S arrival times and separately the fit to the difference between the S and P arrival times for each grid point for stations where both P and S wave arrival times are available. The grid point with the best fit to the data was taken as the event location. After determining the locations of all events, we determined an average station residual for each phase at each station from the average misfit between the data for that phase at that station for all events located. This was taken to be a station correction. This station correction was used as an adjustment to the predicted time for the phase at the station in a subsequent iteration of event locations. The station correction procedure was repeated several times. Using station corrections in this manner has been shown to yield more reliable relative locations of events as it takes account of uncertainties in the velocity model, particularly between the station and the event cluster. For this method to work best, the velocity model in the vicinity of the locations should be most reliable. Uncertainties in the velocity models between the region containing the events and each station are accommodated by the station corrections.

3.2.5. Location Results

We show locations determined using the layered velocity model shown in Figure 3.3a. Between 800 and 900 events were reliably located. We considered a location to be reliable if the RMS misfit between measured and predicted arrival time is less than 1 s. Figure 3.4 shows the locations obtained using the Flat layered model

The events located using velocity models (3) and (4) discussed above show broadly similar epicenter distributions and fit the arrival time data almost equally well. These locations place the majority of earthquakes west and northwest of the platform with the cluster aligned in a roughly northwest-southeast orientation. Notably, the IGN (2013) and EBRO catalog locations have a similar northwest-southeast orientation. However, our locations place most earthquakes farther west, closer to the Amposta fault system and its splays. The locations determined in our analysis using the flat layered model are located somewhat closer to the Castor Platform than those determined using our heterogeneous model, and generally less than about 5 km deep. In contrast, the locations determined using the heterogeneous model are deeper, between 5 and 15 km.

The locations occur in two general regions: (1) a dense cluster of seismicity located near the Castor platform and (2) a sparse distribution that trends southeast from the platform. The majority of the events located to the southeast occurred before mid September. These are the events with larger S-P times that were discussed above and referred to in the

caption to Figure 3.2. We are confident that these events occurred further from ALCN than most of the later events because of the larger arrival time differences that can be clearly seen in the waveforms recorded at ALCN.

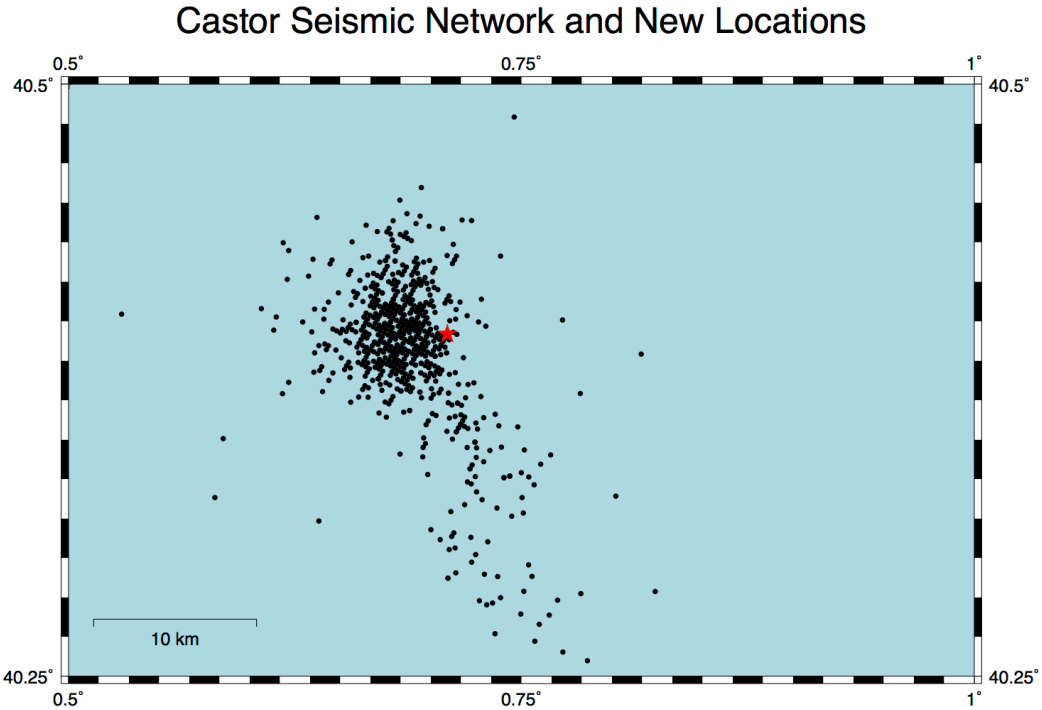

Figure 3.4: Event locations determined using flat layered velocity model. The location of the Castor platform is shown with a red star. (Note that the scale is different from the map shown in Figure 3.1.)

The inadequate station distribution, including the large distance between the stations and the events and the limited range of azimuths of stations around the events, limits our ability to distinguish between the alternative sets of hypocenters that we have developed (as well as those published by others) and determine highly reliable locations that could be used to uniquely identify their source faults. The confidence in the locations is further reduced by the uncertainty in the velocity structure between the events and the stations. Given these uncertainties, we conducted a test where all events were forced to fall along one or more of the faults in the geological structural model that was constructed for the project. The misfit between the measured and predicted arrival times is not significantly worse than when the earthquakes are not constrained to occur along faults. In this case, a majority of the events are found to occur along the Amposta fault, its hanging wall splay faults, or reservoir faults in the vicinity of the platform that are represented in the model (Figure 3.5). When the heterogeneous velocity model is used, event locations are found to occur along the deeper portion of the Amposta fault.

Our analysis leads to the conclusion that it is possible, but not proven, that a majority of the events could have occurred along mapped faults. Another test that we conducted was to determine whether the arrival time data are consistent with the events having occurred

along the shallow Eastward dipping fault in the moment tensor solution of Cesca et al. (2014). (There is no indication of this fault's existence in the 3D seismic data, it is not compatible with the geologic sequence in the region, and it is therefore absent from our geological structural model. Cesca et al. (2014) sketched the fault based on the two-way travel time from active seismic imaging, but when converted to depth this fault would be more steeply dipping, which would then be incompatible with their preferred focal mechanism). We find that the arrival time data are not consistent with more than a very small number of events having occurred along this postulated fault.

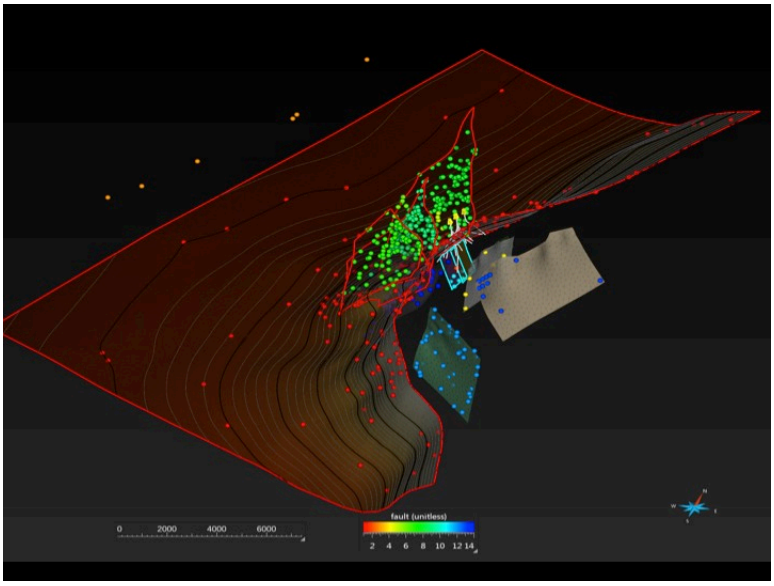

Figure 3.5: 3D perspective view of the Castor structural model, showing earthquakes relocated to the fault surfaces using the layered velocity model. Earthquakes associated with each fault are assigned a unique color. Note that events occur along the Amposta fault system and select reservoir faults.

3.3. Seismic Energy Release vs. Time and Locations of the Largest Events

The seismic energy released during an earthquake sequence is generally dominated by the largest events. Figure 3.6 shows the seismic energy release *vs.* time for the Castor sequence. The first recorded event occurred on September 5. Waveforms for the first four events in the sequence, which all occurred on September 5, are almost identical, indicating that their locations are nearly coincident. Compared to the energy released by the overall sequence, the energy released through September 24 was small. The energy release did not increase substantially until the first large event on September 30. After that event, the energy release is dominated by a small number (6) of rather large events. These six earthquakes have seismic waveforms with almost identical long period components, indicating that they (a) likely have the same focal mechanism, and (b) occurred very close to one another. The locations of these six events are shown in Figure 3.7.

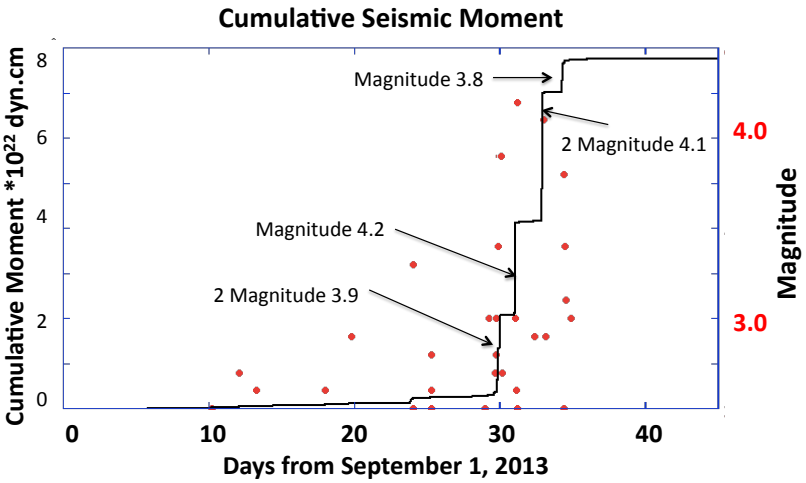

Figure 3.6: Cumulative seismic moment (black) calculated using event magnitudes (shown in red) from the EBRO seismic catalog.

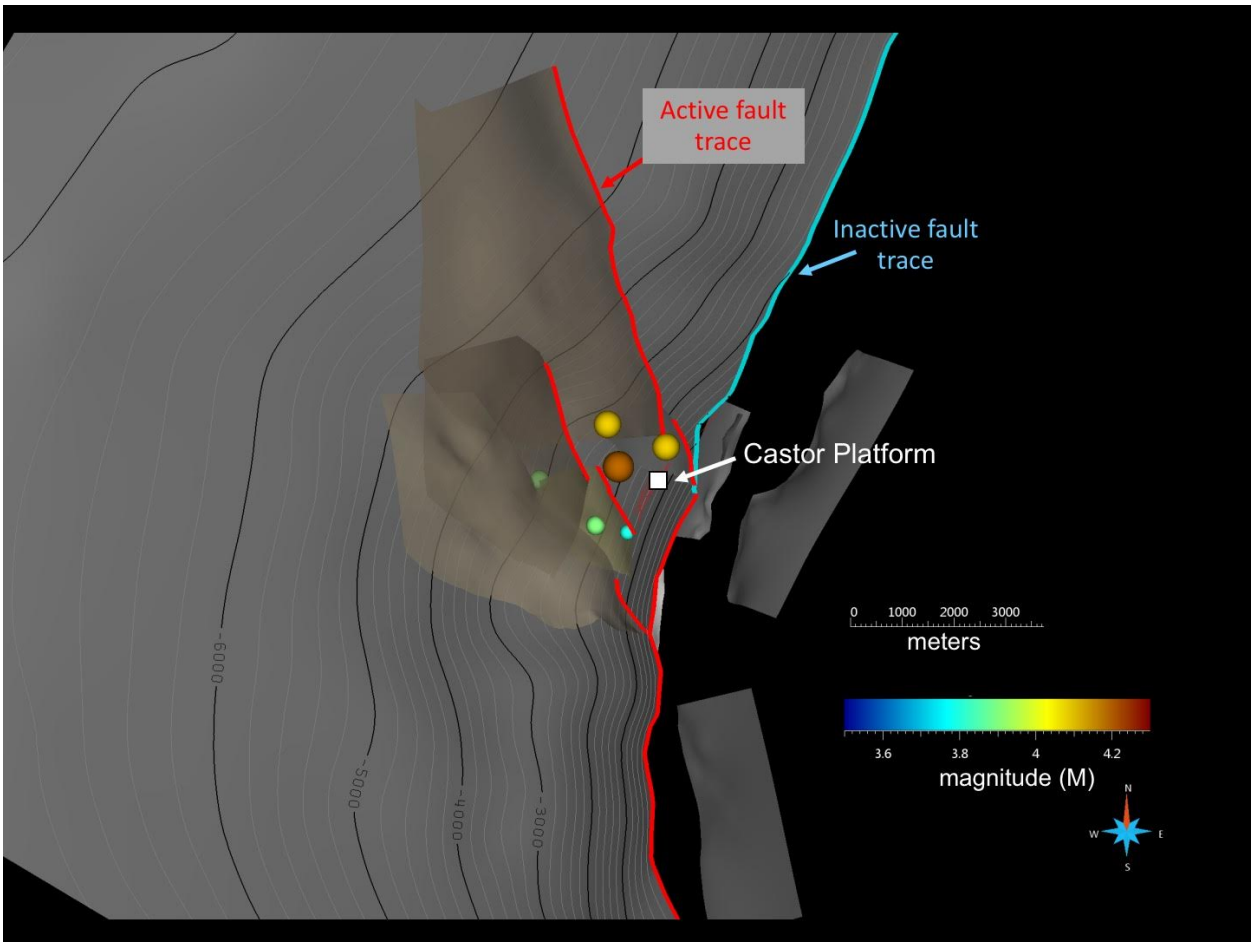

Figure 3.7: Perspective views of the locations of the six events with magnitude between 3.8 and 4.3. Select faults in the structural model are also shown.

3.4. Moment Tensor Inversion

3.4.1. Previous Studies

Moment tensors were determined by IGN (2013), Cesca et al. (2014), Villaseñor et al. (2016), and Saló et al. (2017). Figure 3.8a-c shows the moment tensors found for the main shock on October 1, 2013 by three of the four studies. In all three cases, moment tensors were obtained by waveform fitting. The results of IGN (2013) and Saló et al. (2017) are rather similar, while the result obtained by Cesca et al. (2014) is significantly different from the other two. Moment tensor solutions define two possible planes of slip for the earthquake. Seismic data can only provide information about which plane was the actual plane of slip by considering a finite rupture model, which is possible only when the azimuthal distribution of stations is good. All three moment tensor solutions shown in Figure 3.8 have one fault that trends roughly NW and is close to vertical. All three moment tensor solutions also have a plane that trends NE. However, the plane found by Cesca et al. (2014) has a very shallow dip, whereas the planes identified by IGN (2013) and Saló et al. (2017) are nearly vertical and dipping to the SE. Cesca et al. (2014) argue that the shallow-dipping NE-trending fault was the plane of slip for the event.

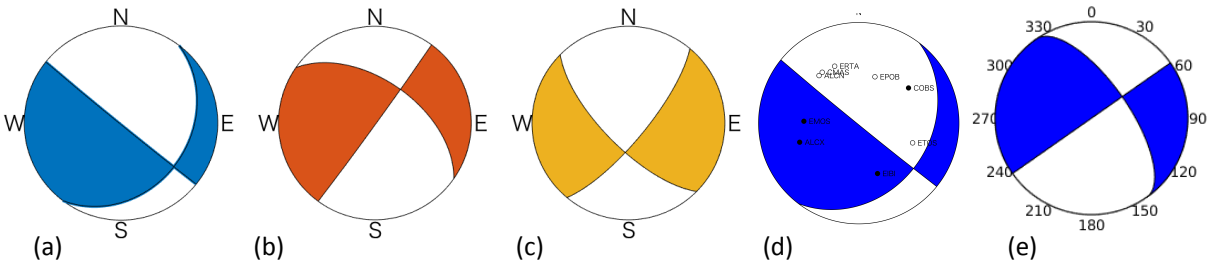

Figure 3.8: Lower hemisphere projection of moment tensor solutions for the Magnitude 4.3 event that occurred on October 1, 2013. The compressive and dilatational quadrants are shown as white and black, respectively. Result determined by (a) Cesca et al. (2014) using waveform fitting, (b) IGN (2013) using waveform fitting, (c) Saló et al. (2017) using waveform fitting. (d) Solution obtained by Cesca et al. (2014) over which we have superimposed the first motion directions where black means compressive first motion and open circle means dilatational first motion. (e) Our solution obtained by fitting waveform data using our layered velocity model and the location of the event determined using station corrections.

3.4.2. Moment Tensor Analysis of Magnitude 4.3 Event on October 1, 2013

We find that the long-period component of the waveforms from the six largest events with magnitudes between 3.8 and 4.3 are quite similar. The similarity leads us to conclude that all of these events occurred on one fault. The waveforms are different from those of the four similar events at the beginning of the earthquake sequence. We evaluated the focal mechanism of the largest of these events, the magnitude 4.3 event that occurred on 1 October, 2013 using two approaches. The first used the classical approach of fitting the directions of first motions at the stations. The second used waveform fitting. Fitting of first motions of events is a relatively straightforward approach for finding the focal mechanism (a simplified moment tensor) that is less dependent on a reliable knowledge of the velocity

structure than is waveform fitting. First motion directions can be easily measured from waveform data and uncertainties in the measurements are easily incorporated into the analysis.

We use the term focal mechanism to represent the two possible slip planes for an earthquake. A moment tensor solution includes the focal mechanism and some estimate of the size of the earthquake. First motion polarity data cannot provide information about the earthquake size unless the first motion amplitudes are also measured and interpreted.

Figure 3.8d shows the observed first motions (up=compressive or down=dilatational) plotted on a lower hemisphere focal sphere along with the moment tensor from Cesca et al. (2014). A good fit of the moment tensor to the first motion data would require that all black and white dots representing directions of motions at the stations fall within the same color regions of the focal sphere that are shaded and white, respectively. All observed first motion data are consistent with their moment tensor solution except that observed at station COBS. Since the measured direction of first motion at COBS is clear and strong, we cannot ignore it and we must conclude that the moment tensor is inconsistent with the data. The difference between the Cesca et al. (2014) moment tensor and the first motion at COBS may not be surprising since they did not use the data from COBS in their moment tensor determination.

IGN (2013) also determined focal mechanisms using first motions. The mechanism they find for the main shock using first motions is similar to those shown in Figure 3.8b and 3.8c except that the NNE trending fault dips to the West, rather than dipping to the East as shown in Figure 3.6. Their solution found using first motions is very well constrained and uses data from far more stations than is shown in Figure 3.8d. The mechanism that they find using first motions is close, but not identical to the one they obtain using waveform fitting. The mechanism shown for IGN (2013) is taken from the report and is slightly different from the one reported by Cesca et al. (2014) as having come from the IGN online catalog.

We examined a suite of possible focal mechanisms that fit all the observed first motion data. We have less confidence in the measurements of first motions at island stations ETOS and EIBI. These stations are located further from the earthquakes and the signal-to-noise of the first motions is smaller than at the other stations. If we consider that one or both of these first motions are incorrectly depicted in Figure 3.8d, a wider range of possible focal mechanisms are possible. The set of solutions that are consistent with all first motions except those at ETOS and EIBI look quite similar to the solutions shown in Figure 3.8(b,c), the moment tensor solutions of IGN (2013) and Saló et al. (2017). We do not find any focal mechanism solution like the one obtained by Cesca et al. (2014) that is consistent with the high-quality first motion data.

To further investigate the moment tensor, we performed waveform fitting of the data at 8 stations (EIBI, ALCX, EMOS, ALCN, CMAS, ERTA, EPOB, COBS) and the first motion at station ETOS. We used a fitting approach that was developed by Li et al. (2011). The waveforms we fit were filtered between 2 and 5 Hz. This is much higher frequency range than that used by

Cesca et al. (2013), which was 0.05 - 0.1 Hz and the one used by Saló et al. (2017), 0.02 - 0.1 Hz. The use of higher frequencies makes our result more dependent on the velocity structure. The advantage of using higher frequencies is that the signal amplitude in the 2-5 Hz band is more than an order of magnitude higher than that in the lower band used by others. Another reason for choosing the higher frequency band is that the wavelengths in the 2-5 Hz band are on the order of kilometers whereas the wavelength at 0.1 Hz is on the order of 10's of km, roughly the same as the distances between the event and the stations. Using the long wavelength range (low frequencies) requires careful consideration of near field terms in the calculation of synthetic seismograms for use in the moment tensor solution. Our fit of the predicted waveforms to the data is measured in several ways, and the weighted sum of those misfits is minimized to find the resulting moment tensor (see, e.g., Li et al., 2011). We used a number of different weighting schemes to emphasize different characteristics of the fits to the data. Figure 3.8e shows one of the mechanisms we obtained. This mechanism shows a fault striking NE-SW that dips to the West and a NW-SE striking fault that is almost vertical but which dips slightly to the NE. This mechanism is very similar to the one found by IGN (2013) using first motion data from a large number of stations. The NE-SW striking fault orientation is consistent with the Amposta Fault, as well as being consistent with the 3D relative locations of the six largest events, which align on a plane dipping northwest. This mechanism differs somewhat from those determined by others who used waveform inversion, with the steep NW-SE plane dipping to the west, rather than to the east. However, within uncertainties, our result agrees with the solutions by IGN (2013) and by Saló et al. (2017), but not with the solution of Cesca et al. (2014).

3.5. Spatial and Temporal Evolution of the Earthquake Sequence

The distribution of hypocenters shown in Figure 3.4 correlates well with the tectonically active sections of the Amposta fault system. However, seismicity is distributed over a larger region than is affected significantly by the stress changes associated with pressurizing the reservoir. This raises the question of whether the *initiation* of the sequence is related to operations. To answer this question, we examined the hypocenter locations as a function of time during the sequence. We found that the earliest events in the sequence were located within a few kilometers (comparable to uncertainties in absolute locations) of the Castor platform and therefore have a high probability of being triggered. The more broadly distributed earthquakes in the approximately 10 days immediately following these "induced foreshocks" appear to be an aftershock sequence, with the initial events triggering subsequent earthquakes, predominantly along the tectonically active segments of the Amposta fault system, in contrast to far fewer events triggered along the tectonically inactive segments. Finally, the six largest events, in which most of the moment was released, were concentrated in the region affected by production (Figure 3.7).

3.6. Synthesis of the Seismicity Analysis

Our major conclusions from the analysis of the seismic data are as follows:

1. Seismicity initiated near the platform, rapidly expanded into a spatially distributed zone, then contracted to a tighter cluster surrounding the 6 largest events that occurred after injection stopped.
2. Seismic energy release is dominated by these six relatively large events. These large events are located very close - within a few km of each other. The large events likely occurred along a single NW dipping plane that could be coincident with the Amposta fault. Our locations place these events near the Castor platform.
3. Most events can be associated with faults that are represented in the geological model developed for this project.
4. Event relocations and moment-tensor solutions, within uncertainties, agree with those from IGN, but our preferred moment tensor has a plane that dips to the NW, aligned with the distribution of the largest events.
5. There is very little evidence that the largest events occurred along the low-angle eastward dipping fault that was proposed by Cesca et al. (2014).

Chapter 4. Coupled Flow-Geomechanics Modeling

4.1. Overall Approach

Our dynamic simulation strategy is based on coupling flow and geomechanical models into one simulation framework. The role of the coupled reservoir flow and geomechanical simulation in the integrated approach for this project in shown in Figure 4.1.

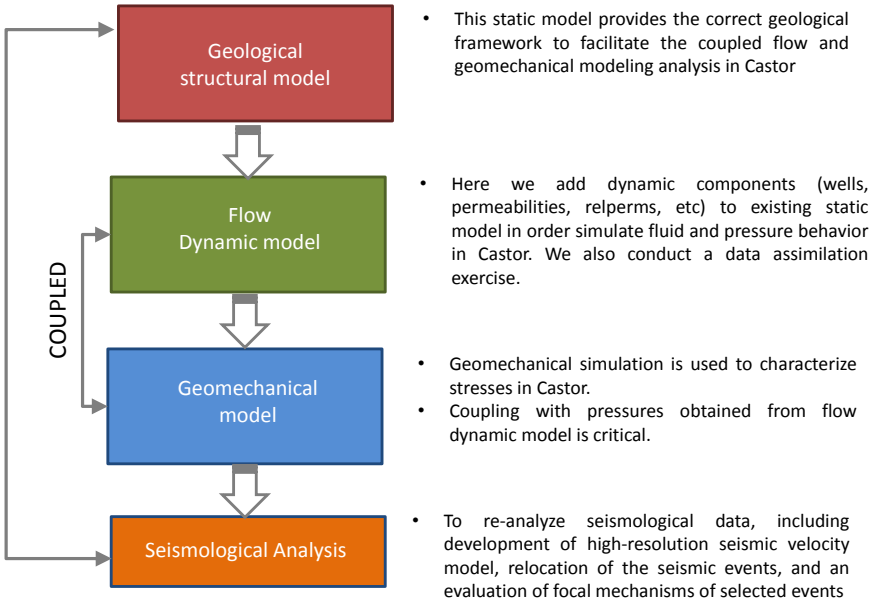

Figure 4.1: Coupled flow-geomechanics simulation within integrated approach for this project.

In what follows we first present the mathematical and computational aspects of the simulation approach, and then describe the specific computational model for Castor, including the mesh, the simulation parameters, and the performance of the model during the different periods of reservoir operations in the Amposta field and Castor gas storage.

4.2 Mathematical Formulation of Coupled Multiphase Poro-Mechanics

4.2.1. Mathematical Formulation

An important aspect of the modeling is the coupling between flow and deformation. These two physical problems are coupled both ways, as described in the classical theory of poromechanics (Biot, 1941; Coussy, 1995, 2004; Jha and Juanes, 2014).

Under the quasistatic assumption for earth displacements, the governing equation for linear momentum balance of the solid/fluid system can be expressed as

$$\nabla \cdot \boldsymbol{\sigma} + \rho_b \boldsymbol{g} = \mathbf{0}, \tag{4.1}$$

where $\boldsymbol{\sigma}$ is the Cauchy total stress tensor, $\boldsymbol{g}$ is the gravity vector, and $\rho_b = \phi \sum_{\beta}^{n_{\text{phase}}} \rho_\beta S_\beta + (1-\phi)\rho_s$ is the bulk density, ρ_β and S_β are the density and saturation of fluid phase β, and ρ_s is the density of the solid phase, ϕ is the true porosity, and n_{phase} is the number of fluid phases. The true porosity is defined as the ratio of the pore volume to the bulk volume in the current (deformed) configuration. Assuming that the fluids are immiscible, the mass-conservation equation for each phase α is

$$\frac{dm_\alpha}{dt} + \nabla \cdot \boldsymbol{w}_\alpha = \rho_\alpha f_\alpha, \tag{4.2}$$

where the accumulation term dm_α/dt describes the time variation of fluid mass relative to the motion of the solid skeleton, $\boldsymbol{w}_\alpha$ is the mass-flux of fluid phase α relative to the solid skeleton, and f_α is the volumetric source term for phase α. The two balance equations (4.1) and (4.2) are coupled by virtue of poromechanics. On one hand, changes in the pore fluid pressure lead to changes in effective stress, and induce deformation of the porous material—such as ground subsidence caused by groundwater withdrawal. On the other hand, deformation of the porous medium affects fluid mass content and fluid pressure. The simplest model of this two-way coupling is Biot's macroscopic theory of poroelasticity (Biot, 1941; Geertsma, 1957; Coussy, 1995). In the remainder of this section we provide the mathematical description of poroelasticity for multiphase fluid systems.

In the multiphase or partially saturated fluid system, it is not possible to linearize the equations of poroelasticity around a reference state because (Coussy, 1995):

1. Gases are very compressible,
2. Capillary pressure effects are intrinsically nonlinear, and
3. Phase saturations vary between 0 and 1 and, therefore, a typical problem samples the entire range of nonlinearity.

Therefore, following Coussy (1995), we use the incremental formulation of poromechanics for multiphase systems, which does not assume physical linearization of total stress from the initial state to the current (deformed) state. We make a modeling assumption that allows us to express the deformation of a multiphase porous material in terms of the increment in applied total stresses and internal fluid pressures. We adopt an effective stress formulation in the multiphase poromechanics (Bishop, 1959; Bishop and Blight, 1963) because constitutive modeling of porous materials is usually done in terms of the effective stress. Under this formulation, we split the total stress on the porous material into two parts: one that is responsible for deformation of the solid skeleton (the effective stress), and another component that is responsible for changes in the fluid pressures,

$$\delta\boldsymbol{\sigma} = \boldsymbol{C}_{dr} : \delta\boldsymbol{\varepsilon} - \sum_{\beta} b_\beta \, p_\beta \mathbf{1}, \tag{4.3}$$

where b_β are the Biot coefficients for individual phases such that $\sum_\beta b_\beta = b$, where b is the Biot coefficient of the saturated porous material. It is common to further assume that b_β are

proportional to the respective saturations S_β (Lewis and Sukirman, 1993; Coussy et al., 1998; Lewis and Schrefler, 1998).

The effective stress concept allows us to treat a multiphase porous medium as a mechanically equivalent single-phase continuum (Khalili et al., 2004; Nuth and Laloui, 2008). The appropriate form of the effective stress equation in a multiphase system is still an active area of research (Gray and Schrefler, 2001; Coussy et al., 2004; Nuth and Laloui, 2008; Vlahinic et al., 2011; Nikooee et al., 2013; Kim et al., 2013). Here we use the concept of equivalent pressure (Coussy et al., 2004) in the effective stress equation (Eq. (4.3)),

$$p_E = \sum_\beta S_\beta p_\beta - U, \tag{4.4}$$

where $U = \sum_\beta \int p_\beta dS_\beta$ is the interfacial energy computed from the capillary pressure relations (Kim et al., 2013). The equivalent pressure accounts for the interface energy in the free energy of the system, and leads to a thermodynamically consistent and mathematically well-posed description of the multiphase fluid response to the solid deformation (Kim et al., 2013). For a system with two phases, the wetting phase *w* and the non-wetting phase *o*, the capillary pressure is

$$P_c(S_w) \equiv P_{wo}(S_w) = p_o - p_w, \tag{4.5}$$

and the interfacial energy is $U = \int_{S_w}^{1} P_{wg} dS$. Assuming $b_\beta = bS_\beta$ (Lewis and Sukirman, 1993; Coussy et al., 1998; Lewis and Schrefler, 1998), and using Eq. (4.4) in Eq. (4.3), we obtain the stress-strain relation- ship for multiphase linear poroelasticity:

$$\delta\boldsymbol{\sigma} = \delta\boldsymbol{\sigma}' - b\delta p_E \mathbf{1}, \qquad \delta\boldsymbol{\sigma}' = \boldsymbol{C}_{dr} : \delta\boldsymbol{\varepsilon}. \tag{4.6}$$

Once we have a definition of the effective stress in multiphase systems, we now express the change in the fluid mass in terms of the mechanical deformation and the change in the fluid pressures. In the deformed configuration, the mass of phase α per unit volume of porous medium is

$$m_\alpha = \rho_\alpha S_\alpha \phi (1 + \varepsilon_v), \tag{4.7}$$

Note that, by definition, the sum of all fluid phase saturations adds up to 1. For multiphase systems (Coussy, 1995, 2004), we have

$$\left(\frac{dm}{\rho}\right)_\alpha = b_\alpha d\varepsilon_v + \sum N_{\alpha\beta} dp_\beta, \tag{4.8}$$

where $\boldsymbol{N} = \boldsymbol{M}^{-1}$ is the inverse Biot modulus. In a multiphase system, the Biot modulus is a symmetric positive definite tensor $\boldsymbol{M} = [M_{\alpha\beta}]$, and the Biot coefficient is a vector. To determine the coupling coefficients $N_{\alpha\beta}$ as a function of the primary variables (pressure,

saturations, and displacements) and rock and fluid properties we develop an alternate expression for the differential increment in fluid mass. Using Eq. (4.7),

$$dm_\alpha = d\big(\rho_\alpha S_\alpha \phi(1+\varepsilon_v)\big), \tag{4.9}$$

which can be expanded as

$$\left(\frac{dm}{\rho}\right)_\alpha = \phi \frac{\partial S_\alpha}{\partial P_{\alpha\beta}} dP_{\alpha\beta} + \phi S_\alpha c_\alpha dp_\alpha + \phi S_\alpha d\varepsilon_v + S_\alpha d\phi, \tag{4.10}$$

where c_α is the compressibility of the fluid phase α, and $\partial S_\alpha / \partial P_{\alpha\beta}$ is the inverse capillary pressure derivative. Above, repeated indices do not imply summation and we have assumed infinitesimal deformations. We can express the increment in porosity $d\phi$ as a function of the volumetric effective stress $d\sigma'_v$ to obtain a closed-form expression of Eq. (4.10). Let $V_s = V_b - V_p$ be the volume of the solid matrix, and $d\varepsilon_{sv} = dV_s/V_s = d\sigma_{sv}/K_s$ be the volumetric dilation of the solid matrix, where σ_{sv} is the volumetric matrix stress. From an expansion of $d\phi$ we can write the incremental form of strain partition as

$$(1-\phi)d\varepsilon_v = (1-\phi)d\varepsilon_{sv} + d\phi. \tag{4.11}$$

Similarly, the volumetric Cauchy total stress can be partitioned into the volumetric matrix stress and the fluid pressure as

$$d\sigma_v = (1-\phi)d\sigma_{sv} - \phi dp_E. \tag{4.12}$$

Substituting $d\sigma_{sv}$ from Eq. (4.12) into Eq. (4.11), we obtain

$$d\phi = \frac{b-\phi}{K_{dr}}(d\sigma'_v + (1-b)dp_E). \tag{4.13}$$

Equation (4.13) implies that an increment in porosity is related to increments in volumetric effective stress and fluid pressures. Substituting $d\varepsilon_v$ from Eq. (4.6) and $d\phi$ from Eq. (4.13) into Eq. (4.10) allows us to express the increment in the phase mass as a function of the increments in the total volumetric stress and phase pressures. Equating this to Eq. (4.9) yields the desired expressions for the coupling coefficients $N_{\alpha\beta}$.

Finally, we obtain the multiphase flow equation for phase α in a poroelastic medium by substituting the two constitutive relations, the effective stress equation, Eq. (4.6), and the fluid mass increment equation, Eq. (4.8), in the mass balance equation, Eq. (4.2):

$$\frac{\partial}{\partial t}\left(\rho_\alpha \sum_\beta \left(N_{\alpha\beta} + \frac{b_\alpha b_\beta}{K_{dr}}\right) p_\beta\right) + \frac{1}{K_{dr}}\frac{\partial}{\partial t}(\rho_\alpha b_\alpha \sigma_v) + \nabla \cdot \boldsymbol{w}_\alpha = \rho_\alpha f_\alpha, \qquad \forall \alpha = 1, \dots, n_{\text{phase}} \tag{4.14}$$

The role of N and b as the coupling coefficients among different fluid phases and the solid phase is evident from the above equation. The bulk density, ρ_b, in the mechanical equilibrium equation, Eq. (4.1), also acts as a coupling parameter because it is a function of the porosity and the phase saturations. Because we assume that the fluids are immiscible, the mass-flux of phase α is $\boldsymbol{w}_\alpha = \rho_\alpha \boldsymbol{v}_\alpha$, where we adopt the traditional multiphase-flow extension of Darcy's law (Muskat, 1949; Bear, 1972):

$$\boldsymbol{v}_\alpha = \frac{\boldsymbol{k} k_\alpha^r}{\mu_\alpha}(\nabla p_\alpha - \rho_\alpha \boldsymbol{g}), \tag{4.15}$$

where μ_α and k_α^r are the dynamic viscosity and the relative permeability of phase α in presence of other fluid phases.

Poromechanics of faults. There are two basic approaches to represent faults in a three-dimensional medium: either as a three-dimensional fault zone (e.g., Rutqvist et al., 2008) or a two-dimensional fault surface (e.g., Juanes et al., 2002; Molinero et al., 2002; Ferronato et al., 2008). The advantage of representing faults as surfaces of discontinuity is that they can more faithfully describe the localized (discontinuous) displacement at the fault, and that one can incorporate models of dynamic frictional strength (like the rate- and state-friction model) capable of reproducing runaway fault slip characteristic of earthquakes. Moreover, introducing discrete fault surfaces does not preclude modeling an adjacent fault zone with appropriate rheology.

A central feature of our work is that we treat faults as surfaces of discontinuity embedded in the continuum. We use zero-thickness elements, also known as interface elements or cohesive elements in the finite element literature (Goodman et al., 1968; Beer, 1985; Carol et al., 1985; Gens et al., 1988; Lei et al., 1995), to represent the fault surfaces. Mathematically, the fault surface is treated as an interior boundary between the two adjacent domains. The two sides of the fault surface, which need not be planar, are designated as the '+' side and the '–' side, and the fault normal vector, $\boldsymbol{n}$, points from the negative side to the positive side.

Traditionally, in the Andersonian faulting theory (Anderson, 1951), fault slip is modeled in a "dry environment," that is, in the absence of fluids. While, in some cases, the presence of fluid has been recognized through the effective stress concept, the dynamics of flow was not included for reasons of conceptual and computational simplicity, as well as for the belief that fluid flow played a secondary role in the release of tectonic stresses (Hubbert and Rubey, 1959; Reasenberg and Simpson, 1992). The effect of pore pressure was accounted for by modifying the coefficient of fault friction μ_f (Harris and Simpson, 1992; Harris et al., 1995), an approach later suggested to be "unwise" (Beeler et al., 2000). In the case of mature faults, the fault core permeability can be low due to comminution of grains while the damaged host rock permeability can be high due to fractures (Sibson, 1977, 1986; Chester et al., 1993; Caine and Forster, 1999). In addition, the permeability can vary substantially across the fault during the seismic cycle (Sibson, 1981, 1990). As a result,

pore pressures can be significantly different across the fault (Sibson, 1994; Rice, 1992; Chester et al., 1993).

A difference in fluid pressure across the fault leads to a pressure jump $[\![p]\!]_{\Gamma_f} = p_+ - p_-$, where p_+ and p_- are the equivalent multiphase pressures (Equation (4.4)) on the "positive" and the "negative" side of the fault. One of the key features of the 2-D representation of faults is the ability to reproduce a finite jump in the pressure, $[\![p]\!]_{\Gamma_f}$, across the fault. This pressure jump leads to a discontinuity in the effective stress across the fault, such that the total stress is continuous

$$\boldsymbol{\sigma'}_- \cdot \boldsymbol{n} - bp_-\boldsymbol{n} = \boldsymbol{\sigma'}_+ \cdot \boldsymbol{n} - bp_+\boldsymbol{n}, \tag{4.16}$$

a requirement for momentum balance on the fault. This gives rise to the question of how to incorporate in the formulation the pressure jump across a fault. This is important because it determines the stability of the fault.

Fault stability can be assessed by evaluating the stability criterion on both sides of the fault separately. The side of the fault where the criterion is met first determines the fault stability. Equivalently, this can be achieved by defining a *fault pressure* that is a function of the pressures on the two sides, p_+ and p_-. Introducing the fault pressure allows us to uniquely define the *effective* normal traction on the fault, σ'_n, and determine the fault friction τ_f. Since the stability criterion, $\tau \leq \tau_f$, is first violated with the larger pressure, we define the fault pressure, p_f, as

$$p_f = \max(p_+, p_-). \tag{4.17}$$

Our definition of fault pressure is a natural result of our fault representation, rather than a conservative assumption. Note that estimating the fault pressure as the arithmetic average of the pressures on the two sides, as proposed in the case of tensile fractures (Segura and Carol, 2004, 2008a, 2008b), may incorrectly delay the onset of shear failure.

Fault tractions at faults. The most important output from the model is the calculation of stresses on faults. From the regional state of stress and the initial pressures, one can compute the initial stress on the faults. This is important to determine whether a fault is (or, rather, portions of a fault are) close to de-stabilization.

The potential for de-stabilization of a fault is measured by the evolution of the Coulomb stress, or Coulomb Force Function (CFF), defined as:

$$\text{CFF} = \sqrt{\tau^2_{\text{left-lat}} + \tau^2_{\text{updip}}} - \mu_f(-\sigma'_n), \tag{4.18}$$

where $\tau^2_{\text{left-lat}}$ and τ^2_{updip} are the left-lateral and up-dip components of shear stress on the fault,

$$\sigma_n' = \sigma_n + bp \tag{4.19}$$

is the effective normal stress on the fault (positive tensile), which is equal to the total normal stress plus the equivalent pore pressure (positive compressive), b is the Biot coefficient, and μ_f is the coefficient of friction on the fault.

As a result of pressure changes as well as poroelastic deformation, all components of stress vary along each fault. Variations in the CFF between any two times, e.g.,

$$\Delta\text{CFF}(t_1 \rightarrow t_2) = \text{CFF}(t_2) - \text{CFF}(t_1) \tag{4.20}$$

indicate if those changes are stabilizing (ΔCFF < 0) or de-stabilizing (ΔCFF > 0). Large positive changes in CFF over extended areas of a fault are indicative of substantial de-stabilization of a fault, and potential for fault slip and earthquake triggering. Changes in the order of 0.1 MPa (1 bar) are considered worrisome from the point of view of the potential for earthquake triggering (Freed, 2005). For some, but not all earthquakes, aftershocks have been documented to be triggered by increases in Coulomb stress of as little as 0.01 MPa (0.1 bar, Hardebeck et al., 1998).

4.3. Computational Modeling and Simulation Software

4.3.1. Numerical Discretization

The interactions between flow and geomechanics have been modeled computationally using various coupling schemes (Dean et al., 2006; Jeannin et al., 2007; Jha and Juanes, 2007; Mainguy and Longuemare, 2002; Minkoff et al., 2003; Settari and Mourits, 1998; Settari and Walters, 2001; Thomas et al., 2003; Tran et al., 2004, 2005; Kim et al., 2011a, 2011b, 2011c, 2013). In the fully implicit method, one solves the coupled discrete nonlinear system of equations simultaneously, typically using the Newton-Raphson scheme (Sukirman and Lewis, 1993; Pao and Lewis, 2002; Lewis et al., 2003; Li et al., 2005; Ferronato et al., 2010). The fully implicit method guarantees unconditional stability if the mathematical problem is well posed, but the simulation of flow and geomechanics for realistic fields becomes computationally very expensive (Settari and Mourits, 1998; Thomas et al., 2003; Jha and Juanes, 2007). Sequential approaches to modeling coupled flow and geomechanics are highly desirable because they offer the flexibility of using separate simulators for each subproblem (Felippa and Park, 1980; Samier and Gennaro, 2007; Minkoff et al., 2003; Rutqvist et al., 2002). The design and analysis of sequential methods with appropriate stability properties for poromechanics and thermomechanics has a long history (Zienkiewicz et al., 1988; Armero and Simo, 1992, 1993; Armero, 1999; Settari and Mourits, 1998; Mainguy and Longuemare, 2002; Jeannin et al., 2007).

Recently, a new sequential method for coupled flow and geomechanics, termed the "fixed-stress split," has been proposed and analyzed (Kim et al., 2011a, 2011b, 2013). Stability and convergence analyses have shown that the fixed-stress split inherits the dissipation properties of the continuum problem and is therefore unconditionally stable, both in the linear (poroelastic) and nonlinear (poroelastoplastic) regime. The analysis has shown that

the fixed-stress split enjoys excellent convergence properties, even in the quasi-incompressible limit. It has also been shown recently that the stability and convergence properties of the fixed-stress split for single-phase flow carry over to multiphase systems if a proper definition of pore pressure, the "equivalent pore pressure" (Coussy, 2004), is used (Kim et al., 2013).

In this section, we describe our computational model for coupled flow and geomechanics of faulted reservoirs. We couple a flow simulator with a mechanics simulator using the fixed-stress scheme (Kim et al., 2011b). We employ a rigorous formulation of nonlinear multiphase geomechanics (Coussy, 1995) based on the increment in mass of fluid phases, instead of the more common, but less accurate, scheme based on the change in porosity (Settari and Mourits, 1998; Minkoff et al., 2003; Thomas et al., 2003; Tran et al., 2004, 2005; Rutqvist et al., 2002). Our nonlinear formulation is required to properly model systems with high compressibility or strong capillarity (Coussy, 1995).

4.3.2. Simulation Software

We developed a coupled multiphase flow and geomechanical simulator by coupling the General Purpose Research Simulator (GPRS) (Cao, 2002; Pan and Cao, 2010) as the flow simulator, and PyLith (Aagaard et al., 2012, 2013) as the mechanics simulator. Below we describe the major features of this coupled simulator.

The flow simulator. GPRS is a general purpose, object-oriented, reservoir simulator for multiphase/multicomponent subsurface flows. It treats element connections through a general connection list, which allows for both structured and unstructured grids. GPRS is capable of handling complex production and injection scenarios in the field, such as wells perforated at multiple depths and flowing under variable rate and pressure controls. The original simulator (Cao, 2002; Pan and Cao, 2010) does not account for coupling with the mechanical deformation, and it models the mechanical behavior of the system through a user-provided rock compressibility (Aziz and Settari, 1979). We modified and extended the original code to implement the coupling with the mechanics simulator. In particular, we implemented the functionality to compute the modified accumulation term in the fluid phase mass balance equations. We also modified the setup of the linear system to implement the flow step of the fixed-stress sequential solution scheme (Kim et al., 2011a).

The geomechanics simulator. PyLith is a finite element code for the simulation of static and dynamic large-scale deformation problems (Aagaard et al., 2012, 2013). Much of its development has been motivated by the modeling of earthquake physics; however, its applicability extends to problems at any other scale, such as the reservoir scale or the laboratory scale. Some of the advantages of PyLith are (1) it is an open-source code and can be modified for specific purposes; (2) it is written using C++ and Python languages and is extendable; (3) it is suitable for parallel computing; (4) it allows localized deformation along discrete features, such as faults; and (5) it is well integrated with meshing codes, such as LaGriT for tetrahedral meshes (LaGriT, 2013) and Trelis for both tetrahedral and hexahedral meshes (CUBIT, 2013). PyLith uses an implicit formulation to solve quasi-static problems and an explicit formulation to solve dynamic rupture problems. Originally, PyLith

is not coupled to any fluid flow model. We modified the code of PyLith version 1.8.0 and coupled it with the flow simulator, GPRS. In particular, we implemented a C++ class, iGPRS, to allow communication between the flow and the mechanics simulators. iGPRS provides the functionality required for exchanging information (pressures, saturations, and volumetric total stress) between the two simulators.

PyLith supports distributed memory parallelization (Message Passing Interface or MPI) whereas GPRS's parallelization is based on the shared memory architecture (Multiprocessing or OpenMP). We integrated the two such that we can run the coupled simulator on a cluster with multiple compute nodes (distributed memory) where individual nodes have multiple cores or processors (shared memory).

Grid. We use a single grid for both GPRS and PyLith. The grid is generated using the Trelis (CUBIT, 2013) mesh generation software. We define geologic surfaces, material regions, faults, and pinch-outs during the geometry creation stage. Then we mesh the domain with hexahedral elements using a fine mesh in the reservoir domain and an increasingly coarse mesh in the overburden, underburden, and sideburden regions. We export the grid in a finite element format such as the Exodus-II format (CUBIT, 2013) for PyLith. We process the grid file using a MATLAB script to generate the equivalent finite volume grid in the domain with element centroid coordinates, element bulk volumes, and face transmissibilities in the Corner Point Geometry format (Schlumberger, 2016). Any grid elements lying outside the flow region of interest (e.g., in overburden and underburden) can be deactivated for the solution of the flow problem. GPRS uses the finite volume grid for simulating flow in the region of interest. The two simulators exchange pressures, saturations, and volumetric stress information inside this region.

Implementation of faults. To support relative motion across fault surfaces, PyLith modifies the grid topology to create zero-thickness fault elements and adds additional degrees of freedom to hold the Lagrange multipliers and fault slip vectors at the Lagrange nodes (Aagaard et al., 2012, 2013) (Figure 4.2). PyLith solves the contact problem iteratively in two steps. In the first step, the elasticity problem is solved over the entire domain to update the displacements and the fault tractions (Lagrange multipliers) corresponding to the current estimate of the slip. The Lagrange multipliers are compared with the friction stress on the fault and are adjusted to be compatible with the fault constitutive model. In the second step, the fault slip is updated corresponding to the adjustment in the Lagrange multipliers while assuming that the deformation due to slip is localized to the elements adjacent to the fault, that is, that displacements at non-fault nodes do not change from their values at the current Newton iteration. If the fault slips over the entire domain, such that the assumption of deformation being limited to the adjacent elements is not met, the convergence of the iterative scheme is poor. Also, if the fault friction coefficient changes significantly with slip (e.g., in rate- and state-dependent models), it leads to large changes in τ_f at every iteration and convergence may degrade. To improve convergence, a line-search routine is used as part of the iterative scheme to find the optimum perturbation in the Lagrange multipliers that minimizes the combined mismatch between the fault friction and the fault shear traction at all the fault nodes

(Aagaard et al., 2013). We modified PyLith's original line-search routine such that the inequality constraint, $\tau \leq \tau_f$, is always honored.

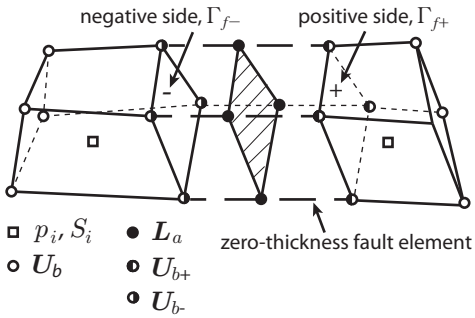

Figure 4.2: Exploded view of our computational representation of a fault, illustrating different node types, locations of different variables, and the zero-thickness fault element. Fluid pressures p_i and saturations S_i are located at the element centers as they are discretized using the finite volume method. Displacements and Lagrange multipliers at the fault are discretized using the nodal-based finite element method. There are two types of nodes in the domain: the displacement nodes and the Lagrange nodes. The displacement nodes carry the displacements $\mathbf{U}_{br}$ at the regular nodes, the displacements $\mathbf{U}_{b+}$ on the positive side of the fault, and the displacements $\mathbf{U}_{b-}$ on the negative side of the fault. The Lagrange nodes carry two types of fault variables: the Lagrange multipliers $\mathbf{L}_b$ (related to fault tractions), and the fault slip $\mathbf{D}_b$. The displacement nodes on the positive and negative sides, and the Lagrange nodes are collocated in the initial grid.

4.4. Computational Grid

Our modeling strategy for Castor is substantially different in many respects from previous modeling efforts. The simulation domain is much larger than previous simulation models (in particular, a previous Eclipse simulation model, see Figure 4.3). This allows us to: (1) incorporate all the main faults in the vicinity of the Castor platform, and (2) directly model a large and deep aquifer, and (3) incorporate the tectonic stresses in the region such that those boundary conditions are unaffected by reservoir operations.

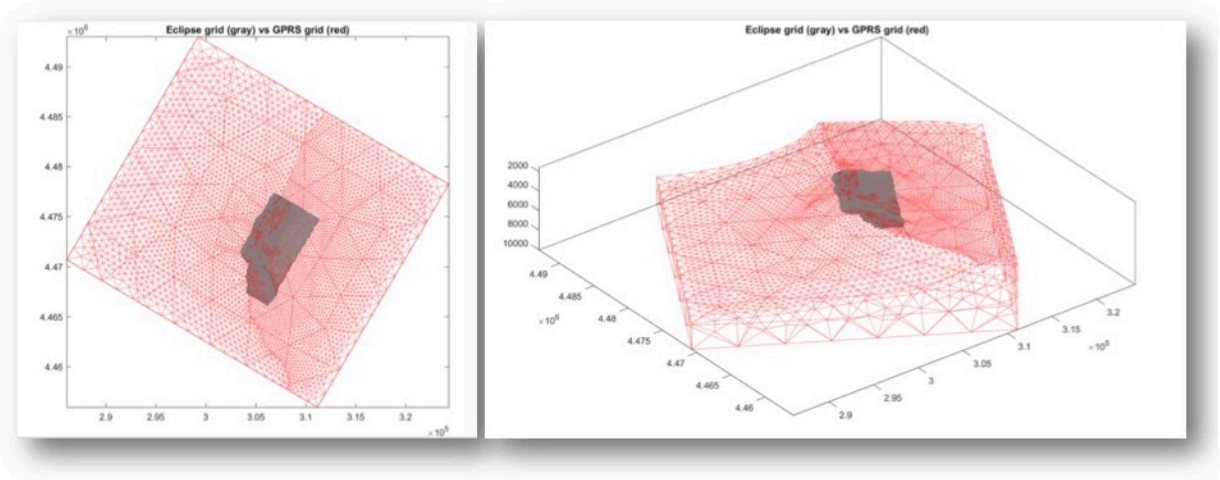

Figure 4.3: Simulation domain for coupled flow-geomechanics simulation (red color) vs Eclipse simulation (gray color). Left panel for top view, right panel for lateral view.

Our simulation model was built using an unstructured grid of tetrahedral cells, necessary to adapt to the stratigraphic and fault representations defined in the geologic structural model (Chapter 2 of this report).

The computational mesh had to be fine enough to capture the key flow and geomechanical responses associated to both Amposta and Castor operations, but it also had to balance the number of resulting grid cells in order to avoid excessive computational burden. For this particular study the meshing process was not trivial due to the need to embed some of the complex geometries for the faults that exist in the vicinity of the Castor platform. As a result, the simulation model had a relatively low resolution around the original oil-water contact in Amposta—in contrast, it extends to depths well below the oil-water contact to directly model the aquifer.

The overall size of the computational domain was approximately 25 × 30 × 10 km. The total number of grid cells was 217,711. The reservoir zone included 86,638 cells, with a maximum depth of more than 9000m. A snapshot with the model depth along with the location of the Amposta wells is shown in Figure 4.4.

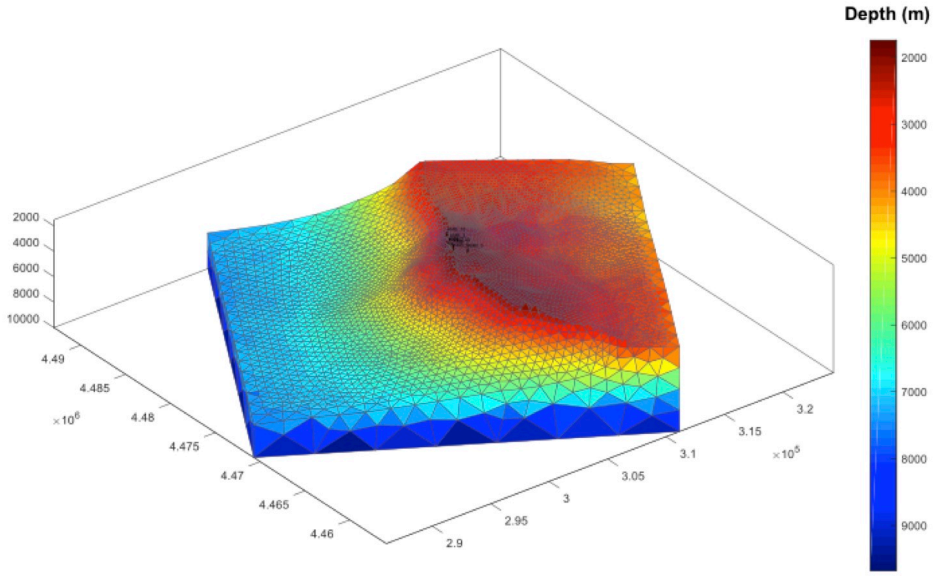

Figure 4.4: Depth of simulation domain of the coupled flow-geomechanics model. The original Amposta wells at the top central part of the reservoir are shown.

4.5. Flow Modeling and History Matching

While the description and resolution of our model was very different from previous studies, some elements required for the modeling of multiphase fluid flow in the reservoir were derived from the existing Eclipse simulation deck (Geostock Iberia, 2011). For instance, PVT tables, fluid densities, relative permeability curves and connate water saturations were imported and adapted from existing Eclipse models. We also extracted from the Eclipse model the well schedules for the simulation of the Amposta phase. On the

other hand, other model parameters (e.g., well completion cells, well schedules during the injection phase) were derived from existing data and discussions with Enagas. Rock properties (permeabilities, porosities and compressibilities) were re-defined in our model.

Table 4.1 provides all the well completions that were implemented in our simulation model. Furthermore, for visualization purposes, Figure 4.5 shows a Y-Z cross-section of the simulation model with all the completion cells for the old Amposta wells.

Table 4.1: Coordinates (X,Y,Z) and Measured Depth (MD) for all well completion intervals implemented in the simulation model. All units in meters.

Well Name	X	Y	Z	MD
AMB_10	306121.2	4475185	-1773.77	2016.5824
AMB_10	306123.6	4475190	-1782.54	2026.5824
AMB_1	305438.6	4473684	-1797.78	1797.7752
AMB_1	305438.6	4473684	-1822.78	1822.7752
AMB_2A	305604.4	4473930	-1812.49	1854.8828
AMB_2A	305616.3	4473945	-1890.28	1934.8828
AMB_3	305816.5	4474467	-1805.05	2063.1912
AMB_3	305849.2	4474540	-1935	2215.5912
AMB_5	305918	4472499	-1884.71	2400.6047
AMB_5	305926.1	4472449	-1978.49	2507.0349
AMB_6	305197.4	4473299	-1765.49	1840.6873
AMB_6	305189.1	4473292	-1801.92	1878.6873
AMB_7	305404	4474138	-1742.63	1857.756
AMB_7	305403.2	4474140	-1749.25	1864.756
C1	305417.1	4474306	-1741.43	1843.2576
C1	305412.9	4474312	-1751.26	1855.5576
C2	305180.2	4473683	-1723.05	1879.7017
C2	305172.1	4473675	-1744.66	1904.3016
C3	305084.5	4473253	-1749.73	2126.2849
C3	305084.1	4473239	-1771.14	2151.8848
C4	306030.1	4475089	-1773.78	2257.7105
C4	306046.4	4475132	-1814.54	2319.2105
C5	305291	4474031	-1748.25	1824.892
C5	305288	4474030	-1761.17	1838.192
C6	305649.4	4474410	-1815.35	1905.7712
C6	305652.2	4474421	-1863	1954.8712
C7	305869.6	4474627	-1837.94	2028.0288
C7	305878.7	4474644	-1869.49	2065.0288
C8	304946	4472919	-1774.72	2425.1792
C8	304940.6	4472908	-1782.8	2439.7793
POB	305394.2	4473793	-1766.32	1860.804
POB	305370	4473710	-1999.6	2110

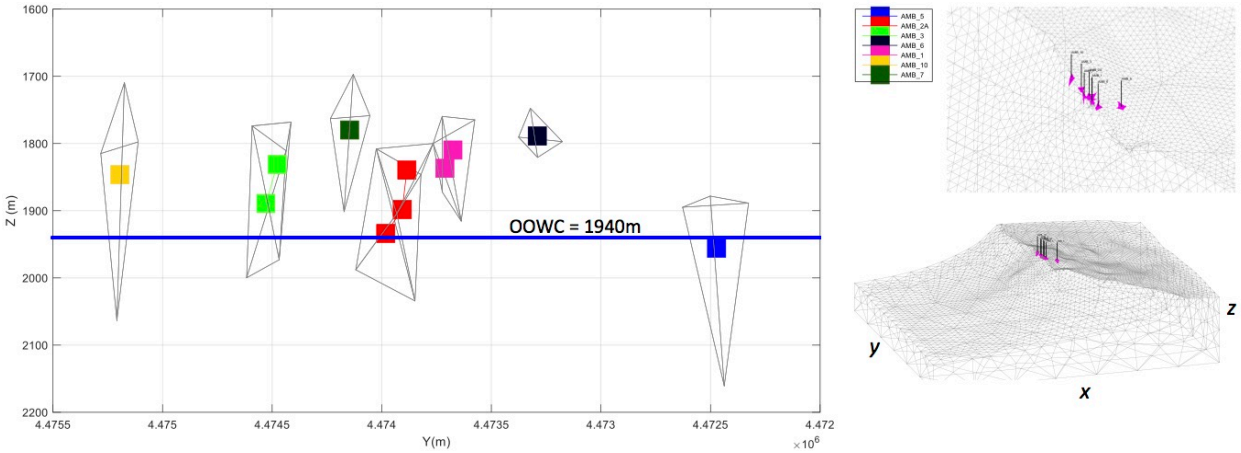

Figure 4.5: Cross-section (Y-Z) of coupled flow-geomechanics model showing completion cells for Amposta wells. Location of the original oil-water contact (OOWC) is also shown at 1940m.

We conducted a sensitivity analysis of the dynamic flow model to key model parameters to better understand the model behavior and to constraint the model description. These parameters included rock compressibility, location of the Original-Oil-Water-Contact (OOWC), fluid densities, water injectors in the aquifer (location and number), general rock permeability and porosity multipliers, among others.

Within this sensitivity analysis the OOWC (1940m) was re-adjusted in our model to minimize the amount of water production (which resulted mainly from having parts of the completion cells for some producers being located below the OOWC). The adjusted OOWC (2009m) was shown to have marginal impact on the reservoir pressure response while significantly reducing the watercut (which is more aligned with the official small water cuts reported for this field during its production phase in the 70s-80s). On the other hand, the possibility of having artificial water injectors in the aquifer (to increase the aquifer support) was also analyzed and finally deemed unnecessary (once rock permeabilities and porosities were readjusted). Small changes in fluid densities were also considered to see their impact on model response. In general rock permeabilities and porosities in this model were regarded as very uncertain due to the lack of reliable prior information; our sensitivity analysis allowed us to constraint their values before a more detailed history matching.

Thus we implemented a formal history matching approach to better reproduce the observed field data. While both production (Amposta) and injection (Castor) phases were considered for the history matching quality, more emphasis was put into representing the observed pressure response during the Castor injection phase. A total of 10 layers was defined in the model (5 layers above OOWC and 5 layers below) with their corresponding horizontal and vertical permeability and porosity multipliers. History matching was achieved by using a sequential Monte Carlo process, and the resulting model is named Model 1 hereafter. As discussed Bayesian solutions were ruled out due to lack of reliable prior information on the model parameters. Other history matching approaches (e.g.,

MCMC) were disregarded due to their excessive computational requirements for this type of coupled flow-geomechanics models.

The improvement in the pressure match for the Castor phase resulting from the history matching exercise is clearly shown in Figure 4.6. This adjusted pressure response, together with the observed field pressure data, is shown in Figure 4.7. Clearly there is a very good agreement between both. Simulation results for the simulation of the Amposta phase are provided in Figure 4.8 (for pressure and cumulative water production). Some mismatch for both pressure and, more especially, water production is observed during this phase. Most of the excessive water production originates in one single well (AMB6, as seen in Figure 4.9). It is worth noticing that the observed mismatch in water production is relatively small in comparison to some previous modeling efforts and even comparing to our initial model attempt for Castor (baseline model).

Having an accurate representation of the pressure response in the Castor phase was given the highest priority for our history matching study. Given the model complexity and, to a certain extent, the uncertainties associated to some of the data reported back in the 70's and 80's the mismatch during this production phase was regarded as acceptable. Oil production and gas injection volumes were honored in the model during Amposta and Castor phases respectively. Alternative models that better represent the Amposta production phase were also derived in this study (they are not presented here), but in general they show a tendency to deteriorate the pressure response during the Castor injection phase and, therefore, they were not pursued.

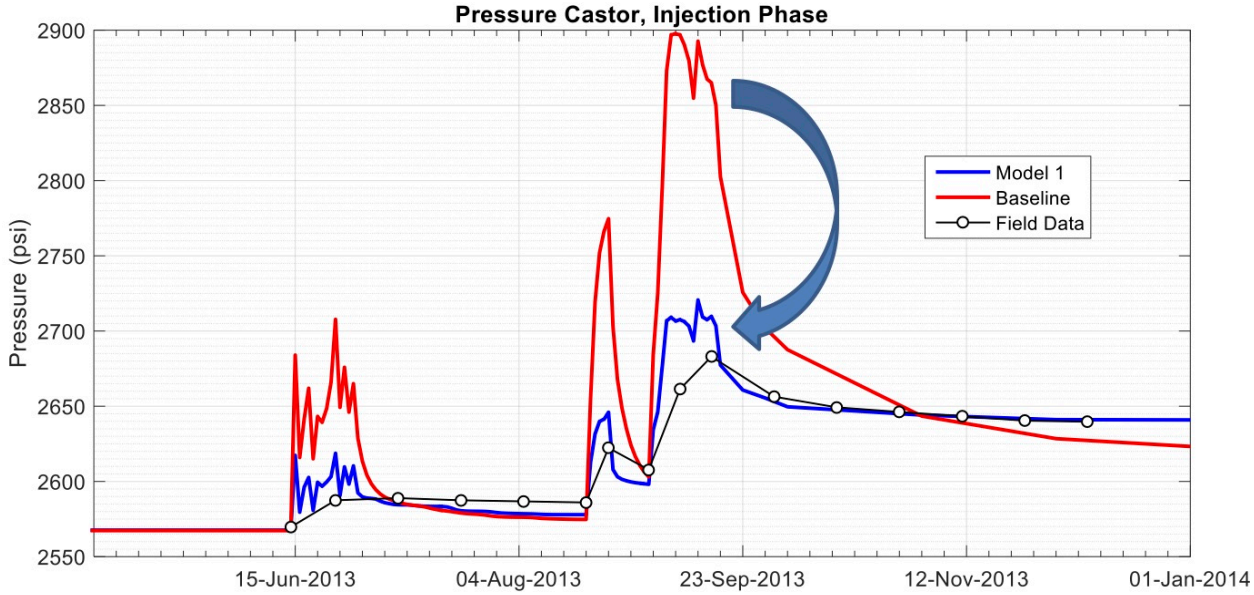

Figure 4.6: Simulated pressure response in Castor before (Baseline) and after (Model 1) history matching using a sequential Monte Carlo approach. The substantial improvement is highlighted by the blue shaded arrow.

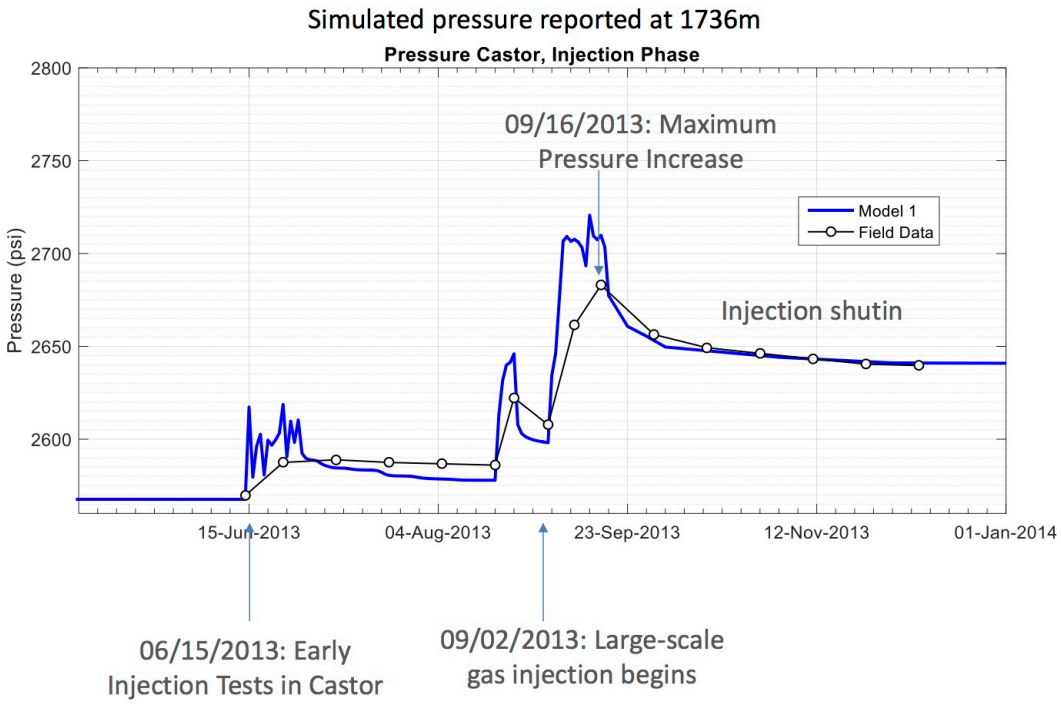

Figure 4.7: Simulated pressure response in Castor after History Matching (Model 1) together with the observed field pressure data.

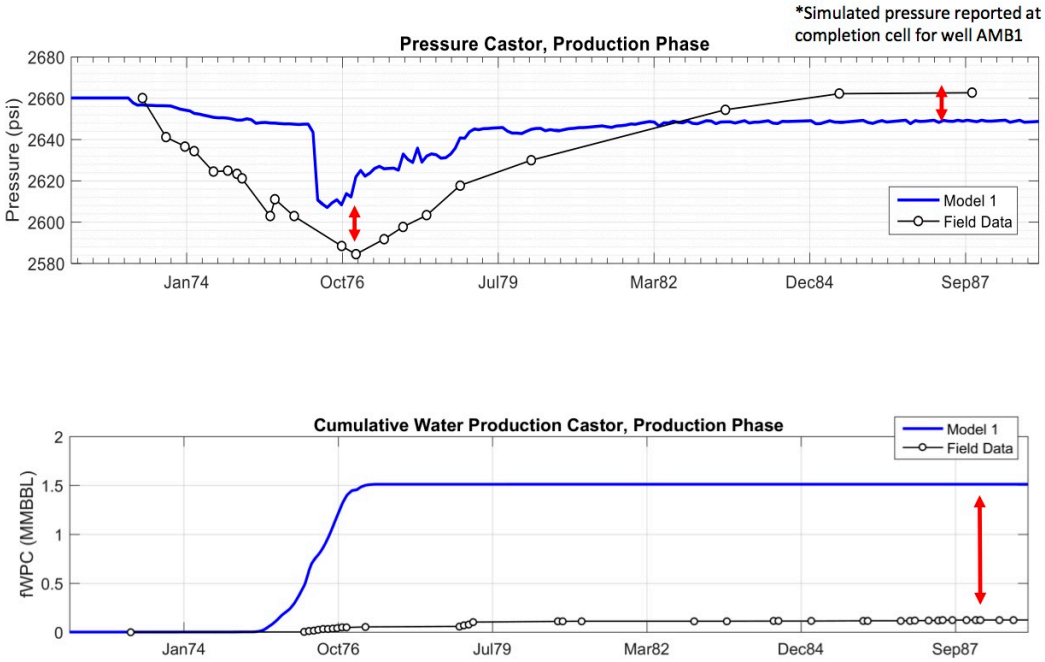

Figure 4.8: Simulated pressure response during Amposta phase after History Matching (Model 1) together with the observed field data. The small red arrows indicate the resulting mismatch.

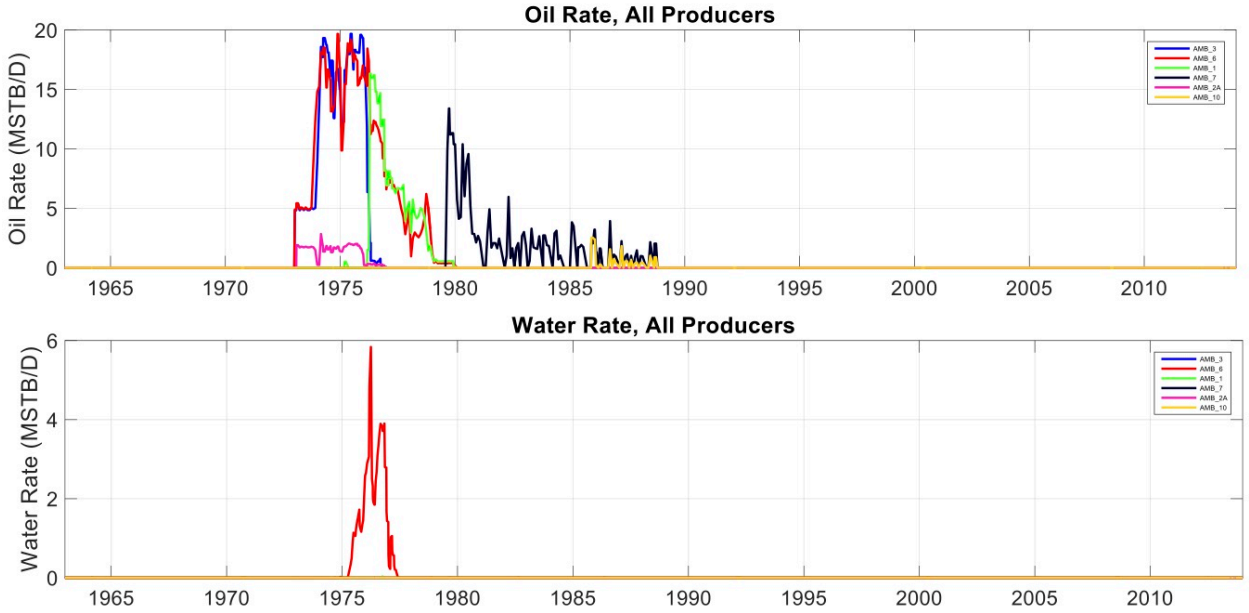

Figure 4.9: Simulated individual well production rates (oil and water) for the Amposta wells. Notice that most water production comes from one single well in the model (AMB6).

The simulated pressure field at September 16, 2013 across the entire simulation domain is shown in Figure 4.10 for Model 1. The resulting rock permeabilities (PERM-X, PERM-Y and PERM-Z) and rock porosities for this same model are provided in Figure 4.11 (only reservoir cells above OOWC are displayed)

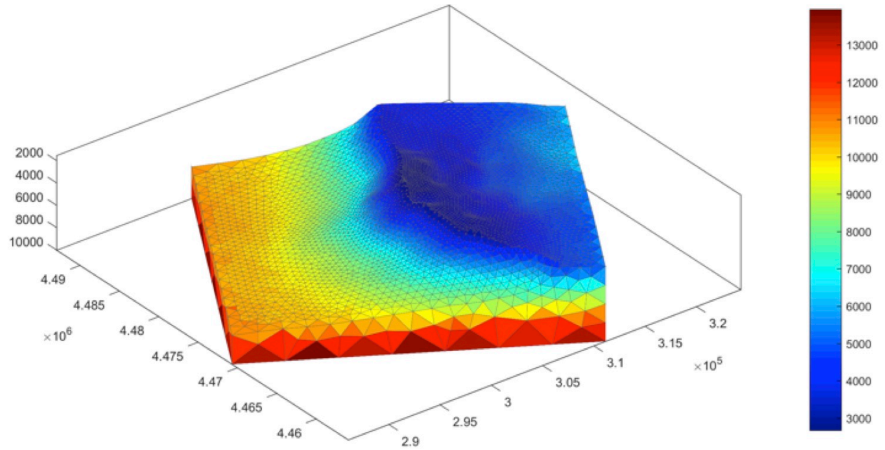

Figure 4.10: Simulated pressure response across entire domain (Model 1) in Castor at September 16, 2013. Units are given in psi.

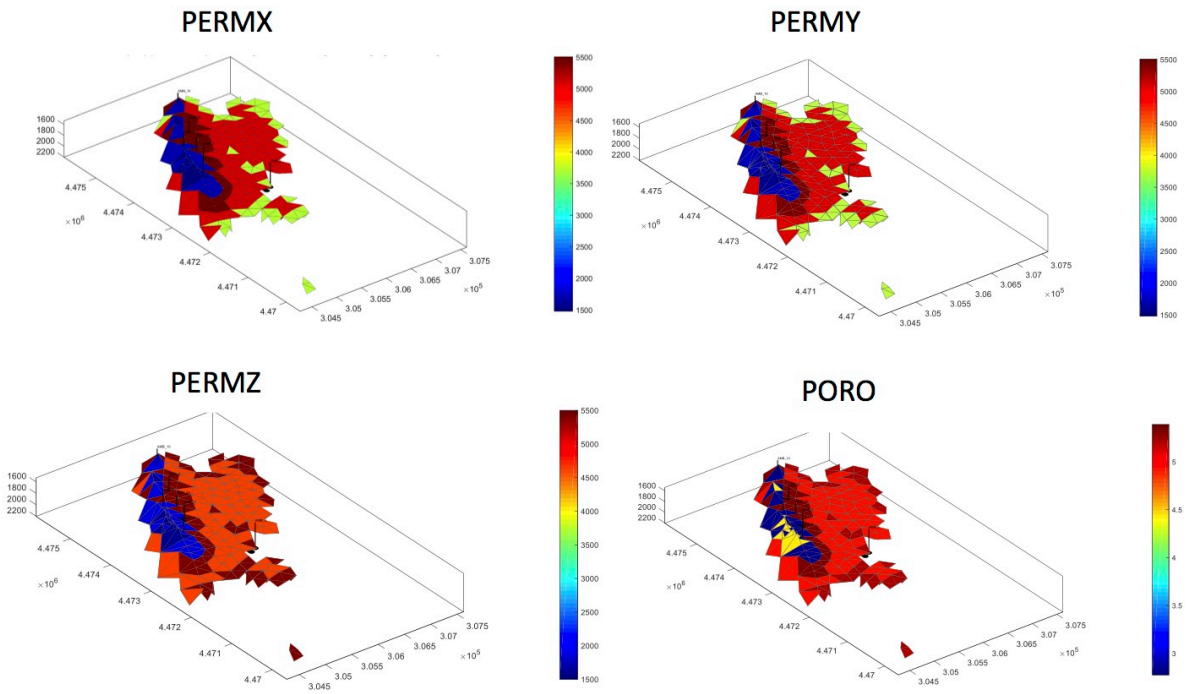

Figure 4.11: Rock permeability (in X, Y and Z direction; units in mD) and porosity (%) after history matching. Only reservoir cells above the OOWC are shown.

Our simulated pressure field for the entire simulation domain was then used to guide the geomechanical simulation in a one-way coupled formulation (see next section for geomechanical results).

An important practical consideration in our study was to evaluate the potential behavior in Castor for different injection scenarios. For example, we used the history-matched model discussed above (Model 1) to quantify the expected changes in pressure response for several reduced gas injection rates. As expected, our simulations clearly show a reduction in the pressure increase during the injection phase as the gas injection rate was reduced (Figure 4.12).

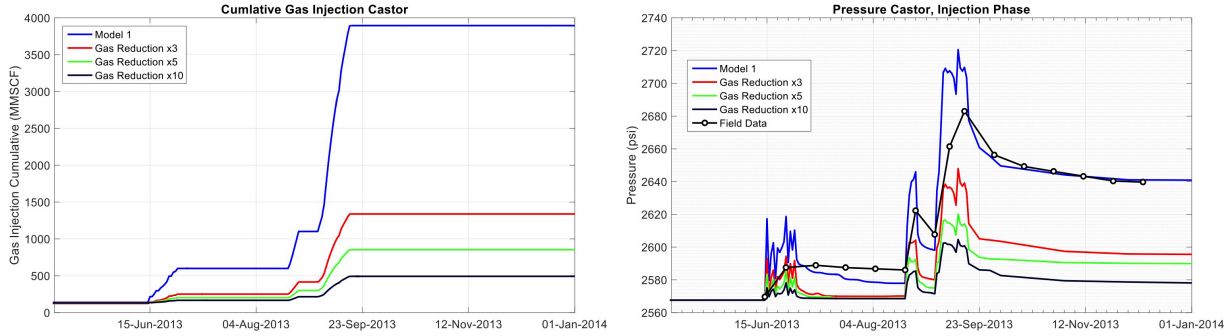

Figure 4.12: Simulated pressure response in Castor for reduced injection scenarios. Left: cumulative gas injection. Right: estimated pressure response. A total of 3 such scenarios is considered (reducing gas injection rates by factors of ~ 3, 5 and 10).

We have also evaluated other injection scenarios of interest, as well as the corresponding impact of pressure variations on the geomechanical behavior of the system and faults stability. For instance, we simulated the following scenario that was proposed in an Escal UGS 2012 report ("Proyecto Castor: Informe Geológico de Final de Campaña de Perforación"; the scenario is referenced there as "Escenario Case Base"). This scenario is illustrated here in Figure 4.13.

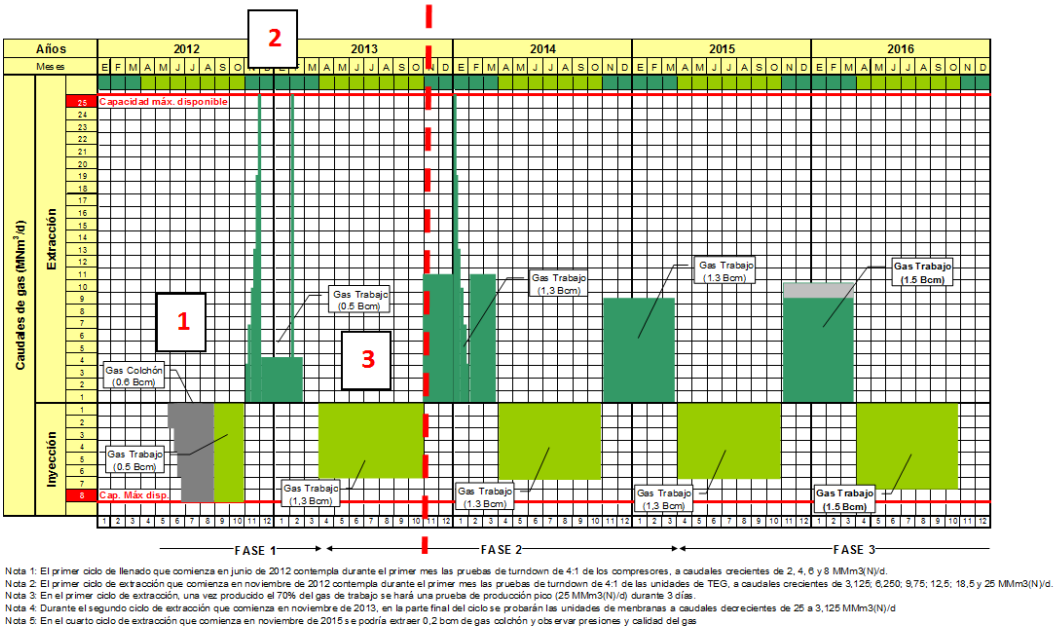

Figure 4.13: Scenario described in Escal UGS 2012 report "Proyecto Castor: Informe Geológico de Final de Campaña de Perforación"; the scenario is referenced there as "Escenario Case Base".

Our goal in this scenario was to approximately simulate stages 1, 2 and 3, which compose what Escal UGS called "FASE 1" (see Figure 5.12). These stages are briefly described now:

i. Total volume of gas injected in Castor before shutdown on September 17, 2013 was ~103 MMm^3. This includes all the volume of gas injected in 2012 and 2013, and it represents only ~17% of the total volume of gas that was originally designed for injection. In this new scenario we simulate now the injection of the total volume that was originally designed (i.e., ~600 MM3). This is called Stage 1 in this scenario.
ii. After that we simulate the production of all the injected gas. This is called Stage 2.
iii. Finally we simulate (Stage 3) a new injection cycle with a total gas injection volume of 1300 MMm^3 (notice this is 10 times larger than the volume injected in Castor before shutdown). For this stage we simulate a lower injection rate than Castor (i.e., ~1/5 of the maximum rate imposed during the Castor phase).

Our simulated pressure response for this scenario is shown in Figure 4.14, which clearly yields the expected behavior of an initial pressure increase due to gas injection (Stage 1), followed by a pressure decrease due to the production of that gas (Stage 2) and a final new

pressure increase associated to the latest gas injection phase (Stage 3). The geomechanical results for this same scenario are briefly discussed later in this report within the overall geomechanical discussion.

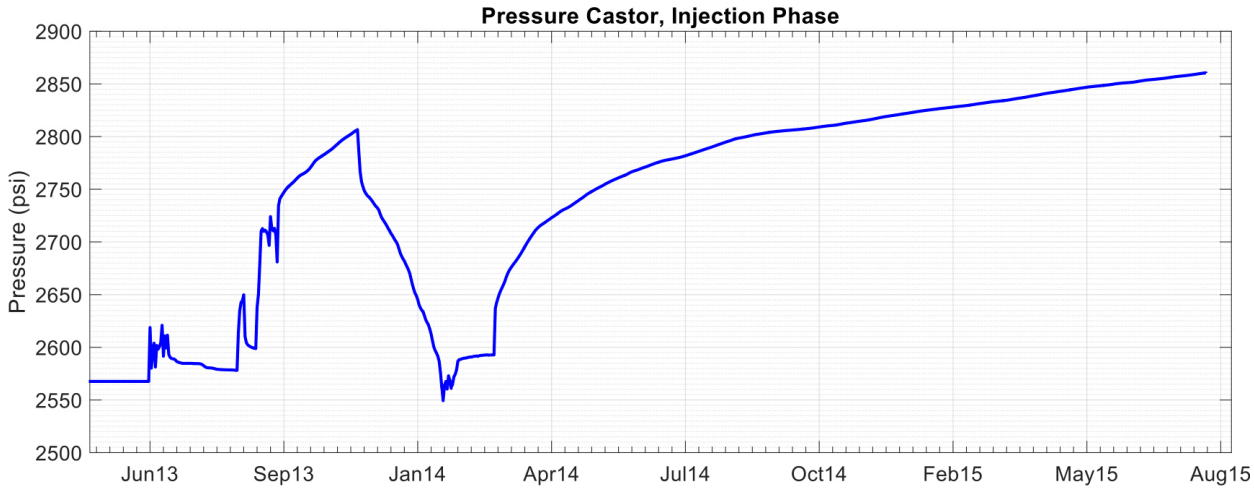

Figure 4.14: Simulated pressure response in Castor for "Escenario Case Base" described in Escal UGS 2012 report "Proyecto Castor: Informe Geológico de Final de Campaña de Perforación"; this scenario involves a hypothetical sequence of injection, production and new injection phases.

4.6. Coupled Flow-Geomechanics Analysis: Fault Stresses

Our coupled flow and geomechanics analysis leads to a *dynamic* quantitative simulation of the impact of subsurface operations (oil production and gas injection) on the stresses on the fault structures present in the model.

Geomechanical initialization and boundary conditions. The model is initialized in terms of stresses and pressures, such that it is in mechanical equilibrium with gravity and tectonic stresses. The tectonic stress regime is dominated by normal-faulting mechanism on NW oriented planes (Perea et al., 2012). Along that direction, the ratio of horizontal to vertical stress is < 1. The boundaries of the model domain were originally aligned with the principal directions of the tectonic stress, in anticipation that they would lead to an easier imposition of boundary conditions for the geomechanics problem. We impose the stress boundary conditions on a grid that is rotated 59.4 degrees counterclockwise to align the model the prevalent tectonic stresses in the region (and the model boundaries) with the coordinate system. We choose the horizontal stresses as follows: the maximum horizontal stress equal to the vertical stress and points to the NE; the minimum horizontal stress equal to 0.7 × vertical stress and points to the NW (Figure 4.15).

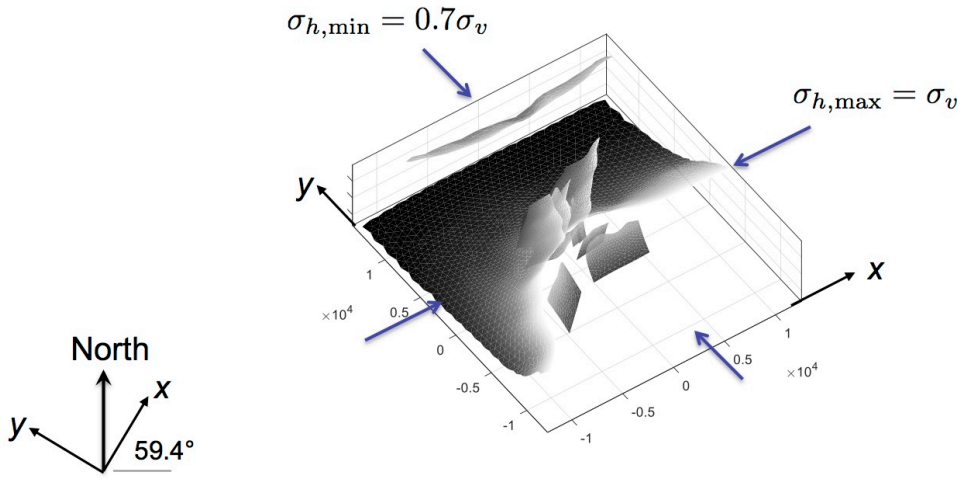

Figure 4.15: Schematic of the model with rotated grid for imposition of tectonic boundary stresses. The x-direction points NE and coincides with the maximum horizontal stress (= vertical stress); the y-direction points NW and coincides with the minimum horizontal stress (=0.7 × vertical stress).

A naïve way to impose the mechanical boundary conditions is to impose rollers on three faces (x-, y- and z-), and normal stresses on the other three (with geostatic stresses on the x+ and y+ faces, and normal stress from the water column on the z+ topography). We have detected, however, that imposing geostatic stresses leads to bending moment that induces thrust stresses at the top portion of the domain.

Thus, we impose the mechanics conditions as follows:

(1) We impose a pre-stress $\boldsymbol{\sigma}_0$ with the desired target tectonic stresses,

$$\boldsymbol{\sigma}_0 = \begin{bmatrix} \sigma_{xx}^0 & 0 & 0 \\ 0 & \sigma_{yy}^0 & 0 \\ 0 & 0 & \sigma_{zz}^0 \end{bmatrix},$$

where

$$\sigma_{zz}^0 = \int_{z_+}^{z} \rho_b g \, dz, \quad \sigma_{yy}^0 = \sigma_{zz}^0, \quad \sigma_{xx}^0 = 0.66\, \sigma_{zz}^0.$$

(2) We prescribe the displacements on the lateral faces, as rollers with imposed normal displacements ($u_{x-} = u_{x+} = 0$, and $u_{y-} = u_{y+} = 0$), which result in the pre-stressed state with near-zero strains.

Poromechanical parameters. Based on previous geomechanical analysis (e.g., Nauroy et al., 2011) and consistency with values of Vp and Vs from the geologic structural model built as part of this study, we took poromechanical parameters that are representative of the carbonate reservoir:

- Matrix bulk modulus (static): K = 14 GPa
- Poisson ratio (drained): ν = 0.26
- Biot coefficient: b = 1.0

From these parameters and from the rock densities, we compute the inputs for PyLith (V_p and V_s):

$$G = \frac{3K(1-2\nu)}{2(1+\nu)}, \quad \lambda = 3K\frac{\nu}{1+\nu},$$

and

$$V_p = \sqrt{\frac{\lambda + 2G}{\rho}}, \quad V_s = \sqrt{\frac{G}{\rho}}$$

4.6.1. Analysis of the Injection Period

Our model provides the means to compare the impact of reservoir operations on all faults included in the model (Figure 4.16).

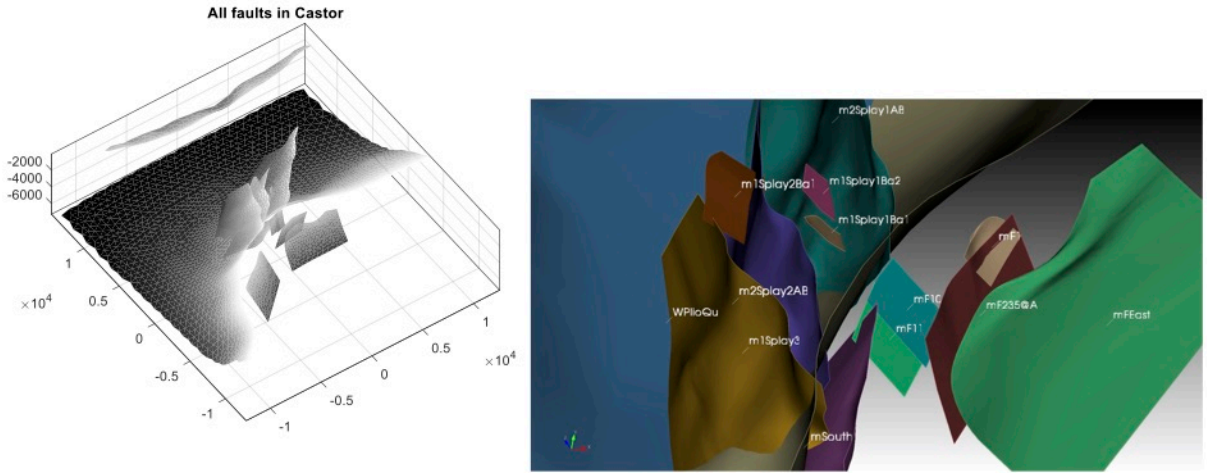

Figure 4.16: Two views of all the faults included in the coupled flow-geomechanics model. Left: view of the entire domain from the footwall (reservoir) side. Right: detailed view with labels for each fault.

Here we focus exclusively on the injection period and, in particular, on the period September 1 – September 16, 2013, given that the latter date corresponds to the time of highest reservoir pressure (see Figure 4.7).

Amposta fault. Given that the Amposta fault is the largest structure, and is known to be subject to recent (Quaternary) activity, it is particularly important to determine the impact of reservoir operations on this fault. We illustrate both the initial stresses computed by the model, and the changes in stress, for all three stress components (left-lateral, updip, and effective normal), along with the corresponding impact on the Coulomb stress.

The change in the left-lateral component is positive towards the East and negative towards the West, as a result of reservoir inflation from gas injection (Fig. 4.17). The change in the

up-dip component is negative (i.e., in the sense of favoring normal faulting) towards the overburden, and positive (i.e., in the sense of favoring thrust faulting) towards the underburden, also as a result of reservoir inflation (Fig. 4.18). The change in effective normal is mostly positive, indicating unclamping of the fault as a result of pressure increase on the reservoir side of the fault (Fig. 4.19). The overall effect of these stress changes is an increase in the Coulomb stress on the Amposta fault in the proximity of the injection wells, indicative of a de-stabilization of the fault as a result of injection. In our model, the Coulomb stress changes reaches a maximum of about 0.5 MPa – a significant stress change (Fig. 4.20).

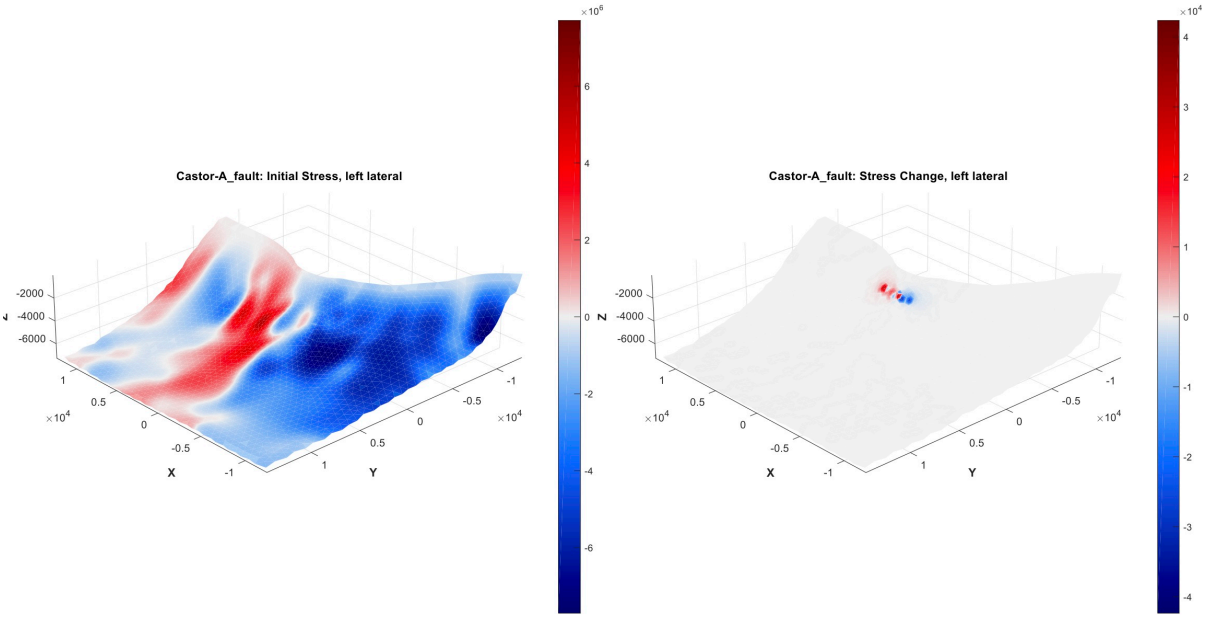

Figure 4.17: Illustration of initial stresses and stress changes on the Amposta fault during the period September 1–September 16, 2013, as a result of gas injection. Left-lateral stress.

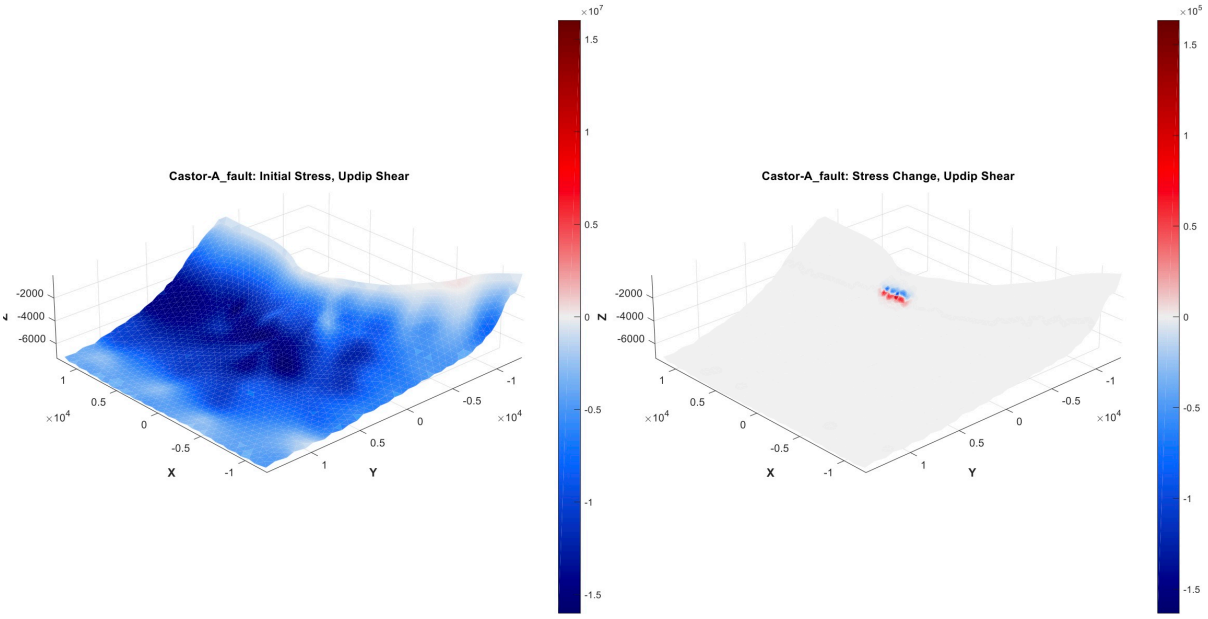

Figure 4.18: Illustration of initial stresses and stress changes on the Amposta fault during the period September 1–September 16, 2013, as a result of gas injection. Updip stress.

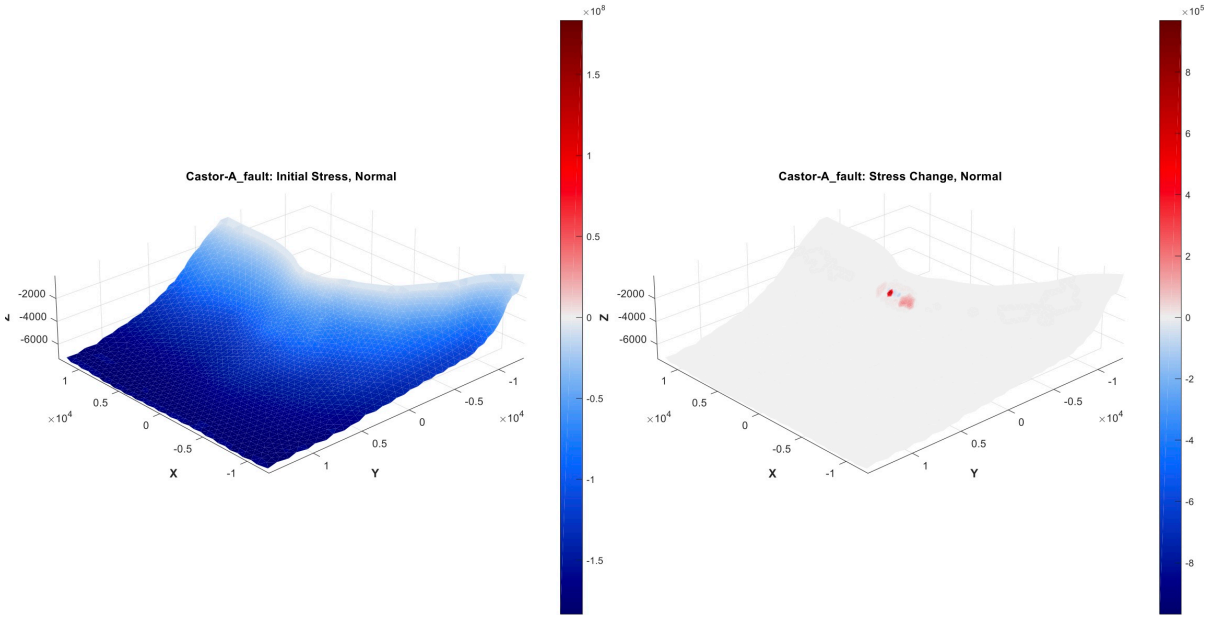

Figure 4.19: Illustration of initial stresses and stress changes on the Amposta fault during the period September 1–September 16, 2013, as a result of gas injection. Effective normal stress.

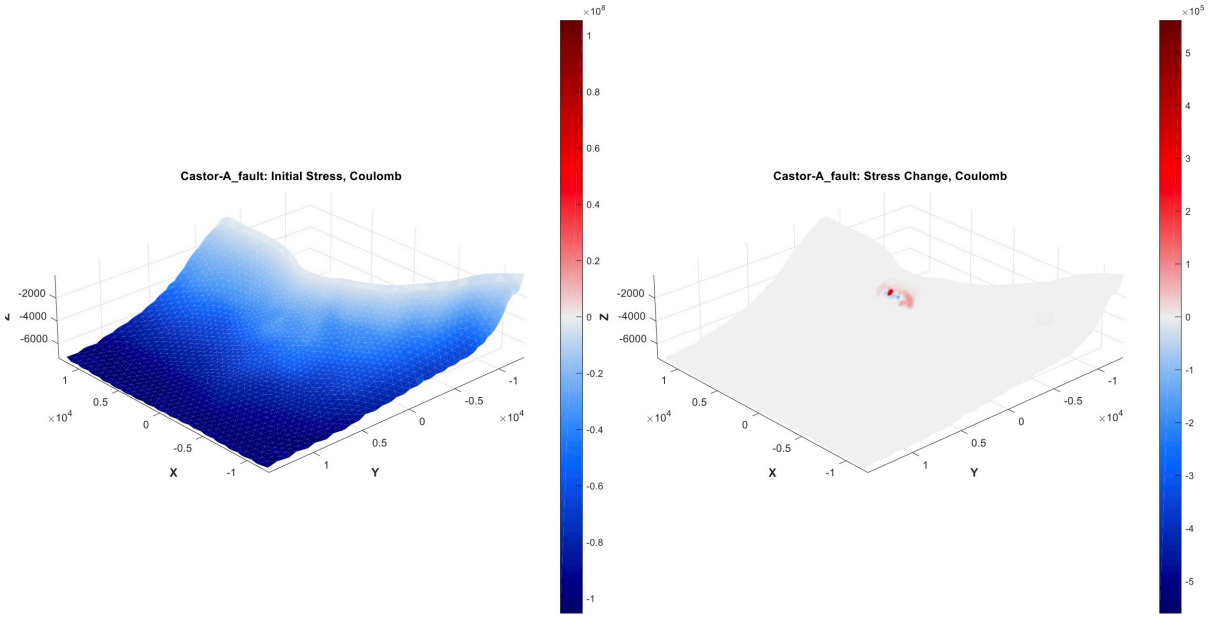

Figure 4.20: Illustration of initial stresses and stress changes on the Amposta fault during the period September 1–September 16, 2013, as a result of gas injection. Coulomb stress.

Reservoir faults. The structures that are predicted to be most de-stabilized by injection are several of the model faults within the reservoir and in proximity of the injection wells. As an illustration, we plot here the stress changes in one of these structures: fault F11 (Figure 4.21). Changes in left-lateral stress (Fig. 4.21a) are de-stabilizing to the East and

stabilizing to the West of injection as a result of reservoir inflation but these stress changes (as is the case with changes in the updip component, Fig. 4.21b) are relatively small, in the order of tens of kPa. The main driver for stress changes on reservoir faults is the reduction in compressive effective normal stress as a result of pore-pressure increase from gas injection in the reservoir (Fig. 4.21c). These changes are on the order of hundreds of kPa, and largely determine the uniformly de-stabilizing changes in Coulomb stress, with values of up to 0.4 MPa (Fig. 4.21d).

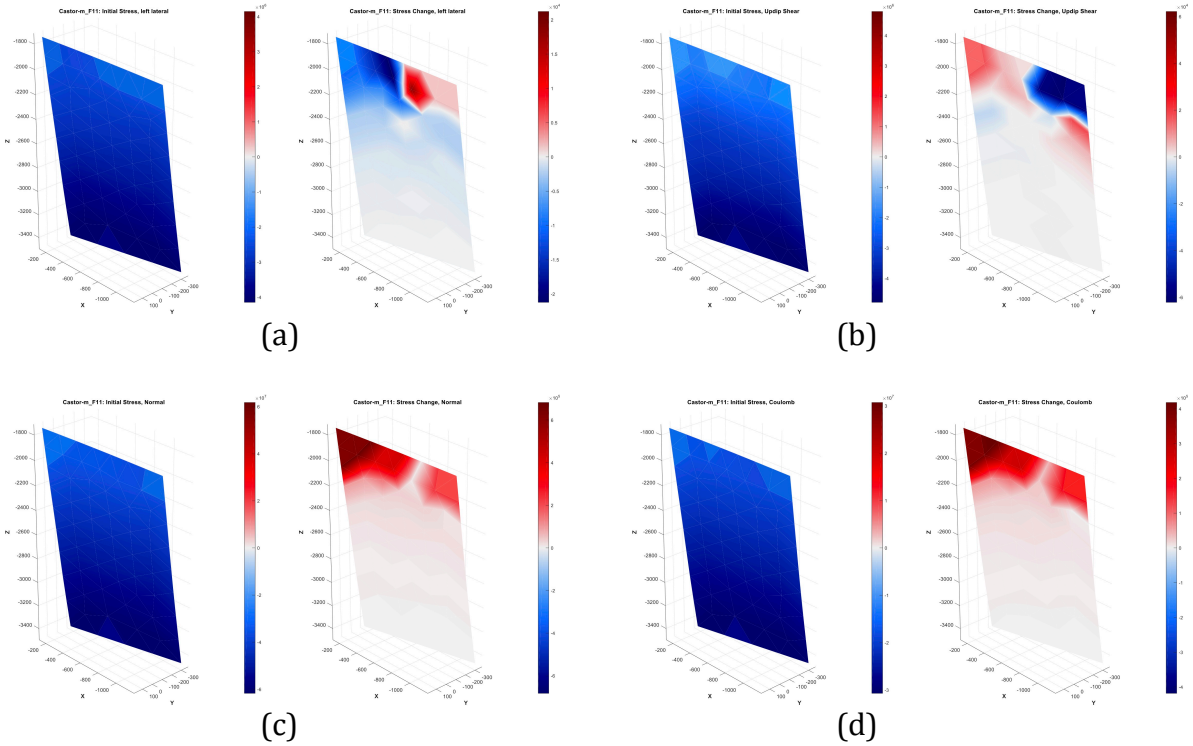

Figure 4.21: Illustration of initial stresses and stress changes on the reservoir fault F11 during the period September 1–September 16, 2013, as a result of gas injection. (a) Left-lateral stress; (b) Updip stress; (c) Effective normal stress; and (d) Coulomb stress.

Splay faults. The Amposta fault system includes, in addition to the main fault trace, other splay faults that connect to the main fault and extend to the hanging wall side. Geometrically, these faults are a natural extension of the West segment of the Amposta fault (Fig. 2.9), and are likely accommodating much of the recent tectonic strain in the fault system. From a modeling point of view, these structures are hydraulically disconnected from the reservoir due to the caprock offset across the Amposta fault. However, this does not mean that they are free from experiencing stress changes. By virtue of the flow-geomechanics coupling, our model captures the poroelastic stress changes that occur as a result of reservoir inflation. It is natural to expect that these poroelastic stresses will transfer to the splay faults on the hanging wall of the Amposta fault, and may result in de-stabilization of those faults.

In Figure 4.22, we show the stress changes in the Splay1AB fault. The key effect controlling changes in CFF is the updip component (Fig. 4.22b), which is de-stabilizing for portions of the fault above the reservoir, and stabilizing below the reservoir, with magnitudes up to several tens of kPa (Fig. 4.22d). This illustrates that, indeed, portions of the splay faults can be de-stabilized by stress transfer and poroelastic effects.

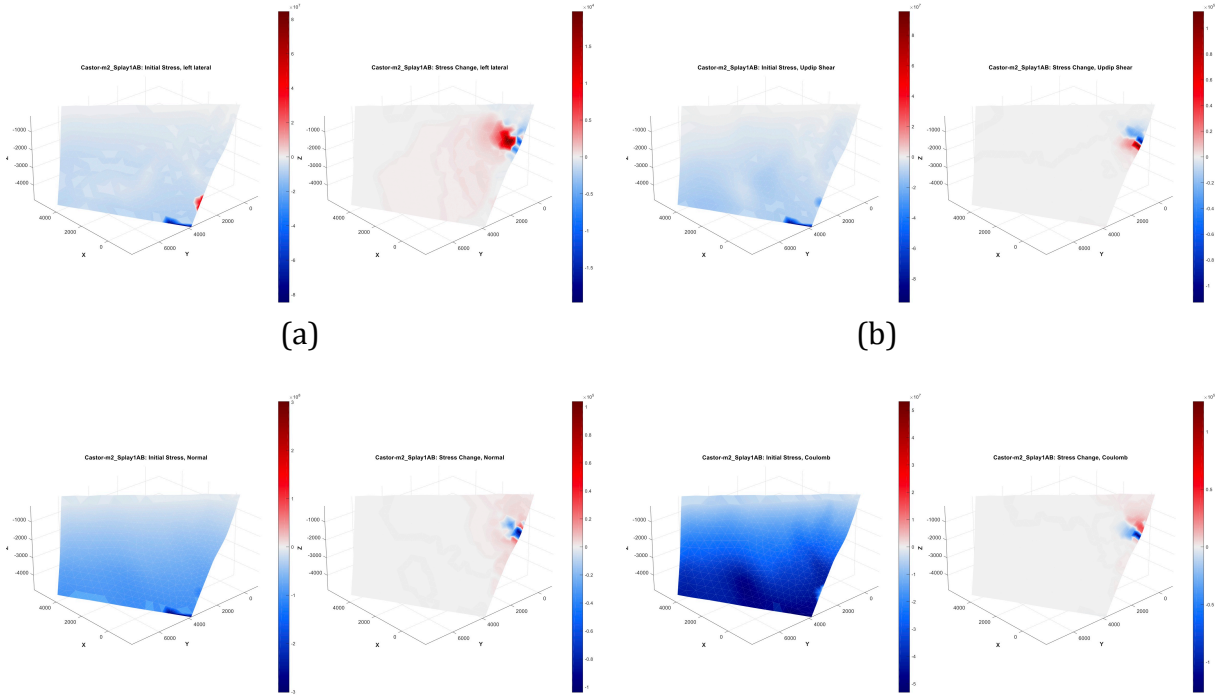

Figure 4.22: Illustration of initial stresses and stress changes on fault Splay1AB during the period September 1–September 16, 2013, as a result of gas injection. (a) Left-lateral stress; (b) Updip stress; (c) Effective normal stress; and (d) Coulomb stress.

The "Castor fault". It is interesting to analyze the stress changes in fault FEastBounding, which is an Southeast-dipping reservoir fault located farther away from the injection area. This fault has been termed the "Castor fault" in some previous reports (IGME, 2014). We show the stress changes for this fault in Figure 4.23. The left-lateral and updip components of stress change are both stabilizing (Fig. 4.23a and Fig. 4.23b, respectively), while the normal effective component is de-stabilizing as a result of pore-pressure increase (Fig. 4.23c). The key observation, however, is that stress changes on this fault, and in particular Coulomb stress changes (Fig. 4.23d) are in the order of 1 kPa, almost three order of magnitude smaller than for the Amposta fault and some of the reservoir faults in close proximity to injection. This is the result of both pressure changes and poroelastic stresses decaying strongly with distance.

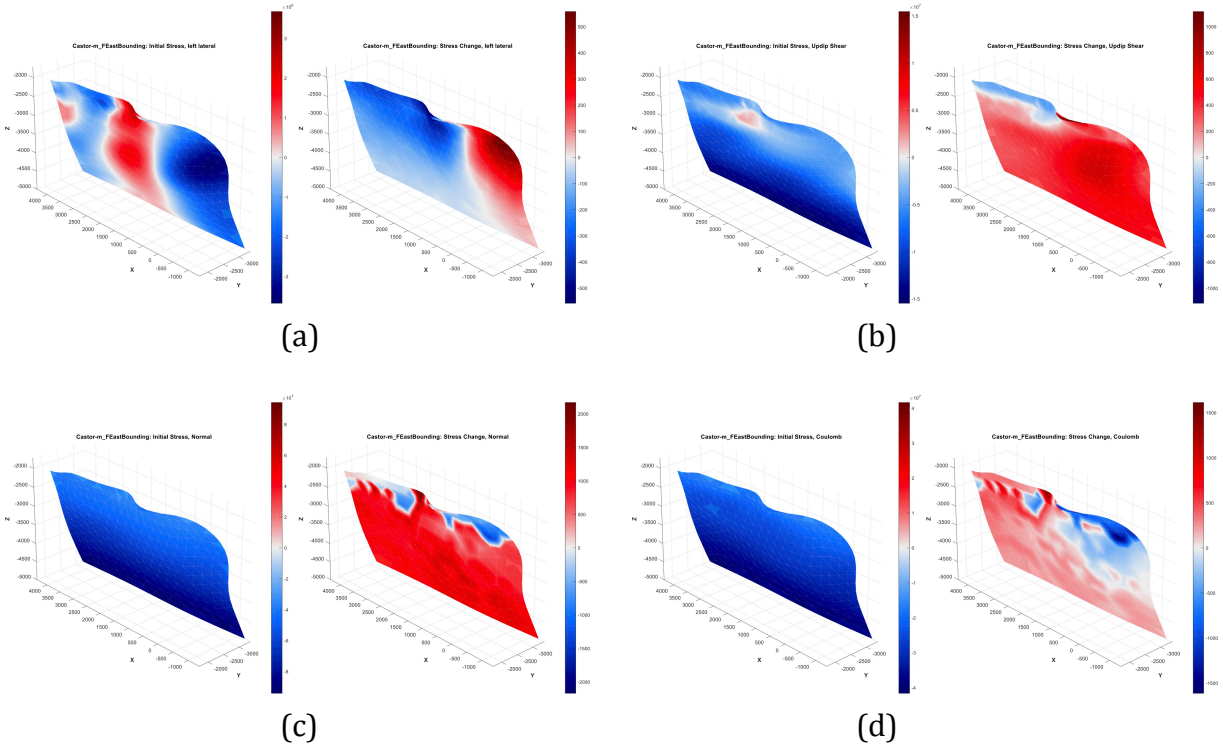

Figure 4.23: Illustration of initial stresses and stress changes on the FEastBounding fault ("Castor fault") during the period September 1–September 16, 2013, as a result of gas injection. (a) Left-lateral stress; (b) Updip stress; (c) Effective normal stress; and (d) Coulomb stress.

All faults in the model. These outputs exist for all faults in the model, and are evaluated dynamically over time. We summarize the results as a table that compiles the maximum stress changes on all faults (Table 4.2). While the pointwise maximum change in CFF is not, necessarily, a fundamental measure of destabilization of a portion of a fault, it is nevertheless indicative of the propensity of reservoir operations towards de-stabilization of individual faults. In Table 4.2, we complement that information with other percentiles of CFF change on each fault.

Table 4.2: Summary of Coulomb stress changes (in Pa) on all faults included in the model, during the period September 1–September 16, 2013.

Fault	min DCFF	P50 DCFF	P90 DCFF	P99 DCFF	max DCFF
Amposta_fault	-182838.4	724.3	1169.9	16329.6	560728.8
W_Main_fault	-314.5	-244.8	-217.7	-199.7	-196.7
F235	-10908.0	1112.9	2194.9	4338.6	5880.9
Splay1B_anti1	-1090.4	-708.2	1862.6	2068.0	2068.0
Splay1B_anti2	-313.6	-245.9	-178.3	-178.3	-178.3
Splay2B_anti1	-496.0	-351.7	-218.0	-162.4	-162.4
Splay3	-3567.4	-489.9	814.5	2134.5	2740.4
Splay1AB	-126233.6	-129.4	2231.5	28200.8	39733.8
Splay2AB_anti1	-14537.2	-438.1	1295.6	4175.0	6477.2
F10	-118972.4	5897.6	167913.8	315828.4	315828.4
F11	2056.2	6866.7	271291.9	416308.2	418104.7
F14	-579.7	403.4	572.7	1179.5	1179.5
FEastBounding	-1613.6	187.4	383.2	1185.8	1382.8
SouthFault	-129181.2	946.8	4734.5	87154.1	92023.3

4.6.2. Summary of the Analysis for Other Injection Scenarios

We have performed the coupled flow-geomechanics analysis for the other injection scenarios considered and described in Section 4.5. A summary of the results is given in Table 4.3, where we compile the maximum DCFF values predicted by the model on two representative faults: the Amposta fault, and the F10 reservoir fault. The reference case corresponds to the base-case model results described above. It is not surprising that the maximum DCFF values decrease for scenarios with reduced injection rate (and therefore, reduced injection volume). The more complex scenario that models more gas injection at a higher rate, followed by recovery of the injected gas and an additional injection cycle, results in larger de-stabilization (roughly, by a factor of two in terms of maximum DCFF) of the two faults.

Table 4.3: Summary of maximum DCFF values at two representative faults for different injection scenarios.

Fault	Reference	Rate 3 times smaller	Rate 5 times smaller	Rate 5 times smaller (longer inj.)	Recovery and additional injection cycle
Amposta_fault	5.6×10^5	1.6×10^5	4.2×10^4	4.3×10^4	9.8×10^5
F10	3.2×10^5	2.2×10^5	2.2×10^5	2.7×10^5	7.3×10^5

4.7. Synthesis of the Flow-Geomechanics Analysis

Based on the modeling results presented and discussed above, we make the following observations:

1. The Amposta fault is significantly de-stabilized by injection, with maximum DCFF of about 0.5 MPa.
2. Faults located on the hanging wall side of Amposta, such as the Splay1AB fault, are also de-stabilized (maximum DCFF of about 0.04 MPa), even though they are not subject to pressure variations directly – however, fault stresses are altered via poroelastic effects.
3. The most heavily de-stabilized faults, according to the model, are reservoir faults in close proximity to the Amposta fault (F11 with max DCFF ~ 0.4 MPa, F10 with max DCFF ~ 0.3 MPa, and SouthFault with max DCFF ~0.09 MPa). All of these faults are steeply dipping, in some cases to the Southeast (F10 and F11), in some cases to the Northwest (SouthFault).
4. Other reservoir faults farther away from the Castor platform are subject to minimal Coulomb stress changes. This is the case, for example, of the EastBounding fault (known in some previous reports as the "Castor fault"), subject according to our coupled flow-geomechanics model to a maximum DCFF of < 0.002 MPa.

Chapter 5. Integration of Results

Here we integrate the results of our geologic, seismologic, and reservoir flow-geomechanical analyses to assess the possible linkages between regional faults, the 2013 earthquake sequence, and Castor reservoir operations. Notably, the structural analysis and fault modeling were based on seismic reflection and well data, and did not use earthquake locations to constrain the faults. Similarly, the geomechanical analysis was based on the structural model and well production and injection schedules. Thus, a comparison of earthquake locations and focal mechanisms with the faults, as well as the production/injection induced pressure and stress changes, provides an objective way to evaluate the relationship between the seismicity and Castor field operations.

5.1. Identifying Faults that Sourced the Earthquakes

Earthquake locations for the 2013 sequence obtained prior to this study generally occur near the Castor platform. The Cesca et al. (2014) locations, which are provided for a subset of the events, lie north-northwest of platform (Figure 5.1A), whereas the IGN (2013) locations occur both to the north and south of the platform along a roughly northwest striking trend (Figure 5.1B). In contrast, the Gaite et al. (2016) locations occur north and east of the platform (Figure 5.1C). Our results, using two distinct velocity models, are more closely aligned with the IGN (2013) and Cesca et al. (2014) locations. Specifically, our locations define a roughly 15 by 15km area centered slightly west of the platform with a general north-northwest trend. Moreover, our preferred locations (Figure 5.1D) place the majority of the earthquakes in the area of Amposta fault, its hanging wall splays, and reservoir faults in the vicinity of the injection wells.

The Amposta fault system and its active splays trend northwest-southeast and exhibit oblique, right-lateral strike-slip and normal displacements. This is, in general, consistent with the earthquake focal mechanisms for the largest earthquake in the sequence determined by IGN (2014) and in this study. In contrast, the focal mechanisms of Cesca et al. (2014) include both steeply dipping, northwest striking and gently east dipping, northeast striking nodal planes. We find no faults, within the Amposta system or reservoir, that are compatible with these low-angle orientations. Thus, mindful of the uncertainties in the focal mechanism determinations outlined in Chapter 3, we suggest that the northwest striking nodal planes in the IGN (2014), Cesca et al., (2014), and our solutions are consistent with the seismic activity of the Amposta fault system that is implied by the earthquake locations.

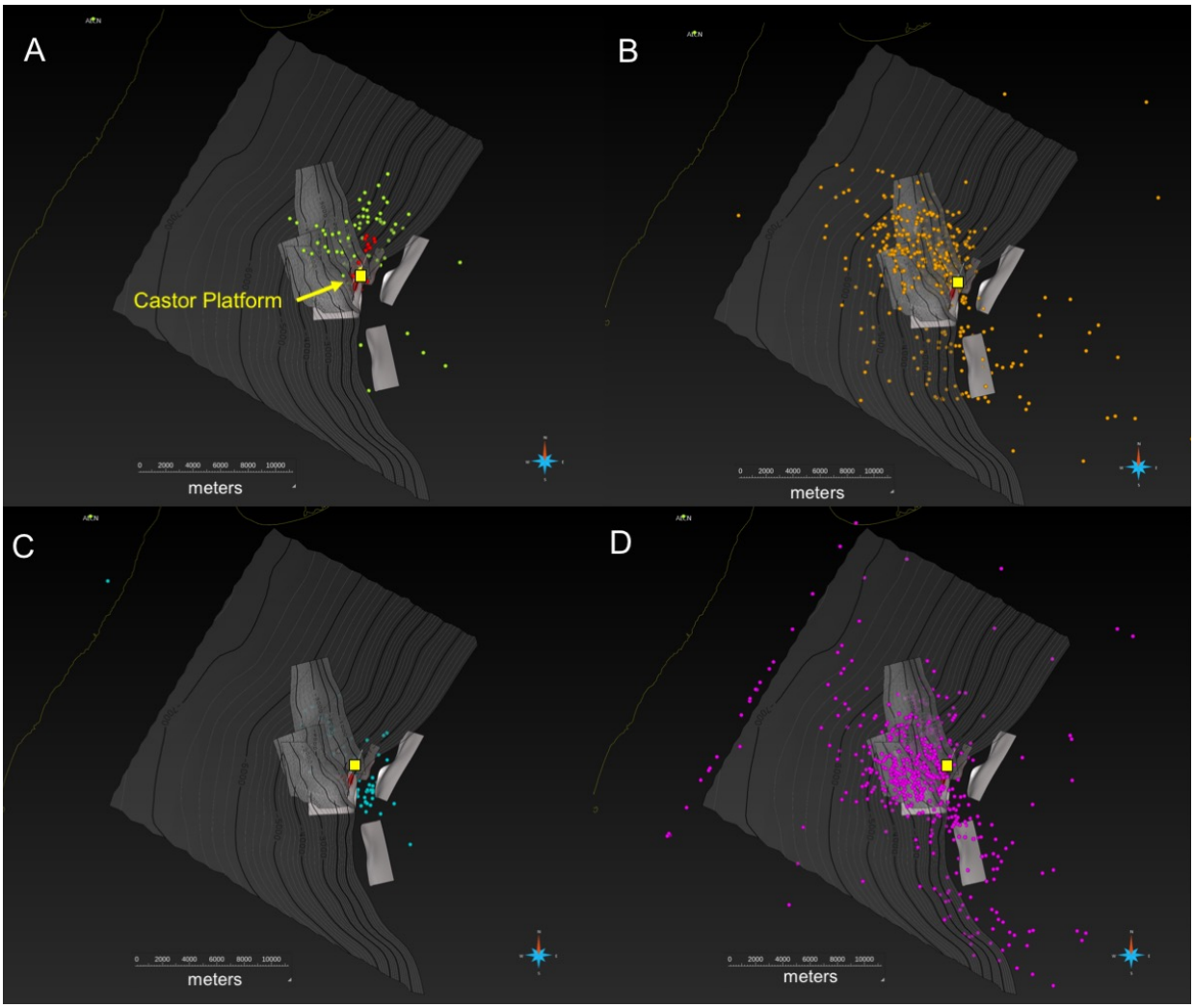

Figure 5.1: Map views of the 2013 earthquake sequence relative to the Castor Platform and faults represented in our structural model. A) Cesca et al. (2014) absolute locations (green) and relative locations (red) for select events; B) IGN (2013) locations; C) Gaite et al. (2016) locations for select events; D) locations obtained in this study using the layered velocity model.

Finally, we conclude from our analysis of the earthquake locations that many of the events occur at considerable (>10 km) distances from one another. This is driven by clear differences in the P and S wave arrival times at the stations. Unlike the uncertainties in absolute earthquake locations, we cannot reasonably ascribe these large differences in arrival times to uncertainties in the velocity field. Thus, while some earthquakes appear located on reservoir faults in the vicinity of the injection sites, no single reservoir fault is sufficient in size to explain all of the seismicity. This further supports our conclusion that the Amposta fault and its splays sourced some of the earthquakes.

5.2. Fault Stress Changes Compared with Earthquake Locations

The change in Coulomb Force Function (DCFF) values calculated from our couple flow and geomechanical analysis are resolved onto the faults represented in our structural model (Figure 5.2). Positive DCFF values, corresponding to changes that tend to destabilize the faults, occur during the injection period on a number of reservoir faults and portions of the Amposta fault system. As expected, these values are largest in the vicinity of injection wells and decrease as a function of distance away from them. Within the reservoir, the F10-11 faults exhibit the largest positive DCFF values (locally exceeding 1 MPa), with other faults (e.g, South Fault) showing smaller positive DCFF values. Notably, the EastBounding or Castor fault, which was suggested as a possible source of the seismicity (Cesca et al., 2014), shows only modestly positive DCFF values (< 0.0014 MPa). The section of the main Amposta fault lying immediately west of the injection wells also exhibits high positive DCFF values (locally exceeding 0.5 MPa), as do several of its hanging wall splays. These splays are not in the region of the model where fluid flow was simulated. Thus, their positive DCFF values are a result of reservoir expansion due to fluid injection.

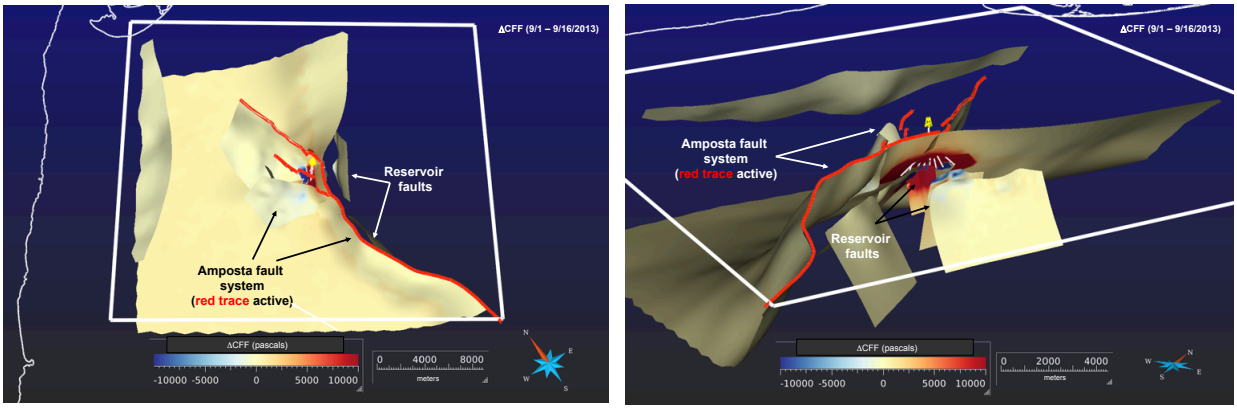

Figure 5.2: Two views of the Coulomb stress change (DCFF) on the model faults, between September 1 and September 16, 2013.

Comparison of the earthquake locations with the DCFF values shows that relocated hypocenters of the September-October 2013 earthquake sequence are concentrated in the region where the faults were significantly destabilized by reservoir operations (Figure 5.3). Specifically, the earthquakes are centered on the destabilized portions of the Amposta fault system as well as the F10-11 reservoir faults. This, combined with the temporal association of gas injection and the occurrence of the earthquakes, confirms that these events were triggered by field operations. Notably, not all of the earthquakes occur on portions of faults that were destabilized. Rather, many of these earthquakes are located up to 10 km away from the injector wells, near areas of faults with negligible DCFF values. This implies that some of these events were aftershocks of triggered earthquakes. This pattern also supports our interpretation that portions of the Amposta fault system were activated in this earthquake sequence, as no reservoir faults extend over this large area.

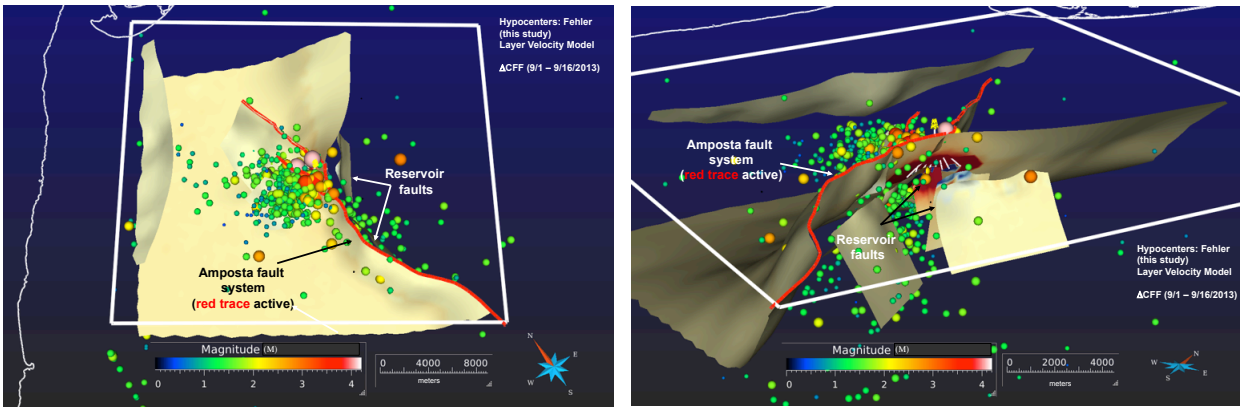

Figure 5.3: Two views of the earthquake locations relative to the Amposta fault system.

Notably, the portion of the Amposta fault system illuminated by the seismicity corresponds to its tectonically active segments. There are very few earthquakes that occur along the Amposta fault north of the field (Figure 5.3). This suggests that many of the events were triggered on critically stressed, geologically active faults, relieving a component of tectonic stress. Moreover, the six largest events in the sequence are clustered along the tectonically active juncture of the Amposta fault and its hanging wall splays (Figure 5.4). Presumably, the active portions of the faults were tectonically stressed near the point of failure, and thus CFF changes due to reservoir operations were sufficient to trigger slip.

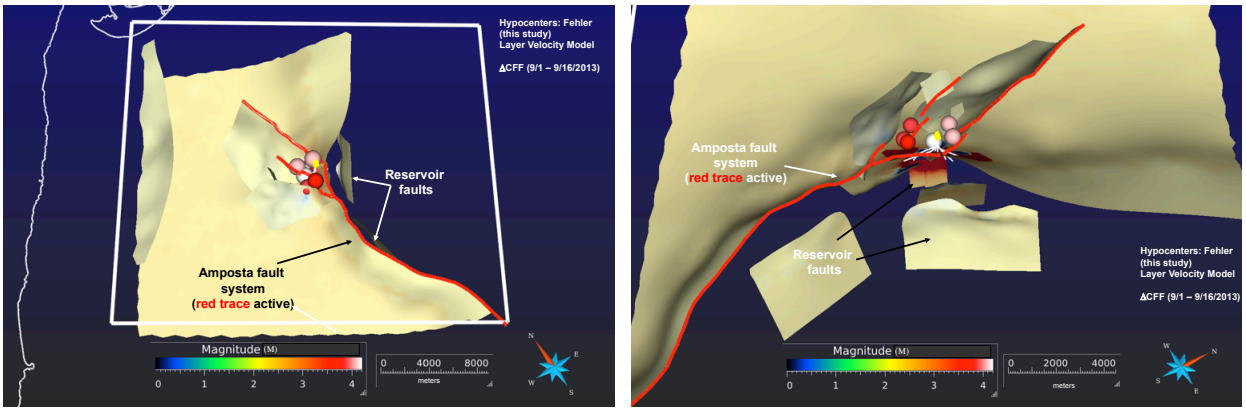

Figure 5.4: Two views of the earthquake locations of the 6 largest seismic events (of magnitudes 3.8 to 4.3).

Chapter 6. Conclusions

Taken together, the outcomes from our analysis point to the following assessment:

1. Earthquake hypocentral locations determined in this study are consistent with activity of the Amposta fault system, its splays, and faults within the reservoir in the vicinity of the injection sites.

2. The hypocenters of the first several events located near the reservoir, followed by a sequence of earthquakes clustered along and to the west of the tectonically active portions of the Amposta fault and its hanging wall splays.

3. The earthquake locations are clustered along and to the west of the tectonically active portions on the Amposta fault and its hanging wall splays.

4. Many relocated earthquakes map to regions of the faults that are destabilized due to injection operations. In particular, our coupled flow-geomechanics model suggests that Amposta, some of its splay faults and several of the reservoir faults in close proximity to Amposta, were significantly de-stabilized by gas injection, with induced Coulomb stress changes of up to 1 MPa. In contrast, the EastBounding fault (also known as the "Castor fault" in some reports) experienced changes in Coulomb stress < 0.002 MPa.

5. The six largest earthquakes (M 3.8 to 4.3) occurred late in the sequence, after injection ceased. These events are clustered in a region of the Amposta fault system that was significantly destabilized during gas injection.

6. Other earthquakes extend farther west and south along the Amposta fault system to areas that were not significantly affected by reservoir operations.

These observations suggest the following scenario for the event sequence:

1. Gas injection triggered seismicity on reservoir faults and nearby segments of the Amposta fault system.

2. These earthquakes, in turn, triggered seismicity on the Amposta fault system and possibly other reservoir faults through static or dynamic stress changes, well after injection stopped ("aftershock sequence"). This sequence included the largest earthquakes, which occurred on segments of the Amposta fault system destabilized by gas injection.

3. Earthquakes largely occurred on the tectonically active (southern) portion of the Amposta fault and its hanging wall fault splays.

Chapter 7. Recommendations

Coupled flow-geomechanics simulations of additional injection scenarios suggest the following:

1. While reduced injection rates generally reduce the maximum Coulomb stress change on Amposta and reservoir faults, values remain high and in risk of inducing seismic events. For reference, risk of de-stabilization of a fault is believed to occur for Coulomb stress changes in the order of 0.01 MPa – 0.1 MPa, and perhaps lower (this is in the range of typical stress drops during earthquakes).

2. The maximum Coulomb stress change is higher than that estimated for the post-mortem analysis in the case of full cycle of gas recovery and injection.

This points to an elevated risk of resuming operations in Castor:

1. Occurrence of M ~ 4 events likely have moved portions of the Amposta fault system closer to failure through static stress changes: these events might have increased Coulomb stress without relieving much moment.
2. Given the fault structures and history of de-stabilization, there is a possibility of earthquakes of significantly larger magnitude. It is worth noting that a complete rupture of the Amposta fault system in the study area could produce a M ≥ 6.8 earthquake, based on standard rupture-area-to-magnitude scaling relations.
3. Defining safe operating injection limits (maximum pressures, rates, volumes) is difficult.

In the case that a determination is made to resume operations, we recommend:

1. Deployment of a dedicated seismic network of ocean bottom seismic stations with good proximity and azimuthal coverage.
2. Slow ramp-up of injection in several phases, with dedicated analysis of seismicity, reservoir pressure, and updating of geomechanics model, after each phase.
3. Develop a protocol for actions to be taken if seismicity occurs or increases during injection (e.g., a traffic-light system).

Finally, it is important to point out that this is a *post-mortem* evaluation of the Castor project, which employs new paradigms for integrating geology, geophysics and reservoir geomechanics. As such, it is unreasonable to expect that a study with industry-standard methodologies would have reached these conclusions ahead of the injection. Our study, however, points to the need for *new standards* to quantify the seismicity risks associated to underground operations, especially in areas where active faults are present.

References

Aagaard, B., S. Kientz, M. Knepley, L. Strand, and C. Williams (2012), PyLith User Manual, Version 1.8.0, Comput. Infrastruct. for Geodyn., Univ. of Calif., Davis, Calif.

Aagaard, B. T., M. G. Knepley, and C. A. Williams (2013), A domain decomposition approach to implementing fault slip in finite-element models of quasi-static and dynamic crustal deformation, J. Geophys. Res. Solid Earth, 118, 3059–3079, doi:10.1002/jgrb.50217.

Amos, C. B. et al. (2014), Uplift and seismicity driven by groundwater depletion in central California. Nature 509, 483–486.

Anderson, E. M. (1951), The Dynamics of Faulting and Dyke Formation With Application to Britain, Oliver and Boyd, New York, N. Y.

Armero, F. (1999), Formulation and finite element implementation of a multiplicative model of coupled poro-plasticity at finite strains under fully saturated conditions, Comput. Methods Appl. Mech. Eng., 171, 205–241.

Armero, F., and J. C. Simo (1992), A new unconditionally stable fractional step method for non-linear coupled thermomechanical problems, Int. J. Numer. Methods Eng., 35, 737–766.

Armero, F., and J. C. Simo (1993), A priori stability estimates and unconditionally stable product formula algorithms for nonlinear coupled thermoplasticity, Int. J. Plasticity, 9, 749–782.

Ayala, C., Torne, M. and Roca, E. (2015), A review of the current knowledge of the crustal and lithospheric structure of the Valencia Trough Basin. Boletín Geológico y Minero, 126 (2-3): 533-552

Aziz, K., and A. Settari (1979), Petroleum Reservoir Simulation, Elsevier, London, U. K.

Bartrina, M.T., Cabrera, L., Jurado, M.J., Guimera, J. and Rota, E. (1992). Evolution of the central Catalan margin of the Valencia trough (western Mediterranean). In: E. Banda and P. Santanach (Editors), Geology and Geophysics of the Valencia Trough, western Mediterranean. Tectonophysics, 203: 219-247.

Bassin, C., Laske, G. & Masters, T.G. (2000). The current limits of resolution for surfacewave tomography in North America, EOS, Trans. Am. Geophys. Un., 81(48), Fall Meet. Suppl., Abstract S12A-03.

Bear, J. (1972), Dynamics of Fluids in Porous Media, John Wiley, New York, N. Y.

Beeler, N. M., R. W. Simpson, S. H. Hickman, and D. A. Lockner (2000), Pore fluid pressure,

apparent friction, and Coulomb failure, J. Geophys. Res., 105, 25,533–25,542.

Beer, G. (1985), An isoparametric joint/interface element for finite element analysis, Int. J. Numer. Methods Eng., 21, 585–600.

Biot, M. A. (1941), General theory of three-dimensional consolidation, J. Appl. Phys., 12, 155–164.

Bishop, A. W. (1959), The principle of effective stress, Tekniske Ukeblad, 39, 859–863.

Bishop, A. W., and G. E. Blight (1963), Some aspects of effective stress in saturated and partly saturated soils, Geotechnique, 13, 177–197.

Brodsky, E. E., and L. J. Lajoie (2013). Anthropogenic seismicity rates and operational parameters at the Salton Sea Geothermal Field. Science, 341, 543–546.

Buttinelli, M., L. Improta, S. Bagh, and C. Chiarabba (2016). Inversion of inherited thrusts by wastewater injection induced seismicity at the Val d'Agri oil eld (Italy). Scientific Reports, 6, 37165, doi:10.1038/srep37165.

Caine, J. S., and C. B. Forster (1999), Faults and Subsurface Fluid Flow in the Shallow Crust, Geophys. Monogr. Ser., vol. 113, edited by W. C. Haneberg et al., AGU, Washington, D. C.

Cao, H. (2002), Development of techniques for general purpose simulators, PhD thesis, Stanford Univ., Stanford, Calif.

Carol, I., A. Gens, and E. E. Alonso (1985), A three dimensional elastoplastic joint element, in Fundamentals of Rock Joints, pp. 441–451, Centek, Lulea, Sweden.

Cesca S., Grigoli, F. Heimann, S., Gonzalez, A., Buforn, E., Maghsoudi, S., Blanch E., and Dahm, T. (2014). The 2013 September–October seismic sequence offshore Spain: A case of seismicity triggered by gas injection? Geophys. J. Int., 198:941–953.

Chester, F. M., J. P. Evans, and R. Biegel (1993), Internal structure and weakening mechanisms of the San Andreas Fault, J. Geophys. Res., 98, 771–786.

Collier, J. S., Buhl, P., Torne, M., and Watts, A.B. (1994). Moho and lower crustal reflectivity beneath a young rift basin: results from a two-ship, wide-aperture seismic-reflection experiment in the Valencia Trough (western Mediterranean). *Geophys J Int.,* 118 (1): 159-180. doi: 10.1111/j.1365-246X.1994.tb04681.x

Coussy, O. (1995), Mechanics of Porous Continua, John Wiley, Chichester, U. K.

Coussy, O. (2004), Poromechanics, John Wiley, Chichester, U. K.

Coussy, O., R. Eymard, and T. Lassabatere (1998), Constitutive modeling of unsaturated drying deformable materials, J. Eng. Mech., 124(6), 658–557.

Coussy, O., P. Dangla, T. Lassabatere, and V. Baroghel-Bouny (2004), The equivalent pore pressure and the swelling and shrinkage of cement-based materials, Mater. Struct., 37, 15–20.

CUBIT (2013), CUBIT 13.2 User Documentation, Sandia Natl. Lab., Albuquerque, N. M.

Dean, R. H., X. Gai, C. M. Stone, and S. E. Minkoff (2006), A comparison of techniques for coupling porous flow and geomechanics, Soc. Pet. Eng. J., 11, 132–140.

Deichmann, N., and D. Giardini (2009), Earthquakes induced by the stimulation of an enhanced geothermal system below Basel (Switzerland), Seismol. Res. Lett. 80(5), 784-798.

Dost, B., and H. W. Haak (2007). Natural and induced seismicity. In Th. E. Wong, D. A. J. Batjes, and J. de Jager, editors, Geology of the Netherlands, pages 223–229. Royal Netherlands Academy of Arts and Sciences.

Ellsworth, W. L. (2013), Injection-induced earthquakes. Science 341, 1225942.

Felippa, C. A., and K. C. Park (1980), Staggered transient analysis procedures for coupled mechanical systems: Formulation, Comput. Methods Appl. Mech. Eng., 24, 61–111.

Ferronato, M., G. Gambolati, C. Janna, and P. Teatini (2008), Numerical modeling of regional faults in land subsidence prediction above gas/oil reservoirs, Int. J. Numer. Anal. Methods Geomech., 32, 633–657.

Ferronato, M., N. Castelletto, and G. Gambolati (2010), A fully coupled 3-D mixed finite element model of Biot consolidation, J. Comput. Phys., 229(12), 4813–4830.

Foulger, G. R., M. Wilson, J. Gluyas, B. R. Julian, and R. Davies (2017). A global review of human-induced earthquakes. Earth Science Reviews, in press.

Frohlich, C. (2012), Two-year survey comparing earthquake activity and injection-well locations in the Barnett Shale, Texas. Proc. Natl Acad. Sci. USA 109, 13934–13938.

Freed, A. (2005). Earthquake triggering by static, dynamic, and postseismic stress transfer: Ann. Rev. Earth Planet. Sci., 33, 335–67.

Gaite, B., Ugalde, A., Villaseñor, A., and Blanch, E. (2016). Improving the location of induced earthquakes associated with an underground gas storage in the Gulf of Valencia (Spain). Phys. Earth Planet. Inter., 254, 46-59.

Galchen, R. (2015), Weather underground – the arrival of man-made earthquakes. The New Yorker, April 13, 2015.

Gan, W. and C. Frohlich (2013), Gas injection may have triggered earthquakes in the Cogdell oil field, Texas. Proc. Natl Acad. Sci. USA 110, doi:10.1073/pnas.1311316110.

García-Mayordomo, J. et al. (2012). The quaternary active faults Database of Iberia (QAFI v.2.0), J. Iber. Geol., 38:285–302.

Geertsma, J. (1957), The effect of fluid pressure decline on volumetric change of porous rocks, Trans. AIME, 210, 331–340.

Gens, A., I. Carol, and E. E. Alonso (1988), An interface element formulation for the analysis of soil-reinforcement interaction, Comput. Geotech., 7, 133–151.

Geostock Iberia (2011). Castor Underground Gas Storage Project, Dynamic Modeling Report.

Gibbs, A. D. (1983), Balanced cross-section construction from seismic sections in areas of extensional tectonics: Journal of Structural Geology, 5, 153–160.

Gonzalez, P. J., K. F. Tiampo, M. Palano, F. Cannavo, J. Fernandez (2012), The 2011 Lorca earthquake slip distribution controlled by groundwater crustal unloading. Nature Geosci. 5, 821-825.

Goodman, R. E., R. L. Taylor, and T. L. Brekke (1968), A model for the mechanics of jointed rock, J. Soil Mech., 94, 637–659.

Gray, W. G., and B. A. Schrefler (2001), Thermodynamic approach to effective stress in partially saturated porous media, Eur. J. Mech.-A/Solids, 20, 521–538.

Groshong, R. (1990), Unique determination of normal fault shape from hanging-wall bed geometry in detached half grabens: Eclogae Geologicae Helvetiae, 83:455–471.

Guglielmi, Y., F. Cappa, J.-P. Avouac, P. Henry, and D. Elsworth (2015), Seismicity triggered by fluid injection–induced aseismic slip. Science 348 1224-1226.

Hamblin, W. K. (1965). Origin of “reverse drag” on the downthrown side of normal faults: Geological Society of America Bulletin, 76:1145–1164.

Hardebeck, J. L., Nazareth, J. J., and Hauksson, E. (1998). The static stress change triggering model: Constraints from two Southern California aftershock sequences. J. Geophys. Res., 103(24), 427-37.

Harris, R. A., and R. W. Simpson (1992), Changes in static stress on southern California faults after the 1992 Landers earthquake, Nature, 360, 251–254.

Harris, R. A., R. W. Simpson, and P. A. Reasenberg (1995), Influence of static stress changes on earthquake locations in southern California, Nature, 375, 221–224.

Hornbach, M. J., H. R. DeShon, W. L. Ellsworth, B. W. Stump, C. Hayward, C. Frohlich, H. R. Oldham, J. E. Olson, M. B. Magnani, C. Brokaw, and J. H. Luetgert (2015). Causal factors for seismicity near Azle, Texas. Nature Comm., doi:10.1038/ncomms7728.

Hubbert, M. K., and W. W. Rubey (1959), Role of fluid pressure in mechanics of overthrust faulting. I. Mechanics of fluid-filled porous solids and its application to overthrust faulting, Geol. Soc. Am., 70, 115–166.

IGME – Instituto Geológico y Minero de España (2013). Informe Geológico sobre la Crisis Sísmica Relacionada con el Almacén Subterráneo de Gas Denominado Castor (Castellón, Noroeste de España).

IGME – Instituto Geológico y Minero de España (2014). Informe Geológico sobre la Crisis Sísmica Relacionada con el Almacén Subterráneo de Gas denominado Castor (Castellón, Noroeste de España) – Revisión.

IGN – Instituto Geográfico Nacional (2013). Informe sobre la actividad sísmica en el Golfo de Valencia, 38pp.

Improta, L., L. Valoroso, D. Piccinini, and C. Chiarabba (2015). A detailed analysis of wastewater-induced seismicity in the Val d'Agri oil field (Italy). Geophys. Res. Lett., 42, doi:10.1002/2015GL063369.

Jeannin, L., M. Mainguy, R. Masson, and S. Vidal-Gilbert (2007), Accelerating the convergence of coupled geomechanical–reservoir simulations, Int. J. Numer. Anal. Methods Geomech., 31, 1163–1181.

Jha, B., and R. Juanes (2007). A locally conservative finite element framework for modeling coupled fluid flow and reservoir geomechanics. Acta Geotechnica, 2(3):139–153.

Jha, B., and R. Juanes (2014). Coupled multiphase flow and poromechanics: A computational model of pore pressure effects on fault slip and earthquake triggering. Water Resour. Res., 50(5), 3776-3808.

Jha, B., F. Bottazzi, R. Wojcik, M. Coccia, N. Bechor, D. McLaughlin, T. A. Herring, B. H. Hager, S. Mantica, and R. Juanes (2015). Reservoir characterization in an underground gas storage field using joint inversion of flow and geodetic data. Int. J. Numer. Anal. Meth. Geomech., 39(4), 1619-1638.

Juanes, R., J. Samper, and J. Molinero (2002), A general and efficient formulation of fractures and boundary conditions in the finite element method, Int. J. Numer. Methods Eng., 54(12), 1751–1774.

Juanes, R., B. H. Hager, B. Jha, J. H. Shaw , A. Plesch, L. Astiz, J. H. Dieterich, C. Frohlich (2016). Were the May 2012 Emilia-Romagna earthquakes induced? A coupled flow-geomechanics modeling assessment. Geophysical Research Letters, 43(13), 6891-6897.

Keranen, K. M., H. M. Savage, G. A. Abers, and E. S. Cochran (2013). Potentially induced earthquakes in Oklahoma, USA: Links between wastewater injection and the 2011 Mw 5.7 earthquake sequence. Geology, doi:10.1130/G34045.1.

Keranen, K., Weingarten, M., Abers, G. A., Bekins, B. A. and Ge, S. (2014), Sharp increase in central Oklahoma seismicity since 2008 induced by massive wastewater injection. Science 345, 448–451.

Khalili, N., F. Geiser, and G. E. Blight (2004), Effective stress in unsaturated soils: A review with new evidence, Int. J. Geomech., 4, 115–126.

Kim, J., H. A. Tchelepi, and R. Juanes (2011a). Stability and convergence of sequential methods for coupled flow and geomechanics: Drained and undrained splits. Comput. Methods Appl. Mech. Engrg., 200:2094–2116.

Kim, J., H. A. Tchelepi, and R. Juanes (2011b). Stability and convergence of sequential methods for coupled flow and geomechanics: Fixed-stress and fixed-strain splits. Comput. Methods Appl. Mech. Engrg., 200(13–16):1591–1606.

Kim J., H. A. Tchelepi, and R. Juanes (2011c). Stability, accuracy and efficiency of sequential methods for coupled flow and geomechanics. Soc. Pet. Eng. J., 16:249–262.

Kim, J., H. A. Tchelepi, and R. Juanes (2013). Rigorous coupling of geomechanics and multiphase flow with strong capillarity, Soc. Pet. Eng. J., 18(6), 1123–1139.

LaGriT (2013), LaGriT Manual, Los Alamos Natl. Lab., Los Alamos, N. M.

Laske, G., G. Masters, and C. Reif (2000), CRUST 2.0: A New Global Crustal Model at 22 Degrees. Institute of Geophysics and Planetary Physics, The University of California, San Diego.

Lei, X. Y., G. Swoboda, and G. Zenz (1995), Application of contact-friction interface element to tunnel excavation in faulted rock, Comput. Geotech., 17, 349–370.

Lewis, R. W., and B. A. Schrefler (1998), The Finite Element Method in the Static and Dynamic Deformation and Consolidation of Porous Media, 2nd ed., John Wiley, Chichester, U. K.

Lewis, R. W., and Y. Sukirman (1993), Finite element modelling of three-phase flow in deforming saturated oil reservoirs, Int. J. Numer. Anal. Methods Geomech., 17, 577–598.

Lewis, R. W., A. Makurat, and W. K. S. Pao (2003), Fully coupled modeling of seabed subsidence and reservoir compaction of North Sea oil fields, Hydrogeol. J., 11(1), 142–161.

Li, J., Kuleli, H. S., Zhang, H., and Toksöz, M. N. (2011). Focal mechanism determination of induced microearthquakes in an oil field using full waveforms from shallow and deep seismic networks, *Geophysics*, 76(6), WC87-WC101.

Li, X., Z. Liu, and R. W. Lewis (2005), Mixed finite element method for coupled thermo-hydro-mechanical process in poro-elastic-plastic media at large strains, Int. J. Numer. Methods Eng., 64(5), 667–708.

Majer E. L, et al. (2007), Induced seismicity associated with enhanced geothermal systems. Geothermics 36(3):185–222.

Mainguy, M., and P. Longuemare (2002), Coupling fluid flow and rock mechanics: Formulations of the partial coupling between reservoir and geomechanics simulators, Oil Gas Sci. Technol., 57, 355–367.

Mallet, J. L. (1992), GOCAD: a computer aided design program for geological applications. In K. Turner (Ed.), Three-dimensional modeling with geoscientific information systems (pp. 123-141). Springer Netherlands.

Minkoff, S. E., C. M. Stone, S. Bryant, M. Peszynska, and M. F. Wheeler (2003), Coupled fluid flow and geomechanical deformation modeling, J. Pet. Sci. Eng., 38, 37–56.

Molinero, J., J. Samper, and R. Juanes (2002), Numerical modeling of the transient hydrogeological response produced by tunnel construction in fractured bedrocks, Eng. Geol., 64(4), 369–386.

Muskat, M. (1949), Physical Principles of Oil Production, McGraw-Hill, New York, N. Y.

National Research Council (2013), Induced Seismicity Potential in Energy Technologies. National Academies Press, Washington DC.

Nauroy, J.-F., A. Baroni, and N. Guy (2011), Geomechanical Study for Castor Gas Storage, IFP –Energies nouvelles, Report # 62034.

Nikooee, E., G. Habibagahi, S. M. Hassanizadeh, and A. Ghahramani (2013), Effective stress in unsaturated soils: A thermodynamic approach based on the interfacial energy and hydromechanical coupling, Transp. Porous Media, 96, 369–396.

Nuth, M., and L. Laloui (2008), Effective stress concept in unsaturated soils: Clarification and validation of a unified framework, Int. J. Numer. Anal. Methods Geomech., 32, 771–801.

Pan, H., and H. Cao (2010), User Manual for General Purpose Research Simulator, Stanford Univ. Pet. Eng. Inst., Stanford, Calif.

Pao, W. K. S., and R. W. Lewis (2002), Three dimensional finite element simulation of three-phase flow in a deforming fissured reservoir, Comput. Methods Appl. Mech. Eng., 191, 2631–2659.

Perea, H., Masana, E., and Santanach, P. (2012). An active zone characterized by slow normal faults, the northwestern margin of the Valencia trough (NE Iberia): a review, *J. Iber. Geol.,* 38:31–52.

Raleigh, C. B., J. H. Healy, and J. D. Bredehoeft (1976), An experiment in earthquake control at Rangely, Colorado. Science 191, 1230–1237.

Reasenberg, P. A., and R. W. Simpson (1992), Response of regional seismicity to the static stress change produced by the Loma Prieta earthquake, Science, 255, 1687–1690.

Rice, J. (1992), Fault Stress States, Pore Pressure Distributions, and the Weakness of the San Andreas Fault, pp. 475–503, Academic Press, London, U. K.

Roca, E., and J. Guimerà (1992). The Neogene structure of the eastern Iberian margin: structural constrains on the crustal evolution of the Valencia trough (western Mediterranean), *Tectonophysics,* 203:203–218.

Rutqvist, J., Y. S. Wu, C. F. Tsang, and G. Bodvarsson (2002), A modeling approach for analysis of coupled multiphase fluid flow, heat transfer, and deformation in fractured porous rock, Int. J. Rock Mech. Min. Sci., 39, 429–442.

Rutqvist, J., J. T. Birkholzer, and C. F. Tsang (2008), Coupled reservoir–geomechanical analysis of the potential for tensile and shear failure associated with CO2 injection in multilayered reservoir–caprock systems, Int. J. Rock Mech. Min. Sci., 45, 132–143.

Ryan, W.B.F., Carbotte, S.M., Coplan, J.O., O'Hara, S., Melkonian, A., Arko, R., Weissel, R.A., Ferrini, V., Goodwillie, A., Nitsche, F., Bonczkowski, J., and Zemsky, R. (2009). Global Multi-Resolution Topography synthesis, Geochem. Geophys. Geosyst., 10, Q03014, doi:10.1029/2008GC002332.

Saló, L., T. Frontera, X Goula, L Pujades, and A. Ledesma (2017). Earthquake static stress transfer in the 2013 Valencia Gulf (Spain) seismic sequence, Solid Earth Diss., in review.

Samier, P., and S. Gennaro (2007), A practical iterative scheme for coupling geomechanics with reservoir simulation, paper SPE 107077 presented at SPE Europec/EAGE, Society of Petroleum Engineers, London, U. K.

Schlumberger (2016), Eclipse 100 Reference Manual 2016.1, Schlumberger Inf. Solutions, Houston, Tex.

Segall, P. (1989), Earthquake triggered by fluid extraction. Geology 17, 942–946.

Seemann, U., Pumpin, V.F., and Casson, N. (1990). Amposta oil field, in *Proceedings of the AAPG Treatise of Petroleum Geology: Atlas of Oil and Gas Fields, Structural Traps II: Traps Associated with Tectonic Faulting,* American Association of Petroleum Geologists, Tulsa, Oklahoma, USA, A-016, 20 pp.

Segura, J. M., and I. Carol (2004), On zero-thickness interface elements for diffusion problems, Int. J. Numer. Anal. Methods Geomech., 28, 947–962.

Segura, J. M., and I. Carol (2008a), Coupled HM analysis using zero-thickness interface elements with double nodes. Part I: Theoretical model, Int. J. Numer. Anal. Methods Geomech., 32, 2083–2101.

Segura, J. M., and I. Carol (2008b), Coupled HM analysis using zero-thickness interface elements with double nodes. Part II: Verification and application, Int. J. Numer. Anal. Methods Geomech., 32, 2103–2123.

Settari, A., and F. Mourits (1998), A coupled reservoir and geomechanical simulation system, Soc. Pet. Eng. J., 3, 219–226.

Settari, A., and D. A. Walters (2001), Advances in coupled geomechanical and reservoir modeling with applications to reservoir compaction, Soc. Pet. Eng. J., 6, 334–342.

Shaw, J.H., S.C. Hook, and E. Sitohang (1997). Extensional fault-bend folding and synrift deposition: An example from the Central Sumatra Basin, Indonesia, American Association of Petroleum Geologists Bulletin, 81(3):367-379.

Sibson, R. H. (1977), Fault rocks and fault mechanisms, J. Geol. Soc. London, 133, 191–213.

Sibson, R. H. (1981), Fluid flow accompanying faulting: Field evidence and models, in Earthquake Prediction: An International Review, Maurice Ewing Ser., vol. 4, pp. 593–603, AGU, Washington, D. C.

Sibson, R. H. (1986), Brecciation processes in fault zone: Inferences from earthquake rupturing, Pure Appl. Geophys., 124, 159–175.

Sibson, R. H. (1990), Rupture nucleation on unfavorably oriented faults, Bull. Seismol. Soc. Am., 80, 1580–1604.

Sibson, R. H. (1994), Crustal stress, faulting and fluid flow, Geol. Soc. Spec. Publ., 78, 69–84.

Suckale, J. (2009), Induced seismicity in hydrocarbon fields. In R. Dmowska, editor, Adv. Geophys., volume 51, pages 55–106. Academic Press, USA.

Sukirman, Y., and R. W. Lewis (1993), A finite element solution of a fully coupled implicit formulation for reservoir simulation, Int. J. Numer. Anal. Methods Geomech., 17(10), 677–698.

Thomas, L. K., L. Y. Chin, R. G. Pierson, and J. E. Sylte (2003), Coupled geomechanics and reservoir simulation, Soc. Pet. Eng. J., 8(4), 350–358.

Torne, M., Pascal, G. , Buhl, P. , Watts, A.B., and Mauffret, A. (1992). Crustal and velocity structure of the Valencia trough (western Mediterranean), Part I. A combined refraction/wide angle reflection and near-vertical reflection study, *Tectonophysics*, 203, 1-20.

Tran, D., A. Settari, and L. Nghiem (2004), New iterative coupling between a reservoir simulator and a geomechanics module, Soc. Pet. Eng. J., 9(3), 362–369.

Tran, D., L. Nghiem, and L. Buchanan (2005), Improved iterative coupling of geomechanics with reservoir simulation, paper SPE 93244 presented at SPE Reservoir Simulation Symposium, Society of Petroleum Engineers, Houston, Tex.

Valoroso, L., L. Improta, L. Chiaraluce, R. Di Stefano, L. Ferranti, A. Govoni, and C. Chiarabba (2009). Active faults and induced seismicity in the Val d'Agri area (Southern Apennines, Italy). Geophys. J. Int., 178, 488–502.

van der Elst, N. J., H. M. Savage, K. M. Keranen, and G. A. Abers (2013), Enhanced remote earthquake triggering at fluid-injection sites in the midwestern United States, Science, 341, 164–167.

Vidal, N., Gallart, J. and Dañobeitia, J.J. (1998). A deep seismic crustal transect from the NE Iberian Peninsula to the western Mediterranean, Journal of Geophysical Research, 103, 12381-12396.

Vlahinic, I., H. M. Jennings, J. E. Andrade, and J. J. Thomas (2011), A novel and general form of effective stress in a partially saturated porous material: The influence of microstructure, Mech. Mater., 43, 25–35.

Villaseñor, A., Herrmann, R. B., Gaite, B., and Ugalde, A. (2016). Source parameters of induced earthquakes using regional earth models: Application to the 2013 sequence off the northeast coast of Spain. Personal communication.

Weingarten, M., S. Ge, J. W. Godt, B. A. Bekins, and J. L. Rubinstein (2015). High-rate injection is associated with the increase in U.S. mid-continent seismicity. Science 348:1336-1340.

Xiao, H., and J. Suppe (1992), Origin of rollover. AAPG Bulletin, v. 76, p. 509-525.

Zhang, H., S. Sarkar, M. Toksoz, S. Kuleli, and F. Al-Kindy (2009). Passive seismic tomography using induced seismicity at a petroleum field in Oman. Geophysics, 74:WCB57–WCB69.

Zienkiewicz, O. C., D. K. Paul, and A. H. C. Chan (1988), Unconditionally stable staggered solution procedure for soil–pore fluid interaction problems, Int. J. Numer. Methods Eng., 26(5), 1039–1055.

Acknowledgments

We thank Enagas for providing all the data that made this study possible. In particular, we thank Ana María García Domínguez and Borja González Cansado for their exceptional help in all matters related to data availability for the project and for following the technical work with interest, and Rosa María Nieto Prieto for her persistence (and patience) to see this study to completion.